10-23-2018

First-Principles Study on the Catalytic Role of Cerium Dioxide in the Conversion of Organic Compounds

Chuanlin Zhao
Louisiana State University and Agricultural and Mechanical College

Recommended Citation

Zhao, Chuanlin, "First-Principles Study on the Catalytic Role of Cerium Dioxide in the Conversion of Organic Compounds" (2018). *LSU Doctoral Dissertations*. 4753.
https://repository.lsu.edu/gradschool_dissertations/4753

FIRST-PRINCIPLES STUDY ON THE CATALYTIC ROLE OF CERIUM DIOXIDE IN THE CONVERSION OF ORGANIC COMPOUNDS

A Dissertation

Submitted to the Graduate Faculty of the
Louisiana State University and
Agricultural and Mechanical College
in partial fulfillment of the
requirements for the degree of
Doctor of Philosophy

in

Cain Department of Chemical Engineering

by
Chuanlin Zhao
B.E., Tianjin University, 2012
M.S., Louisiana State University, 2013
December 2018

To *Yuhuan* & *Min*
Lijun & *Huidou*
Zhuojun & *Xiyuan*

Where is everybody?

--Enrico Fermi

ACKNOWLEDGEMENTS

This dissertation could not be accomplished without the generous sponsorship from National Science Foundation and Louisiana Board of Regents. From the scientific perspective, I would like to thank the following dedicated experimental collaborators involved in the research project: Dr. Steven Overbury, Dr. David Mullins, Dr. Florencia Calaza, and Dr. Aditya Savara from Oak Ridge National Lab, Dr. Vladimír Matolín from Charles University, Czech Republic, Dr. Kenya Shimada from Hiroshima University, Japan, Dr. Chao Wang from John Hopkins University. Most importantly, it is my dear professor, Dr. Ye Xu, who provides me with the cheerful opportunity to work with the above mentioned world-class scientists and engineers. Without his tireless guidance and stringent scientific requirements, such fruitful research achievements throughout my Ph.D. years would never become a reality. I would also like to thank my Ph.D. committee members for small but meaningful discussions: Drs. William Shelton, Kerry Dooley, Kenneth Lopata, and Patrick DiMario. Computation hardware are provided by Louisiana State University High Performance Computing, Louisiana Optical Network Infrastructure, and National Energy Research Scientific Computing Center. From the humanistic perspective, I was, am, and will always be grateful about the love and support from my parents and grandparents. At last, I will always remember and appreciate the hospitality of the people I met in the United States.

TABLE OF CONTENTS

ACKNOWLEDGEMENTS ……………………………………....................................v

NOMENCLATURE, SYMBOLS, ACRONYMS ……………………………………..vii

ABSTRACT …………………………………………………………………...viii

INTRODUCTION ………………………………………………………….........1

TECHNICAL APPROACH …………………………………………………........20

RESULTS AND DISCUSSION …….………………………….....................................27

SUMMARY ……………………………………...…………………………......81

REFERENCES …………………………………………………………………......84

APPENDIX. COPYRIGHT INFORMATION…...…...…………………………………..101

VITA …………………………………………………………………………........107

NOMENCLATURE, SYMBOLS, ACRONYMS

AA: acetic acid, CH_3COOH
AcH: acetaldehyde, CH_3CHO
Ace: acetone, CH_3COCH_3
Actl: acetonyl, CH_2COCH_3
Ata: acetate, CH_3COO
CrA: crotonaldehyde, $CH_3CHCHCHO$
DFT: density functional theory
DOS: density of states
D: C-O dimer from two acetaldehyde
E_a: activation energy barrier
E_{gas}: DFT total energy of the atom or molecule in the gas phase in a neutral state
E_{slab}: DFT total energy of the clean surface
E_{total}: DFT total energy of the slab with the adsorbed atom or molecule
Enl: enolate of acetaldehyde, CH_2CHO
FS: final state of the minimum energy path
IS: initial state of the minimum energy path
hTST: harmonic transition state theory approximation
Ket: ketene of acetic acid, $CH_2CO\text{-}O$
MkM: microkinetic modeling
MP: methyl phosphate monoester
*p*DOS: projected density of states
p-NPP: *para*-nitrophenyl phosphate monoester
RPES: resonant photoelectron spectroscopy
T_B: breaking temperature set in 1st temperature ramping
T_p: peak temperature of desorption
TPD: temperature programmed desorption
TS: transition state of the minimum energy path
V_o: single oxygen vacancy
VV_o: oxygen vacancy dimer
XPS: X-ray photo-emission spectroscopy
ZPE: zero-point energy
ΔE_{ads}: adsorption energy
ΔE_{rxn}: reaction energy
β-KA: β-keto acid, CH_3COCH_2COOH
θ: surface coverage
*: surface free adsorption site

ABSTRACT

Ceria is an earth-abundant material that has been widely used in heterogeneous catalysis, environmental catalysis, and energy applications thanks for its ability to readily convert between different oxidation states. The objective of this study is to theoretically elucidate the reaction mechanisms for the conversion of model organic compounds on ceria, in order to gain insights for the design of cost-effective and selective ceria-based catalysts. Acetaldehyde, acetic acid, and *para*-nitrophenyl phosphate monoester were selected as the model compounds to probe ceria surfaces. Density functional theory calculations can provide accurate predictions of adsorption and reaction energetics, which can be used to calculate the necessary kinetic parameters in the microkinetic model that can validate hypothesized reaction mechanisms. This methodology is also able to generate additional insights regarding the dominant surface species, the existence of transient surface species, and the role of active sites such as defects. Based on the spectroscopic evidence from surface science experiments, we were able to validate the proposed reaction mechanism for temperature programmed desorption of acetaldehyde and acetic acid on ceria surfaces. Particularly, the catalytic role of surface oxygen vacancy during the formation of ethylene, acetylene and crotonaldehyde in the AcH-TPD was examined. The desorption of crotonaldehyde is found to be the rate-limiting step. However, pre-existing oxygen vacancy is not required in the AA-TPD due to facile surface reduction induced by deprotonation of acetic acid. We found the ketene pathway was energetically more favorable than the acetone pathway under UHV condition. Our results showed that ceria can be effective in the dephosphorylation of selected monoesters including *p*-NPP, due to facile P-O ester bond scission. However, the subsequent step-wise hydration is found to be rate-limiting.

INTRODUCTION

1.1 Catalysis Related Properties of Ceria

Ceria is a well-known material in heterogeneous catalysis, environmental catalysis, and energy applications [1, 2]. Ceria is shown to enhance the redox activity of metal catalysts in a number of technological reactions, including the automotive three-way catalysis [3, 4], water-gas shift (WGS) [5], hydrocarbon reforming [6], CO_2 reduction [7], and combustion of soot and volatile organic compounds [8]. Ceria has also been used as key components of solid electrolytes and even electrodes in solid oxide fuel cells [9], and energy carriers in solar thermochemical reactors [10]. Many of its useful properties can be traced to the ability of the Ce cation to readily convert between the +3 and +4 oxidation states chemically and structurally. Meanwhile, cerium is the most abundant of the lanthanides in Earth's crust, with its abundance being comparable to common metals such as chromium, nickel, and copper, and higher than tin and lead. The unique chemical properties of ceria coupled with availability makes it a highly attractive material for current and future catalytic and energy applications.

Different from other rare-earth elements, cerium dioxide (CeO_2) is a more stable phase than the sesquioxide phase (Ce_2O_3) under ambient conditions. Identified as the fluorite structure (space group Fm3m), CeO_2 has its 4 Ce atoms locate in the face-center and corner sites of the unit cell, while 8 O atoms locate inside the unit cell with each O atom adopting a tetrahedron coordination configuration, as shown in **Figure 1.1a**. Among the low-index facets of CeO_2, CeO_2(111) turns out to be thermodynamically the most stable one, followed by (110) and (100) surfaces [11]. CeO_2(111) thin film can be grown on several metal substrates, such as Ru(0001) [12], Cu(111) [13], Pt(111) [14], Rh(111) [15] and other fcc single crystal metal surfaces [12, 16, 17], via depositing Ce metal onto the metal substrates under a background O_2 partial pressure; due to the more reactive nature, $CeO_2(100)$ thin film turns out to be more difficult to grow but has been managed on substrates such as $SrTiO_3(100)$, α-Al_2O_3, Pd(100), Pt(100), biaxially textured Ni(100) and yttria-stabilized $ZrO_2(100)$ [18]. An advantage of the thin film format as

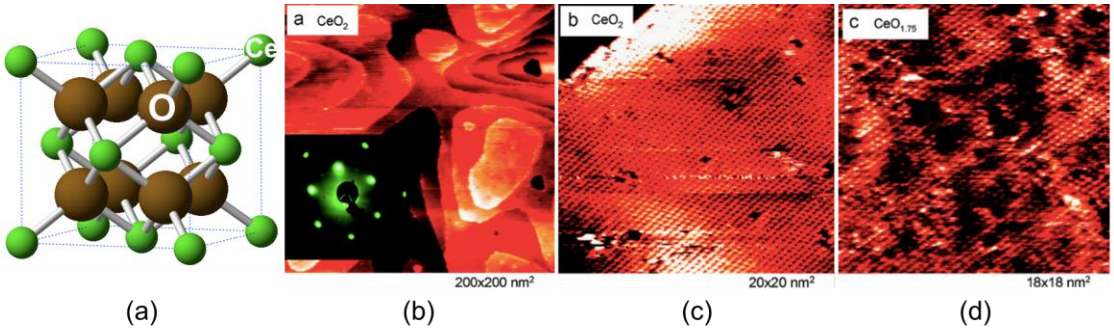

Figure 1.1. (a) Conventional unit cell for CeO_2 bulk, space group Fm3m; (b) Low-energy electron diffraction (LEED) pattern and scanning tunneling microscopy (STM) image of $CeO_2(111)$ thin film grown on Ru(0001); (c) High-resolution STM image of $CeO_2(111)$ thin film; (d) High-resolution STM image of largely reduced $CeO_{2-x}(111)$ thin film. Reprinted with permission from Zhou J et al., J Phys Chem C 112:9336-9345; © 2008 American Chemical Society

grown on conductive metals is that electron-based characterization techniques, including scanning tunneling microscopy (STM), can be applied to probe the surface [19, 20], which is not possible on bulk ceria due to its insulating nature. Along with other surface probing techniques such as atomic force microscopy [21], detailed information about the surfaces of both pristine and defective single crystal ceria has been obtained, which provides structural insights for constructing models of ceria on which to study chemical reactions theoretically. High-resolution STM images show the hexagonal structure of the (111) thin film surface (**Figure 1.1c**), and the symmetry is maintained even when the thin film surface has been largely reduced (**Figure 1.1d**).

Regarding its unique catalytic performance, the redox and acid-base properties of ceria deserve the compliments, and both properties are common features of reducible oxides [22-26]. By definition, the redox reaction consists of a reduction reaction and a complementary oxidation reaction, both of which involve an equal number of electron transfer. In terms of electron transfer, the reduction step leaves two extra electrons to ceria and each electron is backed to one Ce^{4+}. The localization of the extra electron on the Ce 4f orbital results in Ce^{3+}, which induces the volume expansion effects [27]. The acid-base property (sometimes mentioned as amphoteric property), comes from the catalyst that contains both accessible Lewis acid and base sites. For instance, on ceria surfaces, exposed Ce and O are the so-called acid and base sites, respectively. With respect to chemical reactions involving organic oxygenates e.g. $C_xH_yO_z$, the advantage of such catalyst is that the acid site can anchor and activate the functional group such as carbonyl, while the base site can activate C-H bond if α-H is available. Particularly, the ratio of available acid and base sites and their spatial distribution on the catalyst surface can fundamentally affect the activity of catalyst as well as the selectivity of corresponding surface reaction [26]. Therefore, redox and acid-base properties are closely correlated via the common oxygen component involved in the surface chemical reactions. For instance, CO oxidation (or surface reduction) not only decreases the number of surface base site, but also increases the number of accessible surface acid site via V_o formation.

From the thermodynamic perspective, the Ce-O binary system can be quite complicated in terms of possible phases it may evolve into as a function of temperature and composition [28], as shown in **Figure 1.2**. According to the phase diagram (**Figure 1.2a**), most solid phases are concentrated on the compositions with O mole fraction ranging from 3/5 to 2/3, which corresponds to a chemical formula of Ce_2O_3 and CeO_2, respectively. Indeed, redox reactions (typically below 1000 K) on catalytic materials based on ceria may transform ceria into these phases by changing the O composition between the two limiting stoichiometries during the catalytic cycle. However, identifying the active phase during the dynamic catalytic reactions remains to be a challenging task. Further zoom-in (**Figure 1.2b**) of the phase diagram shows a major stoichiometric intermediate phase called Ce_7O_{12}, which may need to be considered in both surface science and reactor condition experiments. According to previous literature, the reduction limit Ce_2O_3 phase, can be found in three different crystal structures: hexagonal (type A), monoclinic (type B), and cubic (type C, bixbyite) [27]. The bixbyite is the one most close to the fully oxidized phase CeO_2 structure-wise, because it can be constructed from 8 elementary units of CeO_2 (each unit cell of CeO_2 has 4 formula units, totally 12 atoms) with 25% of O atoms removed (therefore the unit cell of *c*-Ce_2O_3 has 80 atoms in total) [31]. Energy-wise, both

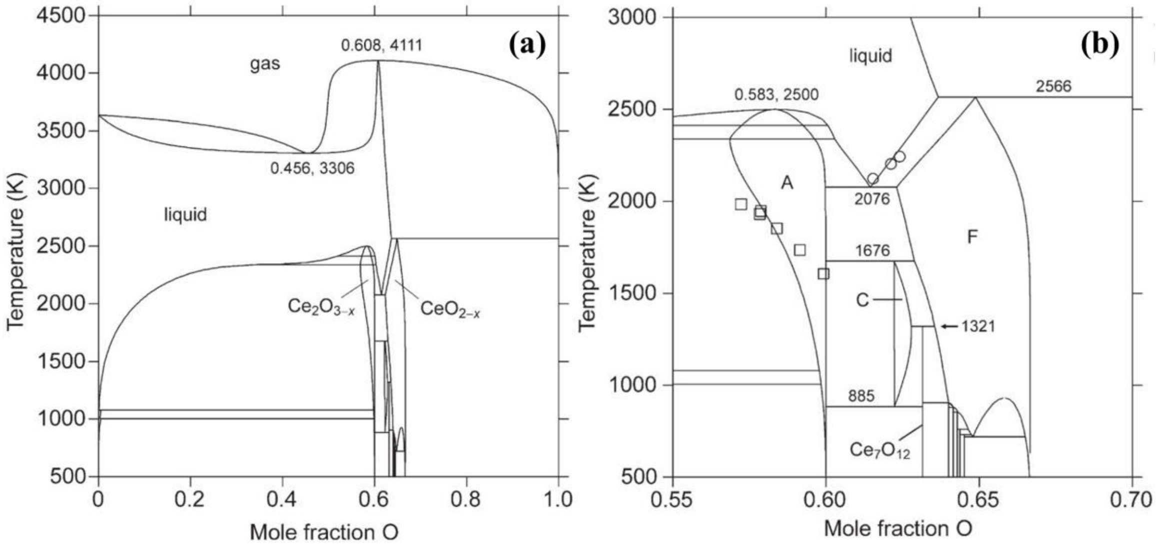

Figure 1.2. Calculated phase diagram for Ce-O binary system. Pressure condition: 1bar. Panel (b) is a zoom-in view of panel (a). The square and circle data points in panel (b) are from [29] and [30], respectively. Reprinted with permission from Zinkevich M et al., Solid State Ionics 177:989-1001; © 2006 Elsevier

hexagonal and cubic structures are more stable than monoclinic, but only the cubic structure is able to explain the volume expansion effects caused by the reduction of CeO_2 [27].

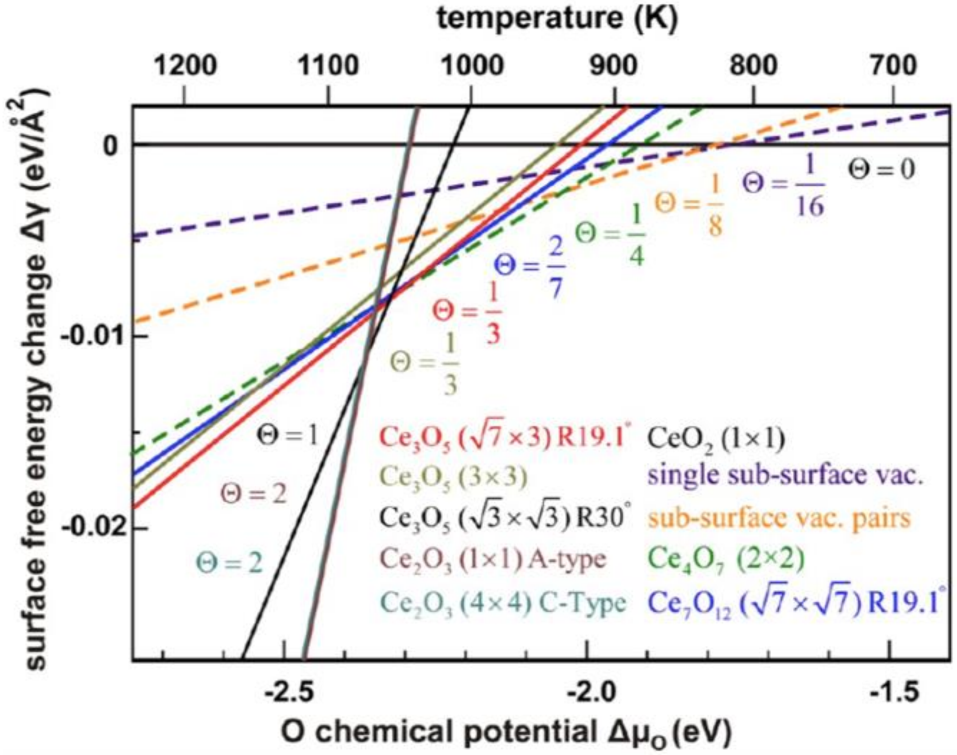

Figure 1.3. Stability plot for proposed ceria surface phases calculated by DFT and *ab initio* atomistic thermodynamic modeling. Here "**Θ**" is a quantity proportional to the extent of reduction in the surface and subsurface of the unit cell in the corresponding structure. Reprinted with permission from Olbrich R et al., J Phys Chem C 121:6844-6851; © 2017 American Chemical Society

Before reaching the reduction limit, surface reconstructions caused by oxygen vacancy ordering under 900 K annealing conditions have seen both (√7×√7)R19.1° structure with bulk termination as Ce_7O_{12}, and (3×3) structure with bulk termination as Ce_3O_5, by reducing the CeO_2(111) ultrathin film surface grown on Cu(111) via cerium deposition [32]. More recently, surface reconstruction that produces (√7×3)R19.1° structure with bulk termination as Ce_3O_5 was unveiled under higher annealing temperature by reducing the $CeO_2(111)$ thick film surface grown on Si(111) via thermal reduction method [33]. According to the calculated relative surface energy derived from *ab initio* atomistic thermodynamic modeling parameterized by DFT-calculated energetics, as shown in **Figure 1.3**, this $(\sqrt{7}\times3)R19.1^\circ$ Ce_3O_5 structure is more stable than the $(\sqrt{7}\times\sqrt{7})R19.1^\circ$ Ce_7O_{12} structure above 1040 K.

The relevance of the above findings to ceria catalysis is: during the surface catalytic reactions where dynamic O exchange between adsorbates and surface operating in a rapid rate, surface reduction/re-oxidation may cause the catalyst surface to span a relatively wide phase space under high temperature conditions. In order to better understand the structure-reactivity relationship, fundamental understanding of each primary phase and its corresponding vacancy ordering structure [34] is quite necessary. Since the surface science experiments devised by our experimental collaborators usually operates under 800 K, we would focus on point and pair defects that are much more stable than these reconstructed phases in terms of surface free energy, according to **Figure 1.3**.

1.2 Current Applications of Ceria in Heterogeneous Catalysis

Due to its electronic and structural promotion effects on catalysts, over the last two decades, ceria has been studied extensively by the catalysis communities. The conventional wisdom [35-38] for studying solid catalysts is: starting from relatively simple catalytic reaction using probe molecule on model 2D surfaces (as shown in **Figure 1.4d** and **e**), validating hypothesis about reaction mechanism and active site by complementing experimental evidence (either in reaction or UHV condition) with electronic structure calculations and microkinetic modeling; then moving on to higher dimensional space, such as model 3D particles [39] (i.e. nanoparticles, as shown in **Figure 1.4a-c**) that typically consist of multiple 2D surfaces that could potentially render synergistic effects (for instance in the interface) on the current catalytic system. Catalytic research on ceria-based materials is no exception with model catalysts ranging from low-index surfaces (generally under UHV condition) to nanoparticles [1, 2, 18, 40-42], incorporated with advanced quantum chemical techniques such as density functional theory (DFT) [43], and *ab initio* molecular dynamics (AIMD) [44, 45], as well as larger scale molecular dynamics [39, 46], in order to better understand the fundamental structures and their potential relevance to reaction mechanisms.

The most successful commercial application of ceria is probably the modern three-way converters for automotive emission control [4], where the exhaust gases of the internal combustion engine mainly consist of CO, HC (hydrocarbon), and NO_x. Due to its excellent oxygen storage capacity [47], ceria-based materials (i.e. ceria-zirconia solid solution) are used as the so-called oxygen storage material (OSM) in the modern three-way converters and mainly play the role of structural promoter for the catalytically active components [48, 49], i.e. the platinum group metals: Rh (catalyze NO_x reduction), Pt (catalyze CO and HC oxidation), and Pd (catalyze CO and HC oxidation). Due to its redox and acid-base properties, ceria can also offer catalytic activity in its own right, for instance activating C-H bond of HC. With more stringent environmental regulations on the automotive emission control standards, more efficient three-way catalysts are in high demand commercially, thus push forward the current knowledge on ceria-based materials in order to achieve such advanced technological resolution.

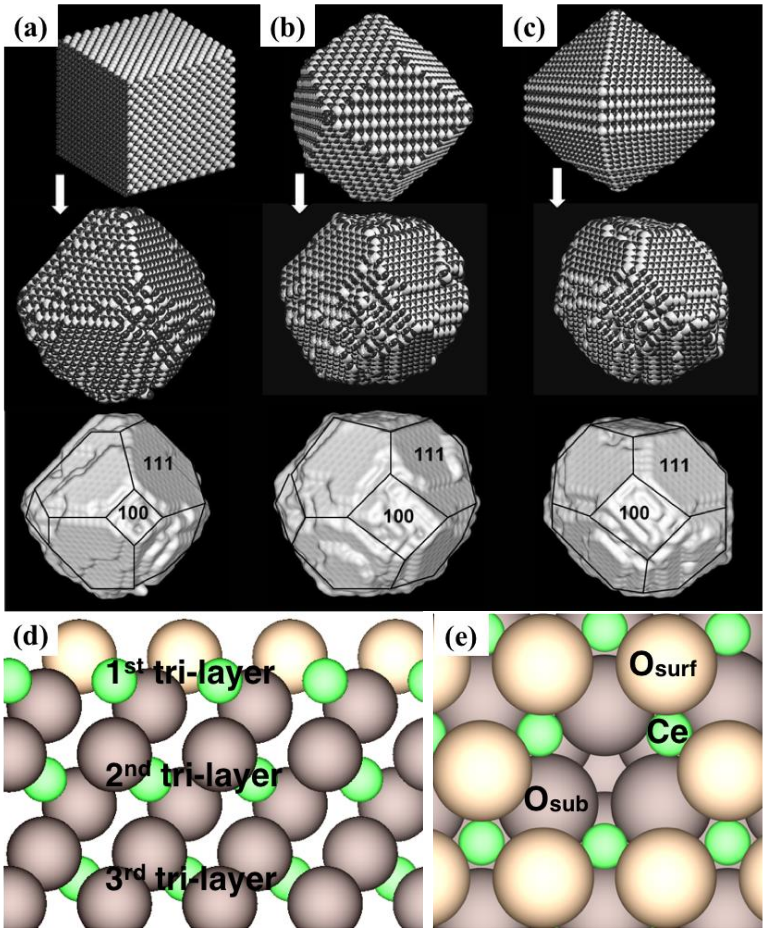

Figure 1.4. (a)-(c) Structural evolution of simulated 3D ceria nanoparticle starting from different initial structures by molecular dynamics. Reprinted with permission from Sayle TXT et al., Chem Commun 0:2438-2439; © 2004 Royal Society of Chemistry (d) and (e) refer to the side and top view of our 2D surface model CeO_2(111) with point defect V_o, respectively, with green, light and dark brown spheres represent lattice Ce, surface lattice O, subsurface lattice O, respectively. Molecular images in this figure and those below are created using VESTA [50].

One exciting potential new catalytic application for ceria is related to biomass conversion. The production of fuels and chemicals from biomass has captured significant research and commercial interest in recent decades [51-53]. Biomass is potentially a renewable, carbon-neutral source of carbon that can be supplied domestically. Biomass conversion is an indirect and more technologically achievable method to harness energy from the Sun through converting the carbon-containing compounds accumulated by photosynthesis into fuels and value-added chemicals. Biomass utilization for fuel and chemical production is a high priority research area for the U.S. Department of Energy [54, 55]. Thermal, chemical, and biological processing and conversion of biomass have been extensively explored [52].

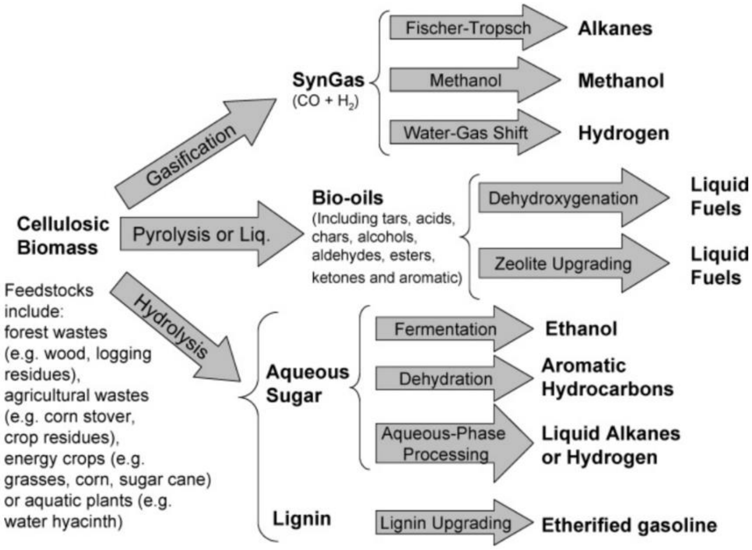

Figure 1.5. Schematic chemical conversion patterns for lignocellulosic biomass. Reprinted with permission from Huber GW and Dumesic JA, Catal Today 111:119-132; © 2006 Elsevier

As shown in **Figure 1.5**, to convert lignocellulosic biomass (cellulose, hemicellulose and lignin) at scale, it needs first to be broken down (e.g. through thermochemical and hydrolysis methods) into a mixture of small organic compounds that are rich in functionalities, and further modified and purified [56]. There are two major conversion pathways: 1) hydrogenation, which reduces the amount of heteroatoms in the feedstock and reduces the reactivity of the compounds; 2) C-C coupling to increase the size of carbon backbone and the fuel value of the molecules. For example, aqueous reforming (hydrolysis based) routes can selectively transform biomass-derived furfural, hydroxymethylfurfural (HMF) and levulinic acid as platform chemicals into liquid fuels and value-added chemicals [53]. Benefited incorporations such as Catilin (biodiesel production using mixed oxide catalyst), Velocys (microchannel reactor designed to produce fuels), ADM (production of propylene glycol), Virent (production of aromatic chemical) and GlucanBio (production of furan derivatives) have brought the technological products into market and proved the economic feasibility of biomass conversion technology.

Thanks to its acid-base and redox properties, ceria is capable of reducing as well as coupling biomass-derived organic oxygenates. C-C coupling reactions include aldol addition/condensation of aldehydes and ketones and ketonization of carboxylic acids and esters, which take advantage of functional groups such as formyl and carboxyl groups. For the aldol addition/condensation reaction, Barteau and coworkers [57] studied the reaction of acetaldehyde adsorbed on polycrystalline ceria and detected C_4 species, such as crotonaldehyde, crotyl alcohol, and reductive coupling products such as butene and butadiene. Dooley and coworkers investigated the condensation of aldehydes on ceria-based catalysts and suggested the key role of carboxylate in achieving high selectivity toward ketones [58]. Dumesic and coworkers [59] synthesized C_{12} or higher ketones from 2-hexanone, as shown in **Figure 1.6**, under reactor conditions (350 ℃, 5 bar) using a palladium catalyst supported on $CeZrO_x$, and they also found that the selectivity of products can be controlled by changing the relative composition of the mixed oxide. Resasco and coworkers [60] used $Ce_xZr_{1-x}O_2$ catalyst for propanal condensation under 400 ℃ with the presence of He or H_2. Cosimo [61] investigated the formation of methyl isobutyl ketone from 2-propanol on $CuCe_4O_x$ catalyst.

Ketonization of carboxylic acids or esters is potentially a green chemistry process, since it does not require the usage of solvents or other elaborate reagents [62]. Dumesic group used $Ce_{0.5}Zr_{0.5}O_2$ catalyst for the ketonization of hexanoic acid [63], with other oxygenates (ketone/alcohol) presented, where 6-undecanone (C_{11} ketone) is observed under high temperature

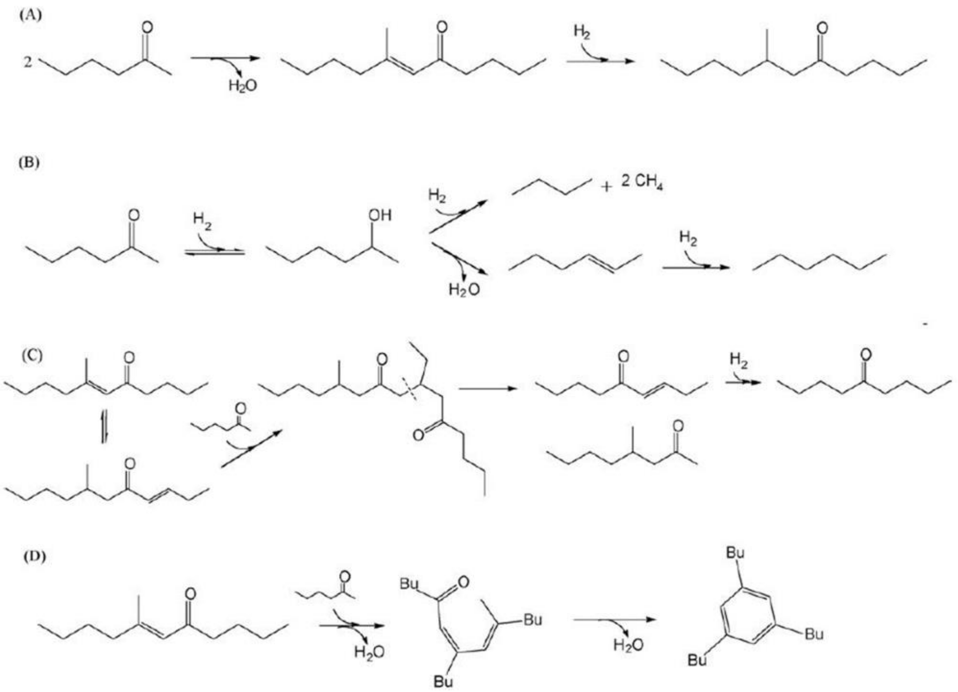

Figure 1.6. Conversion of 2-hexanone on $CeZrO_x$ supported Pd catalyst. Reprinted with permission from Gürbüz EI et al., Appl Catal B-Environ 94:134-141; © 2010 Elsevier

regime. Dooley and coworkers carried out a series of studies on ceria-based catalysts and proposed a ketonization mechanism where a surface ketene intermediate is involved that suggests the necessity of having α-H [58, 64, 65]. More recently Resasco and coworkers further elaborated the mechanism, originally proposed by Neunhoeffer and Paschke [66], which involves a β-keto-acid intermediate [67], as shown in **Figure 1.7**. To be noted, the pathway that involves β-keto-acid intermediate proposes that carbon dioxide originally comes from the enolate form (CH_2COOH) of acetic acid [68], which is formed via α-H abstraction.

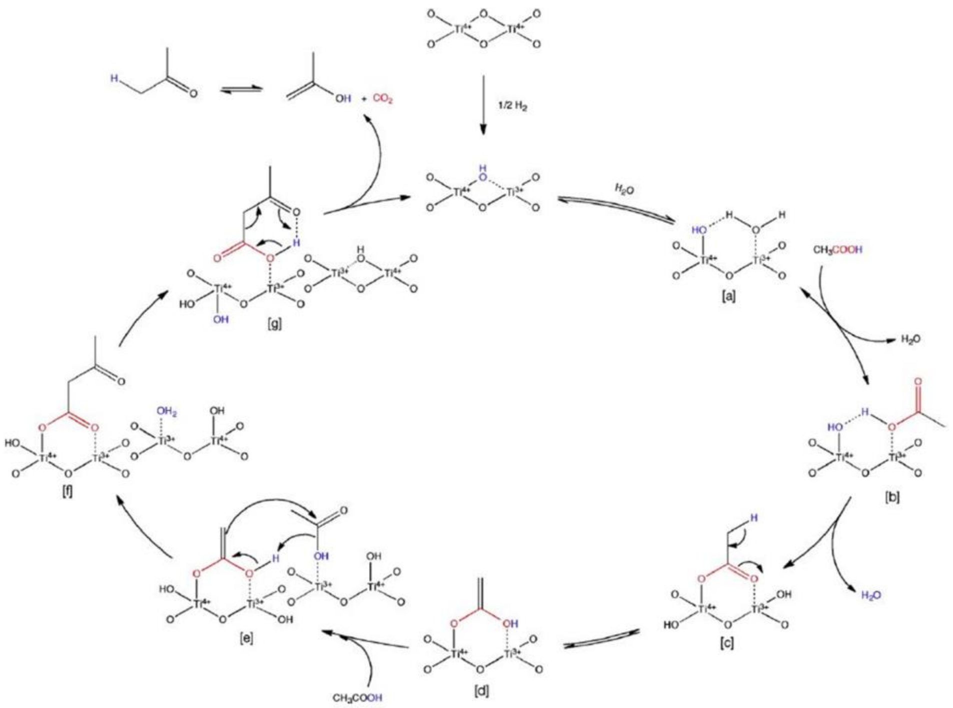

Figure 1.7. Liquid phase ketonization of carboxylic acid over TiO_2 catalyst. Reprinted with permission from Pham TN et al., J Catal 295:169-178; © 2012 Elsevier

Despite the above mentioned efforts, among others, selective conversion of organic oxygenates on ceria has not been achieved by traditional catalytic experiments, partly due to the less realistic models for the catalyst and catalytic active sites, partly due to the difficulty of measuring sufficiently accurate kinetic parameters in a consistent way, for instance counting the number of catalytic sites [69]. Surface science studies can provide fundamental insights for catalytic reactions conducted on the well-defined model surfaces under ultrahigh vacuum (UHV) condition. As one of the benefits, relatively more clear and consistent spectroscopic evidence can be generated, which can be further compared with simulated spectra from microkinetic modeling parameterized by accurate kinetic inputs with clear microscopic meaning such as DFT calculated energetics. Particularly, highlights from a series of surface science studies carried out by Overbury, Mullins and coworkers [70-76] show that on $CeO_2(111)$ thin film surfaces, as shown in **Figure 1.8**, acetaldehyde (AcH) seems to be only reactive on the partially reduced

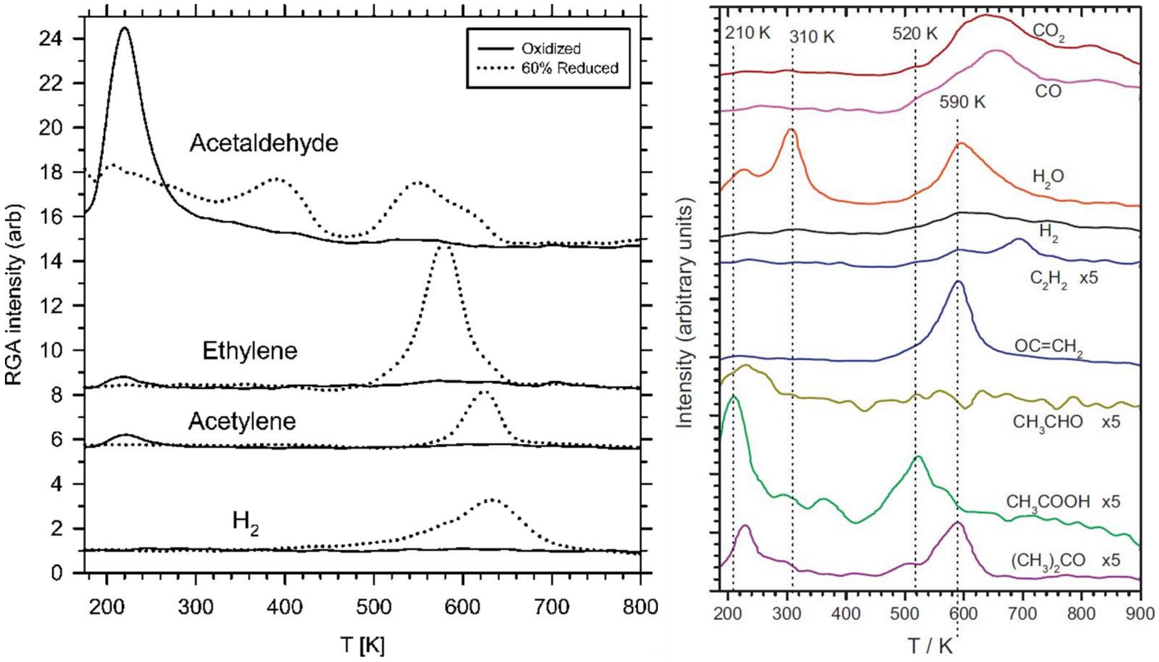

(a) **(b)**

Figure 1.8. (a) Temperature-programmed desorption of acetaldehyde adsorbed on fully oxidized and partially reduced $CeO_2(111)$ thin film surfaces. Reprinted with permission from Chen TL and Mullins DR, J Phys Chem C 115:3385-3392; © 2011 American Chemical Society (b) Temperature-programmed desorption of acetic acid adsorbed on fully oxidized $CeO_2(111)$ thin film surface. Reprinted with permission from Calaza FC et al., Catal Today 253:65-76; © 2015 Elsevier

surface, with no crotonaldehyde or other C_4 species detected, but C_2 species (C_2H_4, C_2H_2 and AcH) and molecular H_2 observed in the temperature programed desorption (TPD) spectra [73]. Combined with DFT calculations [75], they were able to show that acetaldehyde adsorbs very weakly on the fully oxidized surface, and surface oxygen vacancy as the proposed active site can bind acetaldehyde much more strongly and activate the carbonyl bond, which shifts to a single bond and liberates the C atom to further engage in bonding with a nearby surface AcH (η-AcH). This leads to the formation of a C-O dimer state (denoted as D/VV_o). Reflection-absorption IR spectroscopy (RAIRS), together with DFT simulated IR, identified the existence of this surface dominant species around 300 K during the AcH-TPD experiment. As temperature further increases, this C-O dimer decomposes and forms the enolate (CH_2CHO, denoted as Enl/V_o) of AcH and simultaneously releases a AcH molecule back to the gas phase under UHV condition [75]. The existence of Enl/V_o has been confirmed by RAIRS and DFT simulated infrared spectra, which shows it is the dominant surface species between ca. 400 and 600 K [75, 77].

As part of our early scientific discoveries, which will be further explained in Chapter 3, detailed mechanistic picture about the formation of various C_2 products in the temperature programmed desorption of AcH adsorbed on the partially reduced $CeO_{2-x}(111)$ surface can be acquired [77]. However, a big discrepancy exists after comparing with the AcH temperature programmed surface reaction (TPSR) on various CeO_2 nanoshapes under flow reactor conditions [78], where appreciable amount of coupling products such as crotonaldehyde has been detected, which does not appear in the previous surface science studies under UHV condition [73]. The lack of C_4 product in the typical "single-ramping" TPD procedure [73], as further discussed in Chapter 3, is because the surface is dominated by isolated enolate species from ca. 400 K to 600 K. Our most recent scientific discovery devising a tailored "double-ramping" TPD procedure successfully captured the formation of crotonaldehyde under UHV condition. The idea behind the "double ramping" procedure is to take advantage of the facile migration of oxygen vacancies once they are vacant via the desorption of adsorbate. Built upon the general TPD reaction mechanism as proposed in our earlier findings [77], three expanded TPD reaction mechanisms are proposed and investigated in detail to account for the formation of crotonaldehyde in this “double-ramping” TPD procedure. Density functional theory (DFT) calculated energetics are fed into corresponding mean-field microkinetic model that is able to generate simulated TPD spectra, which can be directly compared with the experimental TPD spectra. Once again, this DFT+MkM methodology is found to be very helpful for validating our mechanistic hypothesis.

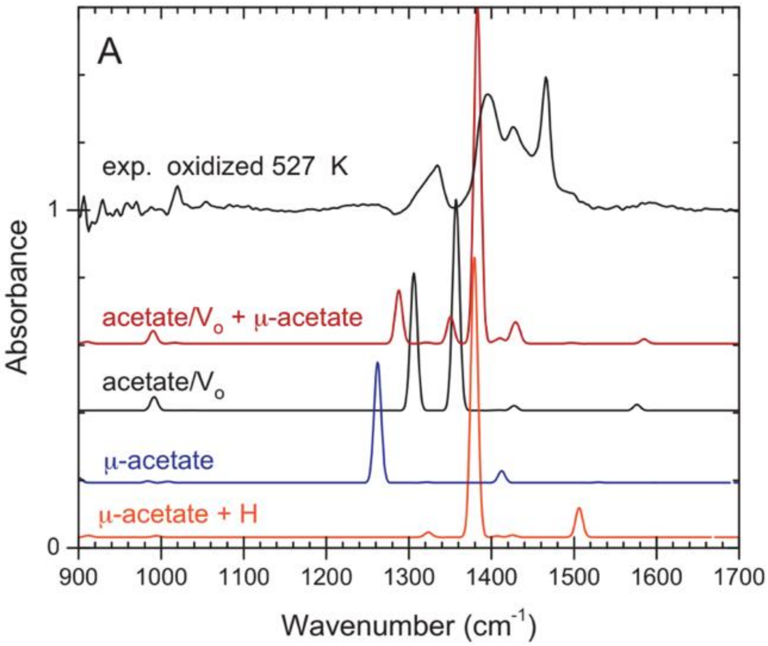

Figure 1.9. Comparison of experimental and DFT-calculated IR spectra for acetates with different local environments on fully oxidized $CeO_2(111)$ thin film surface. Reprinted with permission from Calaza FC et al., Catal Today 253:65-76; © 2015 Elsevier

Oxygenates with different functional groups can introduce dramatic differences in terms of surface chemistry on ceria. For instance, acetic acid (AA) can be quite reactive even on the fully oxidized $CeO_2(111)$ thin film surface, with major products including ketene, water, CO and CO_2 , while acetone is only a minor product, as shown in the TPD spectra in **Figure 1.8b** [76]. On the other hand, as discussed earlier, AcH is not able to do so given the same surface. Earlier findings show that one big difference at the initial stage of TPD is acetic acid can reduce the fully oxidized surface around 300 K [76]. This surface reduction step forms a vacancy stabilized acetate species (denoted as Ata/V_o) that can stay on the surface until above 500 K, providing enough carbon supply for the subsequent C-C coupling step. As shown in **Figure 1.9**, this argument is validated by the fact that DFT-calculated IR spectra of acetates with different local environments overlap with the experimental RAIRS spectra under 527 K. To be noted, DFT-calculated IR modes are usually red-shifted compared with the corresponding experimental IR modes, and their dependence on the magnitude of U is negligible [71]. Dwelled upon earlier proposed mechanisms for ketonization of carboxylic acids on reducible oxides, our proposed ketonization pathway on the fully oxidized $CeO_2(111)$ surface involving both surface bent ketene and oxygen vacancy stabilized β-keto acid will be explored in detail in Chapter 3.

As one of the minor components in biomass, phosphorous (P) is quite often used as agricultural fertilizer and is critical for food production [79]. However, phosphorite (phosphate rock) is a nonrenewable resource and is distributed quite unevenly from a geographic perspective, which undoubtedly limit the production of P-containing fertilizer, therefore imposing serious threats to human society [80]. On the other hand, quite a few phosphate-containing anthropogenic wastes do not receive enough notice in terms of recycling, such as agricultural runoff, industrial wastewater, and human sewage. As a result, eutrophication problems have been created and threaten aquaculture industries as well as potable water resources [81]. For instance, organophosphates (OPs), which are found in many consumer, industrial, and agricultural chemical products, can be found in the above mentioned wastes and often possess toxicity to animals and even humans. Removal of P from such wastes as well as extraction of P from biomass feedstock constitutes important steps in sustainable P use [82]. Environmental necessity and economic and technological feasibility of such methods suggest that the further development of and support for sustainable P use need to be on the agenda of policymakers today [83].

The degradation of OPs in the environment can take months and even years [84, 85]. The hydrolysis of the P-O ester bond by microbes is the primary pathway for OP degradation in nature [86]. Earlier studies have demonstrated promising catalytic activities of cerium oxide nanoparticles toward aqueous-phase dephosphorylation, i.e. hydrolysis, of organic and biological compounds including phosphopeptides, *para*-nitrophenyl phosphate (*p*-NPP), ATP, and phospho-tyrosine [87, 88] that parallel the function of phosphatases. Recently, Janos et al. suggested that ceria-based reactive sorbents can promote the dephosphorylation of several OP pesticides and chemical warfare agents, which opens up a new frontier for ceria in environmental catalysis and may be relevant to large-scale environmental application of P recovery technologies [89, 90]. Manto et al. very recently studied the catalytic dephosphorylation of *p*-NPP using different ceria nano-shapes in deionized water, among which nano-spheres (ca. 4 nm; no preferential exposed facet) showed the highest catalytic activity, followed by nano-octahedra (ca. 18 nm), which primarily expose (111) facets [91]. Although extensive experimental and theoretical studies have been reported in the literature that examine the hydrolysis mechanism of phosphate esters in aqueous solutions or by enzymatic complexes [92-99], the understanding of the dephosphorylation process on solid surfaces remains incomplete [100-104].

Hydrolysis of phosphate esters in water has been extensively studied theoretically [93-99]. In general, as suggested by Warshel and coworkers [94-98], based on potential energy surfaces parameterized by two characteristic P-O bond distances (i.e., d(P-O_{NU}) and d(P-O_{LG}), where O_{NU} refers to the O atom of the nucleophile (i.e. water), and O_{LG} refers to the O atom of the leaving group), the hydrolysis mechanisms of phosphate monoesters in water fall into three major categories: 1) the associative type, where the nucleophilic attack occurs first forming an intermediate complex with a pentavalent P center, followed by a second transition state corresponding to the P-O_{LG} bond scission; 2) the dissociative type, where the leaving group departs before the nucleophilic attack and formation of the P-O_{NU} bond; 3) the concerted type, where the reaction proceeds via a single transition state with both P-O_{NU} and P-O_{LG} bonding characters [95, 99]. The mechanistic preference appears to be influenced by the pK_a of the leaving group in water, with poor leaving groups (high pK_a) favoring associative mechanisms and good leaving groups (lower pK_a) favoring dissociative mechanisms [95, 99]. Among others, Florián et al. used Hartree-Fock (HF) and second-order Møller-Plesset perturbation theory (MP2) together with the Langevin dipoles (LD) model as well as the polarized-continuum model (PCM) to study the hydrolysis of neutral, mono-anionic, and di-anionic MP [94]. A more recent example is the work of Duarte et al., who used the M06-2X and ωB97X-D density functionals and a mixture of implicit/explicit solvent models to investigate the hydrolysis of the di-anions of several aryl phosphate monoesters as well as MP in water [99]. The hydrolysis of the neutral MP is found to preferentially proceed via an associative mechanism, while the associative and dissociative mechanisms are competitive for the mono-anionic and the di-anionic MP [94]. The highest activation free energies for the hydrolysis of neutral, mono-anionic, and di-anionic MP were reported by Florián et al. to be 1.52, 1.73, and 1.65 eV in MP2+LD, and by Duarte et al. to be 1.54 eV in M06-2X and 1.74 eV in ωB97X-D for di-anionic MP. On the other hand, Duarte et al. found di-anionic *p*-NPP to prefer a concerted mechanism with a single barrier calculated to be 1.18 eV in M06-2X and 1.08 eV in ωB97X-D [99], and they reported a threshold pK_a value of ca. 12, below which the hydrolysis of a phosphate monoester di-anion prefers a concerted mechanism, and above which an associative mechanism would prevail [99].

The dephosphorylation and following hydration of model phosphate monoesters, including *p*-NPP and methyl phosphate (MP), on fully oxidized $CeO_2(111)$ in vacuo is studied here systematically, in order to shed light on the factors controlling the kinetics of this reaction and to help establish the range of OPs the dephosphorylation of which ceria may effectively catalyze under mild or ambient conditions. The OPs are modeled in their neutral forms ($PO(OH)_2OR$) in this work, e.g. *p*-NPP-H_2 and MP-H_2, which are the predominant forms in acidic to neutral conditions [93, 105]. The deprotonated forms (i.e., the mono-anionic *p*-NPP-H_1/MP-H_1 and di-anionic p-NPP-H_0/MP-H_0) that prevail in neutral to basic solutions [106] will be considered in a future study. The dephosphorylation of *p*-NPP is of interest because it is accompanied by visible color change of the solution, which allows the reaction kinetics to be readily analyzed using ultraviolet-visible (UV-Vis) absorption spectroscopy [91]. By comparison, MP is the simplest organic phosphate monoester and is used here to explore how the leaving group affects the activation of the P-O ester bond. Moreover, a linear transition state scaling relation is proposed after considering several additional organic phosphate monoesters, including para-chlorophenyl phosphate (*p*-ClPP), phenyl phosphate (*p*-HPP), 2-pyridyl phosphate (2-py-P), and chloro-methyl phosphate (Cl-MP). The formation and desorption of the resulting alcohol species (i.e. para-nitrophenol (p-NP) or 4-nitrophenol from *p*-NPP, and methanol from MP) are facile and therefore kinetically insignificant.

TECHNICAL APPROACH

2.1 Density Functional Theory Calculations

Periodic, spin-polarized DFT calculations were performed using the Vienna Ab initio Simulation Package (VASP) [107] in the generalized gradient approximation (GGA) using the Perdew-Wang (PW91) exchange-correlation functional [108]. The optB86b van der Waals (vdW) functional was used to estimate the vdW contribution in the adsorption of AcH and CrA [109, 110]. The projector-augmented wave method (PAW) was used to describe the core electrons [111], and the Kohn–Sham valence states [Ce(*5s5p4f5d6s*), Cl(*3s3p*), P(*3s3p*), O(*2s2p*), N(*2s2p*), C(*2s2p*), H(*1s*)] were expanded in a plane wave basis set with a kinetic energy cutoff of 400 eV.

The adsorption energy of an atom or molecule was calculated as $\Delta E_{ads} = E_{total} - E_{slab} - E_{gas}$, where E_{total}, E_{slab}, E_{gas} refer to the energy of the slab with the adsorbed atom or molecule, the energy of the clean surface, and the energy of the atom or molecule in the gas phase in a neutral state, respectively. Thus, the more negative the value of ΔE_{ads} is, the stronger the adsorption is. The minimum energy reaction path for each proposed elementary step and the associated transition state (TS) were determined using the climbing-image nudged elastic band method [112, 113] and dimer method [114, 115]. The activation energy was calculated as $E_a = E_{\mathrm{TS}} - E_{\mathrm{IS}}$, where E_{TS} and E_{IS} refer to the energy of the transition state and corresponding initial state, respectively. The corresponding reaction energy of an elementary step is $\Delta E_{\mathrm{rxn}} = E_{\mathrm{FS}} - E_{\mathrm{IS}}$, where E_{IS} and E_{FS} refer to the energy of the initial and final state of the elementary step, respectively. Both geometry optimization and transition state search were converged to the extent that the maximum residual force was 0.01 eV/Å or less in all relaxed degrees of freedom. The singlet-triplet/doublet-quadruplet splitting was checked, and the lower adsorption energy for an adsorbate and the lower activation energy for an elementary reaction step (at constant spin) are reported below. Transition states were verified to possess only one vibrational mode with a negative curvature in the direction of the bond breaking or forming process. Vibrational modes and frequencies were calculated using a finite difference approximation approach of the dynamical matrix with a displacement of 0.01 Å. If not specified, the ΔE_{ads}, E_a, and ΔE_{rxn} values were calculated on $p(2\times2)$ surface unit cells. The values reported in the main text are based on DFT total energies only, while zero-point energy (ZPE) and free energy corrections were applied in the microkinetic models.

The DFT+U formalism of Dudarev et al. [116] was used to partially offset the 4f electron delocalization error in DFT at the GGA level [117]. A U value of 2 eV was used based on our previous studies of similar reaction systems on $CeO_2(111)$ [71, 75], which found that larger U values in combination with DFT-GGA gave less accurate predictions of reaction kinetics based on Redhead analysis [118] when compared to the peak desorption temperatures observed in TPD. Small U values ($\lesssim$ 2 eV) have also been recommended by other authors [119, 120] based on comparison with experimental reaction energetics, although large U values ($\gtrsim$ 4eV) are generally recommended based on theoretical electronic structure arguments [121, 122]. The equilibrium lattice constant of the CeO_2 bulk was calculated to be 5.476 Å on a (15×15×15) Monkhorst-Pack k-point grid at U=2 eV, in close agreement with previous experimental and computational values [43].

As shown in **Figure 2.1**, the $CeO_2(111)$ surface was modeled primarily with a slab consisting of three O-Ce-O tri-layers, with the top tri-layer of the slab and adsorbate fully relaxed, and the remaining two tri-layers fixed at the bulk positions. Size of surface unit cell was chosen to be sufficient to accommodate model compounds. The slab was separated from its periodic images in the z direction by ~12 Å of vacuum. Adsorption was studied only on one side of the slab, with dipole decoupling [123] in the *z* direction. The $CeO_2(100)$ surface is not trivial to model due to its polar nature, a checkboard pattern model with half O atoms of both top and bottom anion terminated layers removed was proposed in order to cancel off the surface perpendicular dipole [124-126], and our model of $CeO_2(100)$ with 11 atomic layers and a *p*(2×2) surface unit cell follows this methodology, so do others [127, 128].

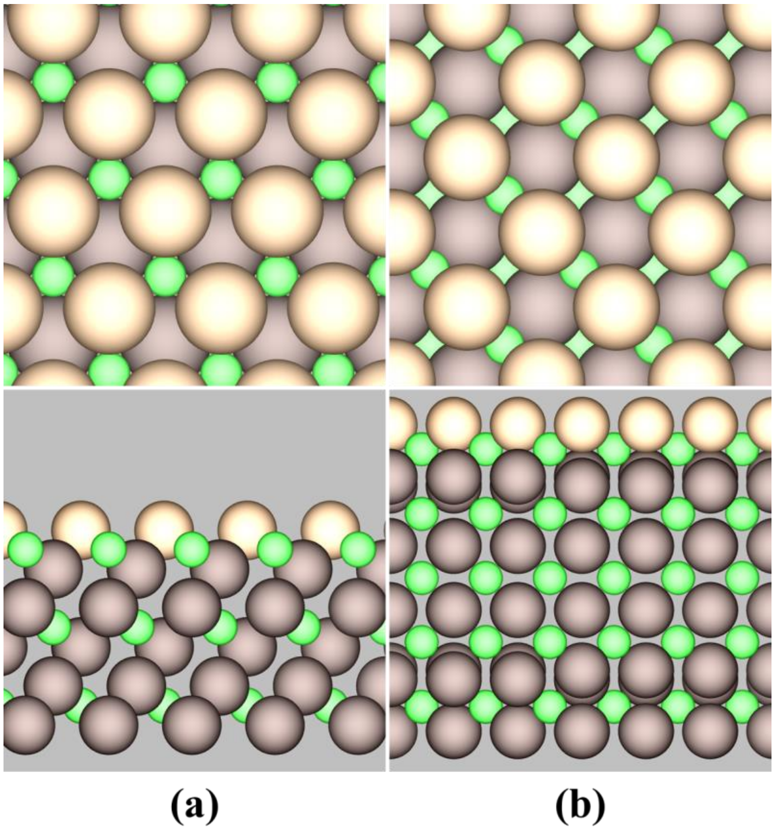

Figure 2.1. Model fully oxidized ceria surfaces used in our studies, top view is on top and side view is on bottom: (a) 9 atomic layer $CeO_2(111)$, (b) 11 atomic layer $CeO_2(100)$. Green, light and dark brown spheres represent lattice Ce, surface lattice O, subsurface lattice O, respectively.

The exact structure of the CeO_{2-x}(111) thin films used in the TPD experiment (i.e. $CeO_{1.70}$) [73] was not investigated by Chen et al. STM images of $CeO_{1.75}$(111) thin films reported in a separate study by Zhou et al. [20] showed an ordered hexagonal CeO_2 lattice with both isolated and patches of dark depressions, presumably oxygen vacancies. If the outermost O-Ce-O tri-layer had a composition of $CeO_{1.70}$, it would correspond to 60% of the Ce atoms being in the 3+ oxidation state, or 30% of the O atoms being missing. At the upper limit, if all of the oxygen vacancies are located in the surface O layer, it would correspond to a coverage of 0.30 ML for oxygen vacancies. It should be noted that the clustering of oxygen vacancies reported [129] in CeO_2(111) surfaces cut from natural CeO_2 crystals has been called into question recently, due to possible mistaken identity for naturally occurring fluorine contamination [130].

For the AcH-TPD and AA-TPD modeling part, we used point oxygen vacancy (V_o) as the main vacancy model, which corresponds to one oxygen vacancy per (2×2) surface unit cell (i.e. 0.25 ML vacancy coverage) where a Γ-centered 2×2×1 Monkhorst-Pack k-point grid was used to sample the surface Brillouin zone [131]. The energetics of different V_o ensembles were determined on p(4×4) surface unit cells where the k-point grip was sampled at the Γ-point only. For the dephosphorylation of *p*-NPP modeling part, we used a *p*(3×3) surface unit cell consistently where a Γ-centered 2×2×1 Monkhorst-Pack k-point grid was used.

The projected density of states (*p*DOS, 3×3×3 Monkhorst-Pack k-point grid) calculations for bulk CeO_2 and *c*-Ce_2O_3 (bixbyite) were based on the Heyd-Scuseria-Ernzerhof (HSE06) hybrid functional [132], and the corresponding optimized lattice constants were calculated to be 5.40 Å (11×11×11 Monkhorst-Pack k-point grid) and 11.20 Å (Γ-point only Monkhorst-Pack k-point grid, antiferromagnetic state), respectively. The band gap between O *2p* and Ce *4f* was calculated to be 3.5 eV for bulk CeO_2, and the Ce *4f* - *5d* band gap was calculated to be 2.6 eV for *c*-Ce_2O_3. Therefore, the key results of our electronic structure calculations are in good accordance with previous literature: CeO_2, 5.41 Å lattice constant (experiment [133], calculation [134]), O *2p* - Ce *4f* band gap (experiment: 3 eV [135], calculation: 3.3 eV [134]); *c*-Ce_2O_3, 11.16 Å lattice constant (experiment [136]), Ce *4f* - *5d* band gap (experiment: 2.4 eV [137]). In order to simulate the resonant-on mode of the angle-resovled RPES experiment, core-level (*4d*) electron excitation was done using the method of Köhler and Kresse [138].

2.2 Microkinetic Modeling

To simulate the TPD process, a reaction mechanism was proposed that consisted of a series of surface reaction steps and desorption steps. In accordance with the TPD experiment of Chen et al. [73], adsorption was assumed to occur before the temperature ramp and therefore not modeled directly. The TPD process was mathematically modeled using a set of differential equations that expressed the rate of change for the coverage of each surface species, *i*, as:

$$\frac{d\left(\theta_i/\theta^\circ\right)}{dt} = \sum_j \alpha_j\left(r_{f,j} - r_{r,j}\right)$$

where α_j is the stoichiometric coefficient of species *i* in step *j*, being positive if *i* is a product and negative if *i* is a reactant in step *j*; r_j is the forward reaction rate of step *j*, being equal to $r_{f,j} = k_{f,j}\prod_k \left(\theta_k/\theta^\circ\right)^{|\alpha_k|}$ where the product includes all the reactants of step *j* (the reverse rate is similarly defined); and θ^o is the standard coverage at which the activation barriers and reaction energies are calculated (1/4 ML in this study). This set of differential equations was solved together with $\sum_i \theta_i = 1$, which includes the coverage of empty sites (θ_*).

For a *reaction* step, the forward reaction rate constant was calculated based on harmonic transition state theory approximations (neglecting *pV* effects) [139]:

$$k_f = \frac{k_B T}{h} \cdot e^{\frac{-G_a}{k_B T}} = \frac{k_B T}{h} \cdot e^{\frac{S_a}{k_B}} \cdot e^{\frac{-U_a}{k_B T}} = \nu \cdot e^{\frac{-U_a}{k_B T}}$$

where the subscript "*a*" indicates an activation quantity calculated as the difference between the TS and the initial state (IS) of a reaction step, and ν is the pre-factor. The free energy of an adsorbed species (including surface TSs) was calculated as [140, 141]:

$$G = U - T \cdot S(T) = E^{DFT} + E^{ZPE} + \Delta E(T) - T \cdot S(T)$$

where E^{DFT} is the DFT-calculated total energy, E^{ZPE} is the zero point energy, ΔE is the change in internal energy with respect to temperature, and S is the entropy. E^{ZPE}, ΔE, and S were calculated from the fundamental vibrational frequencies (ν_i) of an adsorbed species as:

$$E^{ZPE} = \frac{1}{2} \sum h\nu_i$$

$$\Delta E(T) = k_B T \sum \frac{\Theta_i}{e^{\Theta_i} - 1}$$

$$S(T) = k_B \sum \left(\frac{\Theta_i}{e^{\Theta_i - 1}} - \ln(1 - e^{-\Theta_i}) \right),$$

where $\Theta_i = \frac{h\nu_i}{k_B T}$, and k_B and h are the Boltzmann constant and Planck constant, respectively. The mode with the negative curvature was excluded from the calculation for TS's. The corresponding reverse reaction rate constant was calculated via the equilibrium constant, where ΔG is the reaction free energy:

$$K_{eq} = e^{\frac{-\Delta G}{k_B T}} = \frac{k_f}{k_r}$$

The *desorption* steps were all taken to be irreversible (forward direction only) under UHV condition. For the molecular desorption of AcH and CrA, the activation barrier was taken to be the negative of its ΔE_{ads} (i.e. no activation barrier for the corresponding adsorption process). A typical value of 10^{13} was used as the pre-factor. A reactive desorption step (i.e. C-O bond scission releasing C_2H_x to gas phase), was treated as a reaction step, not a desorption step.

RESULTS AND DISCUSSION

Previous experiments have shown that ceria can be beneficial towards C-C coupling of aldehydes/carboxylic acids, however the reaction mechanism and active sites remain unclear, which impedes finding better or novel catalysts for upgrading biomass-derived oxygenates. Ceria as a catalyst for recovering phosphorus from phosphates is possible but also poorly explored or understood, which is of high importance partly because phosphorus is a nonrenewable resource and because organophosphates are the main ingredients of many agricultural chemicals. Both areas require fundamental insights to enable practical applications based on ceria. In the following sections[1], we used relevant model compounds, AcH, AA and *p*-NPP, to discover the catalytic mechanisms for adol addition, ketonization, and dephosphorylation reactions, respectively, primarily on model $CeO_2(111)$ surfaces that are thermodynamically the most stable low-index facet and prevail on ceria nano-octahedra [142].

3.1 Transformations of Acetaldehyde and Acetic Acid on $CeO_2(111)$

Previously, Overbury and coworkers proposed and validated a preferred C-O dimerization pathway leading to enolate formation after AcH adsorption on partially reduced $CeO_{2-x}(111)$

---

[1] This chapter contains four previously published articles: 1) C. Zhao et al., “Simulated Temperature Programmed Desorption of Acetaldehyde on $CeO_2(111)$: Evidence for the Role of Oxygen Vacancy and Hydrogen Transfer,” *Top Catal* 60 (2017): 446-458. Copyright 2017 Springer Nature; 2) C. Zhao et al., “Coupling of Acetaldehyde to Crotonaldehyde on $CeO_{2-x}(111)$: Bifunctional Mechanism and Role of Oxygen Vacancies” *J Phys Chem C* XXX (2018): XXX-XXX. Copyright 2018 American Chemical Society; 3) C. Zhao et al., “Theoretical Investigation of Dephosphorylation of Phosphate Monoesters on $CeO_2(111)$” *Catal Today* 312 (2018): 141-148. Copyright 2018 Elsevier; 4) Duchoň T. et al., “Covalent versus Localized Nature of 4f Electrons in Ceria: Resonant Angle-Resolved Photoemission Spectroscopy and Density Functional Theory” *Phys Rev B* 95 (2017): 165124. Copyright 2017 American Physical Society, are reprinted (adapted) here by permission of Springer Nature, American Chemical Society, Elsevier, and American Physical Society, respectively.

[75]. The structures of several reaction intermediates, such as surface adsorbed AcH (AcH*), vacancy stabilized AcH (AcH/V_o), vacancy dimer stabilized C-O dimer state (D/VV_o), and vacancy stabilized enolate (CH_2CHO, Enl/V_o) have been proposed, as shown in **Figure 3.1**. AcH* preferentially adsorbs in the η^1 configuration with the carbonyl O located above a threefold hollow site above a second layer Ce cation, and the carbonyl H pointing toward a surface lattice O (**Figure 3.1a**). It has a C-C bond length ($d_{C\text{-}C}$) of 1.492 Å and a $d_{C\text{-}O}$ of 1.228 Å, nearly identical to those of AcH in the gas phase (1.484 and 1.219 Å, respectively), and a ΔE_{ads} of -0.25 eV (relative to gas-phase AcH). The adsorption energies and the C-C and C-O bond lengths of the various C_2H_xO species investigated in this study are summarized in **Table 1**. AcH adsorbs more strongly in an oxygen vacancy (AcH/V_o; **Figure 3.1b**), with ΔE_{ads} = -1.11 eV. The $d_{C\text{-}C}$ is slightly shorter (1.486 Å), whereas the $d_{C\text{-}O}$ is longer (1.305 Å) than AcH*, indicating interaction with the oxygen vacancy and partial rehybridization of the C=O bond. Polymeric AcH has been explored in our previous study [75] due to earlier reports of AcH forming C-O linked polymers on metal and oxide surfaces at low temperatures [143, 144]. A representative structure that most closely matches the observed RAIR spectrum at 300 K involves the coupling of the carbonyl C of AcH/V_o to the carbonyl O of AcH*, followed by the bonding of the carbonyl C of the AcH* to a surface lattice oxygen, creating a O-C-O-C-O linkage (**Figure 3.1c**). This dimer state is more stable than both AcH* and AcH/V_o, with a ΔE_{ads} of -1.37 eV per AcH unit. The carbon-surface oxygen bonds are at ~1.40 Å, and the C-O bonds in the middle of the linkage are at ~1.47 Å. Longer polymeric states formed in a similar way may be present but have not been studied. The enolate of AcH (Enl/V_o; **Figure 3.1d**) has been found to match the observed IR spectrum at 400 K, and is consistent with sXPS and EXAFS evidence that the α-C becomes more negatively charged when temperature was ramped up from300 K to 400 K [73].

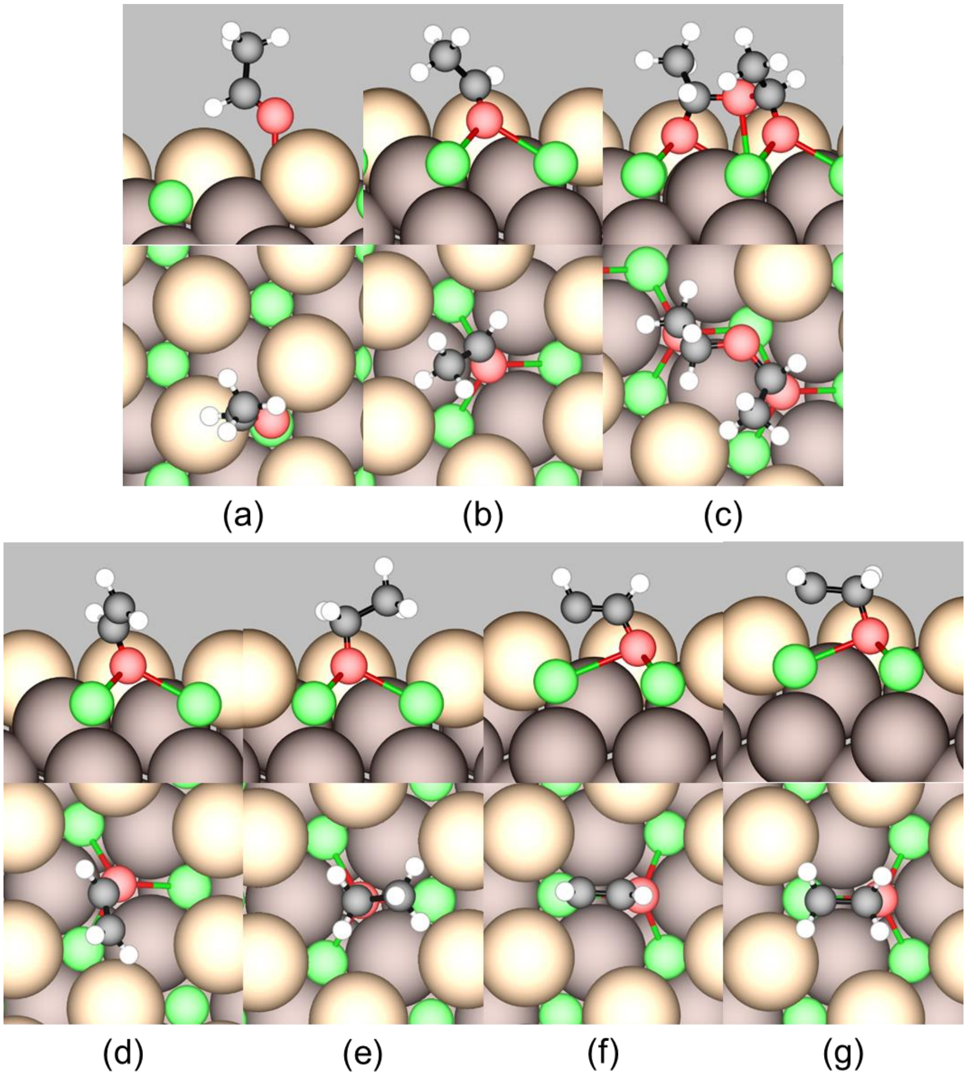

Figure 3.1. (Top) top view and (bottom) side view (from the bottom side of the top view) of DFT-calculated minimum-energy structures of (a) AcH*, (b) AcH/V_o (c) D/VV_o, (d) Enl/V_o, (e) Etx/V_o, (f) CHCHO/V_o, and (g) CH_2CH_2O/V_o on $CeO_{2\text{-}x}$(111). Green, light brown, dark brown, red, black, and white spheres represent lattice Ce, surface lattice O, subsurface lattice O, O in molecules, C, and H atoms, respectively. Surface lattice O atoms bonded to C atoms in the molecules are considered part of the molecules. Periodic images of the adsorbates have been removed for clarity.

The carbonyl C-O bond is lengthened to 1.352 Å, whereas the C-C bond is noticeably shortened to 1.346 Å, consistent with being a C=C double bond which confirms the enolate species [75]. Compared to gas-phase CH_2CHO the ΔE_{ads} of Enl/V_o is -3.26 eV. As mentioned below, the energy of Enl/V_o plus an atomic H adsorbed on an oxygen site at infinite separation is -2.01 eV relative to gas-phase AcH. Therefore Enl/V_o is the most stable of these four surface states for AcH, which is consistent with enolate appearing at higher temperatures than AcH and polymeric AcH in RAIRS [75].

Furthermore, in order to shed light on the high temperature decomposition mechanism that produces various C_2 species, three additional surface intermediates are proposed in this study to account for the formation of C_2H_4 and C_2H_2. They are various hydrogenated and dehydrogenated forms of AcH/V_o. The hydrogenation of AcH/V_o at the carbonyl C position produces a vacancy-stabilized ethoxy species (**Figure 3.1e**). The $d_{C\text{-}O}$ of Etx/V_o is 1.433 Å, and the $d_{C\text{-}C}$ is 1.524 Å, both of which are significantly longer than the corresponding bonds in AcH/V_o. Thus the C=O double bond character is completely lost upon the hydrogenation of AcH/V_o. The ΔE_{ads} of Etx/V_o is -3.95 eV relative to the gas-phase ethoxy radical. The dissociation of a methylene H from Enl/V_o produces CHCHO/V_o (**Figure 3.1f**). The $d_{C\text{-}O}$ and $d_{C\text{-}C}$ are 1.398 and 1.337 Å, respectively. These values are comparable to the C=C and C-O bonds in vinyl alcohol (1.332 and 1.374 Å) [75]. Relative to gas-phase C_2H_2O and C_2H_2, the ΔE_{ads} of this species is -3.75 eV and -0.24 eV, respectively. It also possesses no vibrational mode with a negative curvature. Carrasco et al. have previously reported a CHCHO/V_o state for C_2H_2 adsorption on $CeO_2(111)$, with a ΔE_{ads} of -0.12 eV [145]. The dissociation of a methyl H from Etx/V_o, or equivalently the hydrogenation of the original carbonyl C position in Enl/V_o, produces CH_2CH_2O/V_o (**Figure 3.1g**). The $d_{C\text{-}O}$ is 1.495 Å, much longer than a C=O double bond and even longer than a typical C-O single bond. The $d_{C\text{-}C}$ of this state is 1.487 Å, which falls between the lengths of a C-C single bond and a C=C double bond [75]. Its adsorption energy relative to gas-phase CH_2CH_2O is ΔE_{ads}=-3.98 eV and relative to gas-phase C_2H_4 is ΔE_{ads}=+0.70

Table 1 Calculated minimum adsorption energies (ΔE_{ads}, in eV), magnetic moment (in μ_B), and C-O and C-C bond lengths ($d_{C\text{-}O}$ and $d_{C\text{-}C}$, in Å), of the surface reaction intermediates on $CeO_2(111)$ and $CeO_{2-x}(111)$

Species	ΔE_{ads} [a]	Magnetic moment	$d_{C\text{-}O}$	$d_{C\text{-}C}$
AcH*	-0.25 [b] -0.43 [b, c]	0	1.228	1.492
AcH/V_o	-1.11 [b]	0 [d]	1.305	1.486
D/VV_o	-1.37 [b, e]	2 [d]	1.396 1.398 1.472 [f] 1.482 [f]	1.519 1.520
CHCHO/V_o	-3.75 [g] -0.24 [h]	0	1.398	1.337
Enl/V_o	-3.26 [g]	1 [d]	1.352	1.346
CH_2CH_2O/V_o	-3.98 [g] +0.70 [h]	0	1.495	1.487
Etx/V_o	-3.95 [g]	1	1.433	1.524
H*	-3.00 -0.73 [i]	1	-	-

[a] ΔE_{ads} is based on DFT total energy without ZPE corrections, at ¼ ML coverage; no co-adsorbed atomic hydrogen is included
[b] With respect to gas-phase AcH
[c] Calculated using optB86b van der Waals functional
[d] Singlet-triple/doublet-quadruplet splitting is 0.05 eV or less
[e] Averaged over 2 AcH
[f] Part of the polymeric C-O-C linkage
[g] With respect to gas-phase C_2H_xO
[h] With respect to gas-phase C_2H_x
[i] With respect to gas-phase H_2

eV. The latter indicates that the C_2H_4 moiety would be more stable without the C-O bond, although vibrational analysis finds no mode with a negative curvature, indicating that CH_2CH_2O/V_o is a local minimum on the potential energy surface. By comparison, CHCHO/V_o is more stable than CH_2CH_2O/V_o when viewed as the adsorbed states of the respective gas-phase C_2H_x molecules, which is consistent with C_2H_2 being a more reactive species than C_2H_4.

Incidentally, Enl/V_o (i.e. CH_2CHO/V_o), $CHCHO/V_o$, and CH_2CH_2O/V_o, which all have an unsaturated C end, can all form an alternate hemicyclic structure in which the unsaturated C atom forms a bond to an adjacent surface O atom. The hemicyclic forms of $CHCHO/V_o$ (i.e., $CHOCHO/VV_o$) and CH_2CH_2O/V_o (i.e., CH_2OCH_2O/VV_o) are 1.28 and 0.79 eV, respectively, more stable than the non-cyclic, monoxy states, although the formation of the second C-O bond have significant activation energies and is therefore not kinetically relevant in the microkinetic model presented below. On the other hand, the hemicyclic form of the enolate (i.e., CH_2OCHO/VV_o), as was initially suggested by Chen et al. [73], is 1.56 eV *less* stable than Enl/V_o. Finally, the adsorption energy of atomic hydrogen is calculated to be the lowest on top of a surface lattice O, at -3.00 eV with respect to atomic H and -0.73 eV with respect to H_2. The ΔE_{ads} of H would be lowered to -3.48 eV, or -1.20 eV with respect to gas-phase H_2, when a U value of 5 eV is used [71]. Previously Vicario et al. [146] reported the H adsorption energy to be -3.57 eV on the fully oxidized CeO_2(111) surface with respect to gas-phase atomic H (U= 4 eV). Popa et al. [147] reported -1.21 eV with respect to gas-phase H_2 (U= 4.5 eV). Similar values have also been reported by other authors [145, 148]. Therefore our results are in line with previously reported values for the ΔE_{ads} of H on CeO_2(111).

The elementary reaction steps that comprise the proposed TPD mechanism, along with the activation barrier, representative pre-factor, and reaction energy for each of the steps, are summarized in **Table 2**. These include the molecular desorption of AcH from a stoichiometric site (Step 1) and from an oxygen vacancy (Step 2); the coupling of AcH to form the dimer state

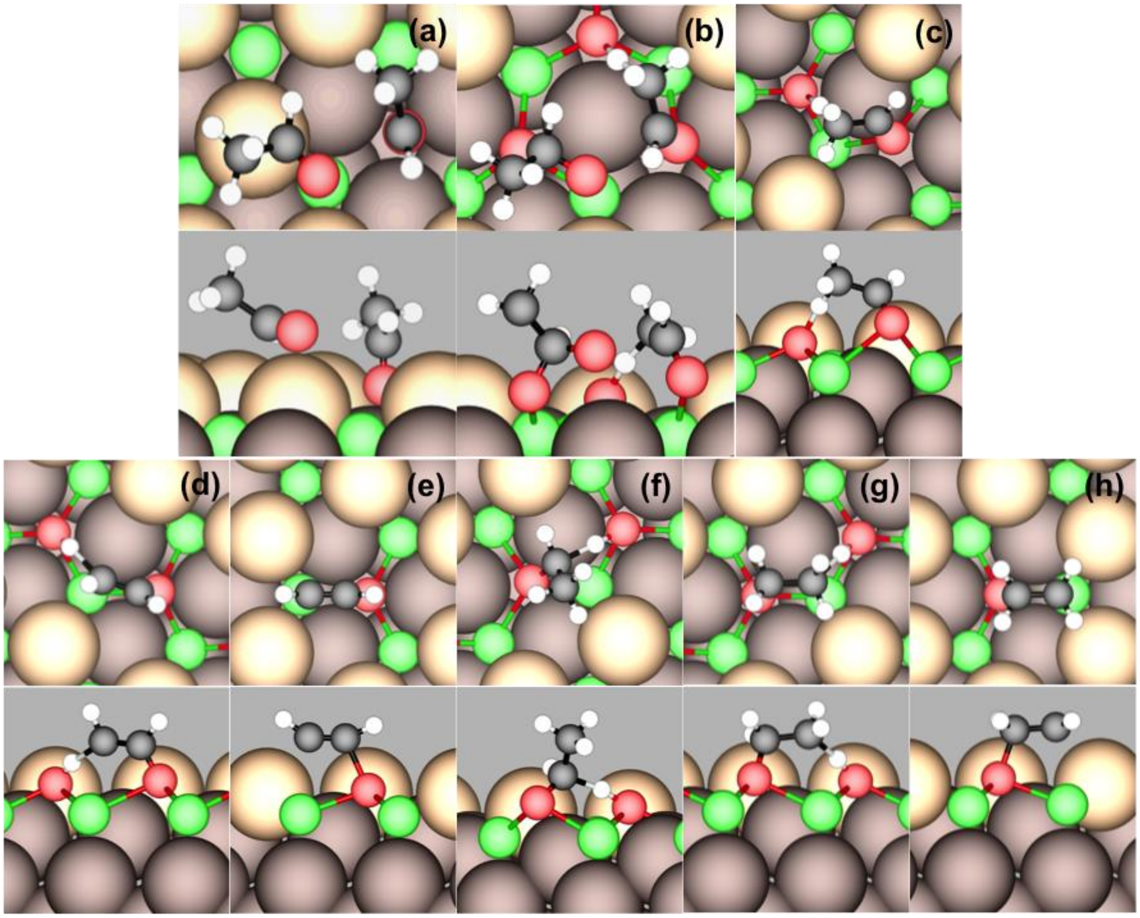

Figure 3.2 (Top) top view and (bottom) side view of DFT-calculated minimum-energy transition states for (a) AcH*, AcH/V_o coupling (Step 3 in Table 2); (b) D/VV$_o$ decomposition (Step 4); (c) AcH/V_o enolization (Step 5); (d) β C-H scission in Enl/V_o (Step 6); (e) C-O scission in CHCHO/V_o (Step 7); (f) Etx/V_o formation (Step 8); (g) β C-H scission in Etx/V_o (Step 9); (h) C-O scission in CH_2CH_2O/V_o (Step 10), on $CeO_{2-x}(111)$. Green, light brown, dark brown, red, black, and white spheres represent lattice Ce, surface lattice O, subsurface lattice O, O in molecules, C, and H atoms, respectively. Surface lattice O involved as Lewis base site is labeled the same as O in molecules to emphasize the bonding between atom/molecule and the surface.

and its decomposition (Steps 3, 4); the successive dehydrogenation of AcH/V_o to Enl/V_o and CHCHO/V_o (Steps 5, 6), and CHCHO/V_o decomposition to C_2H_2 (Step 7); AcH/V_o hydrogenation to Etx/V_o (Step 8), followed by dehydrogenation to CH_2CH_2O/V_o (Steps 9) and then decomposition to C_2H_4 (Step 10); finally, H desorption as H_2 (Step 11). No rate-limiting step is assumed.

For AcH molecular desorption from a stoichiometric site (Step 1), the GGA+U-PW91 desorption barrier is $-\Delta E_{ads} = 0.25$ eV. It is well known that GGA functionals systematically under-predict the adsorption energies of primarily physisorbed species while PW91 somewhat over-predict the strength of chemical bonds. Therefore we also used a self-consistent van der Waals functional, optB86b [146], to calculate the ΔE_{ads} of AcH* in the η^1 state, and obtained -0.43 eV. For Step 1 the desorption barrier is therefore taken to be $-\Delta E_{ads} = 0.43$ eV. Here for AcH*, "*" is a threefold hollow site above a second layer Ce cation, whereas the "*" site required by all of the others steps is a surface O site, which either accepts a dissociated H atom or bonds with a C center. Both involve a stoichiometric part of the surface, and it is inconsequential in this particular microkinetic model to distinguish them.

Two of the elementary steps have even smaller activation barriers than AcH* desorption barrier: C-O coupling (Step 3; see **Figure 3.2a** for snapshots of the transition state; the transitioning C-O bond has a length of $d_{C\text{-}O\ddagger} = 2.622$ Å) and enolization of AcH/V_o (Step 5; **Figure 3.2c**; $d_{C\text{-}H\ddagger} = 1.242$ Å, $d_{H\text{-}O\ddagger} = 1.524$ Å). This means that additional reactions can take place before molecular AcH desorbs on a $CeO_{2-x}(111)$ surface, which explains why some amount of the AcH molecules was retained on the surface up to high temperatures in the TPD experiment. The decomposition of the C-O coupled state occurs via the loss of a methyl H and simultaneously produces Enl/V_o and AcH* (Step 4; **Figure 3.2b**; $d_{C\text{-}O\ddagger} = 2.605$ Å, $d_{C\text{-}H\ddagger} = 1.348$ Å, $d_{H\text{-}O\ddagger} = 1.369$ Å). Given that AcH* is expected to rapidly desorb at temperatures where the decomposition occurs, this step is taken to release an AcH molecule to the gas phase directly.

Table 2. Proposed elementary reaction steps for AcH on $CeO_{2-x}(111)$ and their properties: activation barrier (E_a, in eV); reaction energy (E_{rxn}, in eV); and representative pre-factor (ν, in s^{-1}, at 298.15 K)

No.	Step	E_a	ΔE_{rxn}	ν
1	$AcH^* \rightarrow AcH\uparrow + *$	0.43	+0.43	10^{13}
2	$AcH/V_o \rightarrow AcH\uparrow + V_o$	1.11	+1.11	10^{13}
3	$AcH^* + AcH/V_o \leftrightarrow D/VV_o$	0.11	-1.57	4.11×10^{11}
4	$D/VV_o + * \rightarrow Enl/V_o + H^* + AcH\uparrow$	1.30	+0.73	2.12×10^{13}
5	$AcH/V_o + * \leftrightarrow Enl/V_o + H^*$	0.32	-0.91	3.72×10^{11}
6	$Enl/V_o + * \leftrightarrow CHCHO/V_o + H^*$	1.19	+1.19	1.30×10^{12}
7	$CHCHO/V_o + H^* \rightarrow C_2H_2\uparrow + H^* + *$	0.99	+0.43	2.45×10^{13}
8	$AcH/V_o + H^* \leftrightarrow Etx/V_o + *$	0.67	-0.73	1.77×10^{11}
9	$Etx/V_o + * \leftrightarrow CH_2CH_2O/V_o + H^*$	1.31	+1.30	1.55×10^{11}
10	$CH_2CH_2O/V_o + H^* \rightarrow C_2H_4\uparrow + H^* + *$	0.17	-0.64	1.40×10^{13}
11	$2H^* + V_o \rightarrow H_2\uparrow + V_o + 2^*$	1.75	+1.47	10^{13}

E_a and E_{rxn} are based on DFT total energy without ZPE correction. E_{rxn} for steps involving multiple reactants or products are calculated with the multiple species at infinite separation.

C_2H_2 desorption is proposed to involve $CHCHO/V_o$ as the intermediate, which is formed through *β* C-H bond scission in Enl/V_o (Step 6; **Figure 3.2d**; $d_{C\text{-}H\ddagger} = 1.736$ Å, $d_{H\text{-}O\ddagger} = 1.050$ Å), followed by C-O bond scission (Step 7; **Figure 3.2e**; $d_{C\text{-}O\ddagger} = 1.946$ Å). On the other hand, the reaction path to C_2H_4 formation is less clear. Mullins et al. suggested that it occurs via the direct hydrogenation of an enolate-like carbanion intermediate at the α C (i.e. the carbonyl C) position [149]. However, we could not locate such an elementary step for Enl/V_o, nor one for intra-molecular H shift for AcH/V_o, with an activation barrier lower than 2.5 eV. The formation of C_2H_4 via the decomposition of *ethoxy* was previously proposed by Christiansen et al. in a DFT study of ethanol conversion to ethylene on γ-$Al_2O_3(111)$, as involving concerted *β* C-H and C-O bond scission to yield ethylene directly without any C_2H_4 surface intermediate [150]. Beste et al. have recently studied ethanol decomposition on *stoichiometric* $CeO_2(111)$ theoretically and reported that the activation barriers for ethoxy decomposition to C_2H_4 exceed 2 eV for both the concerted and sequential mechanisms [151]. We find that interaction with an oxygen vacancy significantly facilitates the sequential decomposition of ethoxy to C_2H_4 on $CeO_{2-x}(111)$. The minimum energy reaction pathway to C_2H_4 desorption begins with the hydrogenation of AcH/V_o to Etx/V_o, (Step 8; **Figure 3.2f**; $d_{C\text{-}H‡}$ = 1.562 Å, $d_{H\text{-}O‡}$ = 1.234 Å), followed by β C-H bond scission to form CH_2CH_2O/V_o (Step 9; **Figure 3.2g**; $d_{C\text{-}H‡}$ = 1.627 Å, $d_{H\text{-}O‡}$ = 1.111 Å). C-O bond scission then releases C_2H_4 (Step 10; **Figure 3.2h**; $d_{C\text{-}O‡}$ = 1.761 Å). The reaction energy profile for the formation of C_2H_2 and C_2H_4 with respect to Enl/V_o, which is experimentally found to be the dominant surface species at high temperatures, is plotted in **Figure 3.4**. All of the C-H bond scission steps in this mechanism involve a surface lattice oxygen (a Lewis base) as the H acceptor. Incidentally, Etx/V_o and H* are calculated to be -2.3 eV with respect to gas-phase ethanol, which makes the recombinative desorption of ethoxy and atomic H as ethanol from $CeO_{2-x}(111)$ highly uncompetitive in vacuum. Indeed, no ethanol was detected in the TPD experiment [73].

Several previous surface science studies have reported molecular H_2 desorption on $CeO_{2-x}(111)$ surfaces near 600 K, whereas this desorption channel is not operative on the stoichiometric $CeO_2(111)$ surface [72, 75, 152]. Evidently some type of reduced ceria site is active for catalyzing the recombination of atomic H, but the nature of this active site remains elusive. Fernández-Torre et al. have reported in a DFT+U study that H_2 can in fact dissociate on stoichiometric $CeO_2(111)$ with a moderate activation barrier (E_a = 1.0 eV at U=4.5 eV), but their results indicate that the reverse barrier for atomic H recombination is in excess of 3 eV [153]. Similarly high barriers for atomic H recombination were reported by other groups [148, 154]. Wu et al. have recently studied H interaction with $CeO_{2-x}(111)$ surfaces and reported that the activation barrier for H recombination decreases with an increasing degree of surface reduction, but it remains more than 2 eV even on a large cluster of subsurface O vacancies (U=5 eV) [148], which would be inconsistent with H_2 desorption around 630 K. Moreover, the broad H_2 TPD peak shown in **Figure 1.8a** suggests that there may be a distribution of sites that catalyze H_2 formation and desorption. To ascertain the exact nature of the H_2 formation site is outside the scope of this study. Herein we postulate that the rate-limiting step in H recombinative desorption is the diffusion of atomic H across surface oxygen sites that is necessary for reaching the yet-to-be-determined active site for the H-H bond formation. The minimum diffusion barrier of atomic H on CeO_2(111) is reported by Fernández-Torre et al. to be 1.8 eV (U=4.5 eV). The diffusion mechanism involves the H atom hopping alternatingly between surface and subsurface O sites. We find the corresponding value for the H hopping barrier to be 1.75 eV at U=2 eV. This value, together with a typical diffusion prefactor of 10^{13}, is used for H_2 recombinative desorption (Step 11).

These DFT-calculated energetics with clear microscopic meaning were fed into our mean-field microkinetic model, which was able to generate a simulated TPD spectra and a corresponding surface coverage evolution of key surface species as a function of temperature, as shown in **Figure 3.3**. Above 200 K, two major AcH desorption waves are predicted: One spans from ~330 K to 420 K, with T_p = 391 K, and the other is broader from ~520 K to 670 K with T_p = 602 K, which matches the 620 K shoulder in the experimental TPD (**Figure 1.8a**). The 391 K wave originates from the decomposition of D/VV$_o$ (Step 4), whereas the 602 K wave originates from the recombination of Enl/V$_o$ and H* to form AcH/V$_o$ (reverse of Step 5), followed by AcH desorption from V$_o$ (Step 2). C_2H_4 desorbs from ~490 K to 670 K, with T_p = 592 K, whereas acetylene desorbs from ~570 K to 690 K, with T_p = 658 K. The H_2 desorption peak is fairly broad from 560 K to 770 K, with T_p at 620 K.

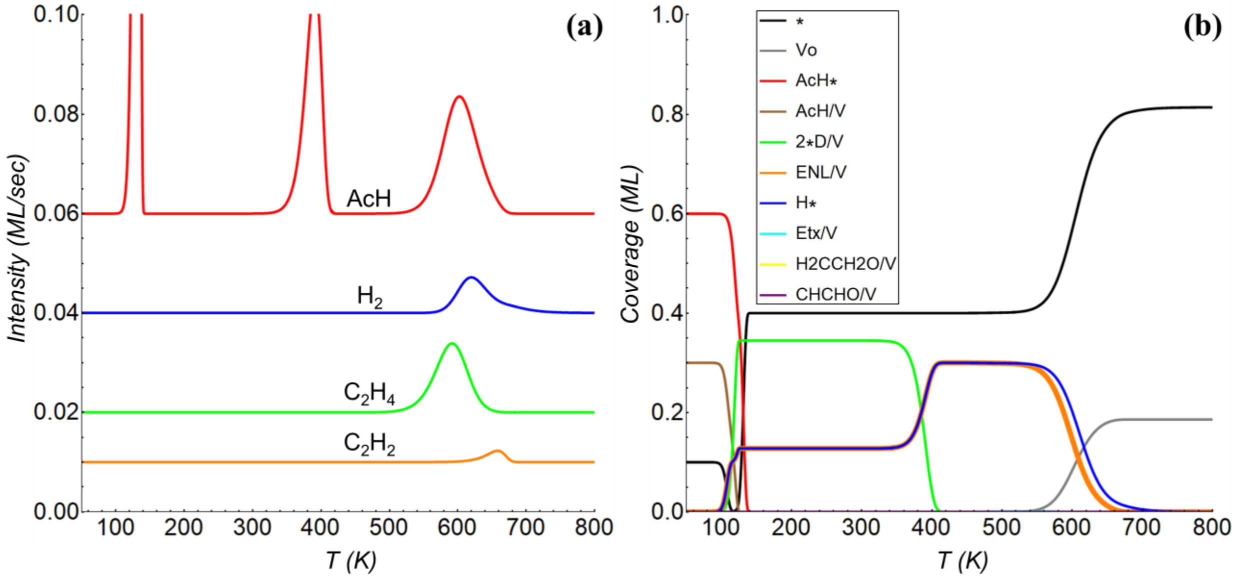

Figure 3.3. Simulated (a) TPD spectra and (b) surface coverage evolution of surface species, for acetaldehyde adsorption on $CeO_{2-x}(111)$ [77]. Initial coverages (in ML): AcH* = 0.6; AcH/V_o = 0.3; free site * = 0.1; all other adsorbates = 0; temperature = 50 K. Ramp rate = 2 K/s.

The microkinetic model also provides information on how the coverages of the surface intermediates evolve with temperature (**Figure 3.3b**). Most of the surface reactions, as signified by rapid changes in surface coverages, take place around three temperaturs: ~140, 400, and 600 K. The formation of the C-O coupled dimer occurs almost as soon as the temperature ramp starts and consumes all of the AcH/V_o states, which completely out-competes the enolization of AcH due to a lower kinetic barrier and poor availability of stoichiometric sites needed for dehydrogenation to occur. In the RAIRS experiment features associated with reduced sites, which remained upon heating above 220 K, were already present even below 220 K [75]. D/VV_o is predicted to be the dominant surface species up to ~380 K, following which Enl/V_o and H* are the dominant surface species all the way up to ~650 K, both of which are also consistent with the RAIRS study of Calaza et al. [75]. There is ~0.4 ML or more of empty site above ~120 K, so when H gains mobility (~520 K and above) there is space for different adsorbates to aggregate or separate according to their thermodynamic preference.

Neither Etx/V_o, CH_2CH_2O/V_o, nor CHCHO/V_o is predicted to have any appreciable coverage in the range of temperature simulated, and indeed none of these species is identified on the $CeO_{2-x}(111)$ surface in the previous RAIRS study [75]. Yet significantly, the product differentiation (C_2H_4 vs. C_2H_2) entirely depends on the formation of these minority species. Finally, the coverage of oxygen vacancies (V_o) increases from zero when Enl/V_o begins to desorb as AcH and releases oxygen vacancies at ~560 K. However, θ_{V_o} does not recover its initial value of 0.3 ML because the reductive desorption as C_2H_4 and C_2H_2 annihilates some amount of the vacancies. The final values of θ_* and θ_{V_o} are 0.81 and 0.19 ML, respectively. In conclusion, the key spectroscopic outcomes of our microkinetic model are in close agreement with the observed desorption activities for surface species, which supports the validity of the proposed mechanism on the well-defined ceria surface.

Clearly, oxygen vacancies (V_o) play a critical role in the reaction mechanism. They facilitate the enolization of AcH, and C-H bond scission/formation and C-O scission in AcH and its derivatives. Fundamentally, all these functions can be traced back to the fact that the acidic cations (Ce^{4+}) are buried beneath oxygen anions on the stoichiometric $CeO_2(111)$ surface. V_o open up access to Ce^{4+} and reveal the amphoteric nature of this surface, and allow the basic O atom in the carbonyl group of AcH to be stabilized. The C atom in the carbonyl group (the α C) would thereby be freed to form a bond with another atom, such as the β C, an external H atom, or a nucleophilic species such as the carbonyl O of another AcH molecule or the CH_2 group of an enolate because the *α* C is electrophilic, leading to C-O or C-C coupling. The activation of the *α* C and the availability of lattice oxygen as a Lewis base and H acceptor facilitate the enolization of AcH/V_o, and also *β* C-H scission in Etx/V_o and Enl/V_o. Finally, the conversion of the carbonyl bond from a double bond to a single bond facilitates the eventual deoxygenation of the molecule, ending in the re-oxidation of the vacancy.

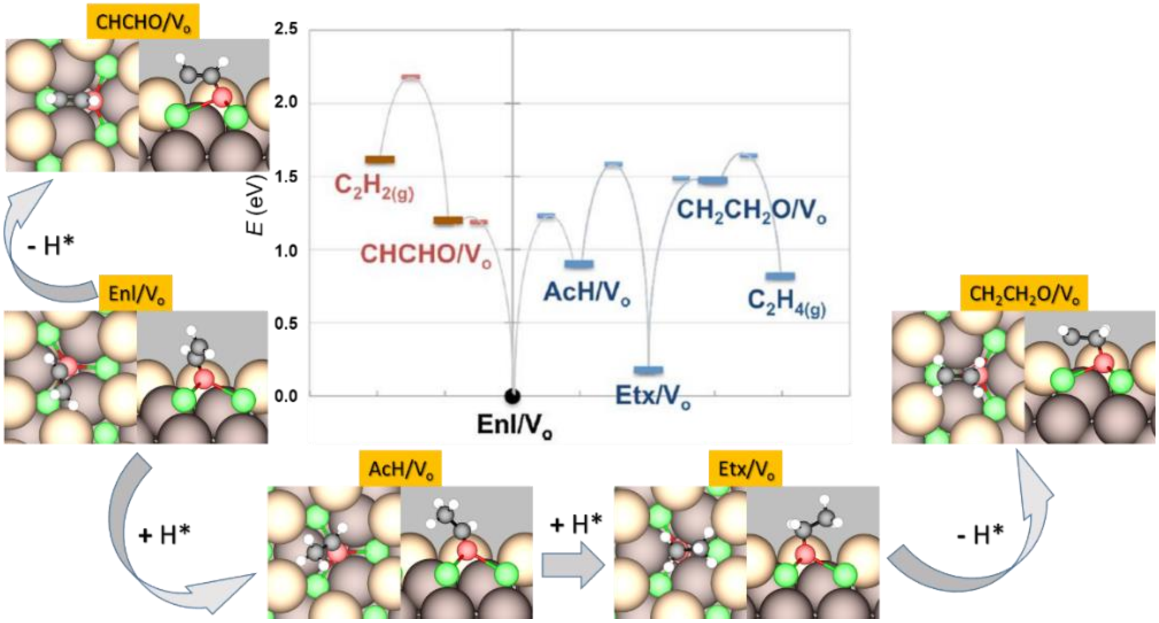

Figure 3.4. Schematic plot for hydrogen transfer processes and corresponding reaction energy profile in the high temperature regime for acetaldehyde adsorption on $CeO_{2-x}(111)$.

The occurrence of Etx/V_o indicates that intermolecular H transfer occurs between AcH and/or its derivatives on $CeO_{2-x}(111)$, as shown in **Figure 3.4**. Based on the proposed mechanism, the TPD of AcH adsorbed on $CeO_{2-x}(111)$ suggests that a window of temperature exists for transfer hydrogenation to occur on CeO_{2-x}, which is bound on the upper end by H_2 recombinative desorption (T_p = 620 K). Note that in AcH, *β* C-H scission occurs at a primary C. *β* C-H scission in a carbonyl compound where the *β* position is a secondary or tertiary C should require lower temperature for activation, thereby widening the temperature window for transfer hydrogenation, a potential route to biomass upgrading without needing molecular hydrogen [155], on this particular surface.

Till now, we were able to explain the formation of various C_2 species in the typical TPD experiment [73]. However, in contrast to the flow reactor experiments on ceria nano-shapes [78], C_4 species were not detected under UHV condition, even though enolate species (Enl/V_o) is identified to be the dominant surface species from ca. 400 K to 600 K, and its calculated vibrational signatures closely match RAIRS evidence in the same temperature range [75]. Enolates are well known to be the key intermediates in aldol condensation reactions, so we have devised additional experiments to attempt to realize the formation of CrA in UHV experiments. In order to take advantages of the wide temperature window of enolate on the surface, a custom "double-ramp" procedure was used. The idea behind it was to stop the experiment with the enolate on the surface and then cool down to add more AcH to allow them to react. The procedure involved a program of cooling-dosing-ramping, breaking and stopping the ramp, then cooling-dosing-ramping again. The steps performed are as follows: 1) The surface was cooled below the monolayer adsorption temperature of AcH (160-175K) and dosed with AcH; 2) the surface temperature was ramped at 2 K/s (first ramp); 3) at a set break temperature, T_B, the heating ramp was stopped (there was no intentional dwell time at T_B, and the direction of change of the temperature reversed toward cooling on the order of seconds once the heating was stopped); 4) the surface was once again cooled below the monolayer adsorption temperature for AcH and dosed with AcH; and finally 5) the surface temperature was ramped at 2 K/s up to 900 K (second ramp).

In this section four experimental TPD profiles will be presented (**Figure 3.5**). In all cases, the vertical axis indicates molecular gas phase concentration detected by mass spectrometry during TPD. **Figure 3.5a** presents the TPD profile for AcH from oxidized $CeO_2(111)$ surface, which has a low concentration of vacancies. Consistent with previous results [73, 75], mostly only molecular desorption of un-reacted AcH is observed at slightly above 200 K. **Figure 3.5b** shows the TPD profile for AcH on a partially reduced surface (~60% Ce^{3+}).

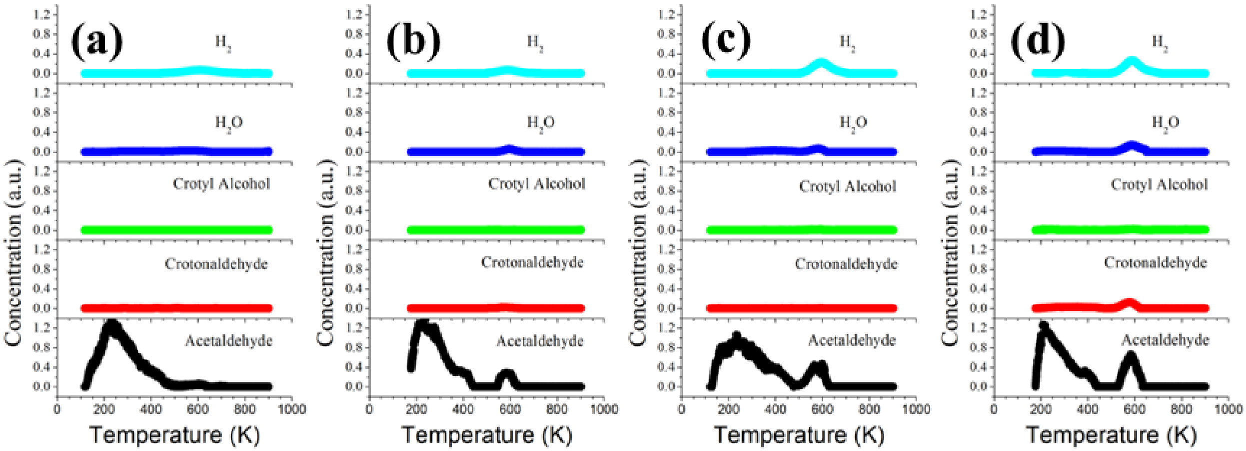

Figure 3.5. Gas phase concentrations of molecules detected during typical TPD of AcH adsorbed on (a) oxidized $CeO_2(111)$ with few vacancies; (b) partially reduced $CeO_{2-x}(111)$ with ~60% Ce^{3+}. TPD of AcH on $CeO_{2-x}(111)$ with ~60% Ce^{3+} for the second temperature ramp during the double-ramp procedure described in the text where the first temperature ramp was stopped at either (c) 410 K or (d) 530 K.

Here we again see results consistent with prior studies that there are now three AcH desorption waves [73, 75, 77]. Signals associated with ethylene and acetylene were observed as minor products at temperatures similar to those reported in our previous study [73]. **Figure 3.5c** and **3.5d** show the TPD results from the second ramp with the T_B = 410 K and T_B = 530 K, respectively. T_B = 530 K produced a clearly distinguishable CrA peak (on the order of 5% of the carbon balance), while T_B = 410 K did not. In all experiments, there was little to no crotyl alcohol detected, which was consistent with the fact that crotyl alcohol was a very minor product on ceria octahedra under flow reaction conditions [78]. Enhanced H_2O production (**Figure 3.5d**) is consistent with aldol condensation, which ejects two H atoms for each CrA molecule formed from AcH, although the oxygen in the water may or may not originate directly from the organic intermediates. The quantity of vacancies at the end of an experiment was found to be similar to at the beginning of experiment based on XPS.

Building on the previously elucidated mechanism (**Table 2**) for the TPD of AcH on partially reduced $CeO_{2-x}(111)$ [77], we propose to extend this mechanism to include additional pathways to give three different CrA formation mechanisms that we denote as Mechanisms A, B, and C: A) coupling between Enl/V_o and AcH/V_o ; B) coupling between two Enl/V_o; C) coupling between a surface adsorbed AcH and Enl/V_o. They are all based on the hypothesis that Enl/V_o is the key reactive intermediate and must exist on the surface in order for C-C coupling to occur, while they differ in the reactant that couples to Enl/V_o. Each mechanism is restricted to a different C-C coupling pathway. By doing so we aim to identify the main pathway of the aldol addition reaction as observed in our double-ramp experiments. The schematics in **Figure 3.6** illustrate the three proposed TPD mechanisms.

The extended additional steps are listed in **Table 3** with their DFT-calculated energetic parameters. Below, each mechanism is presented with a reaction energy profile and the structures of the key reaction intermediates and transition states. The microkinetic modeling results for each mechanism, including simulated desorption spectra and coverage evolution of surface species are presented in the next subsection.

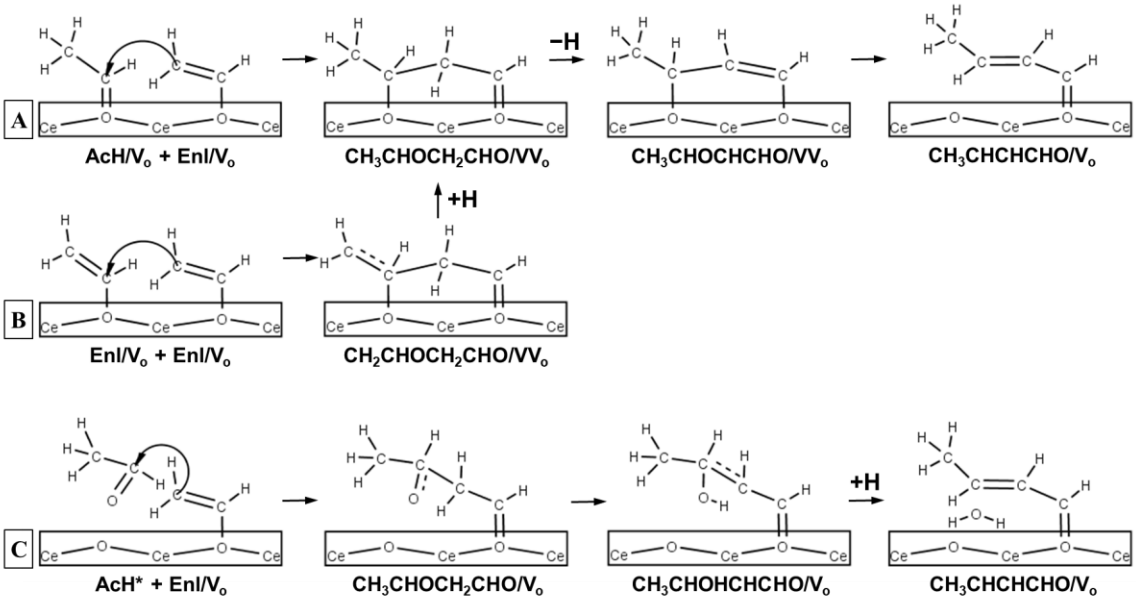

Figure 3.6. Schematics for expanded TPD mechanisms A, B and C. To be noted, upon H addition step in mechanism B, the following steps are the same as those in mechanism A.

In Mechanism A (**Figure 3.7**), C-C coupling occurs between AcH/V$_o$ and Enl/V$_o$ (**Figure 3.7a** and **e**) to produce CH_3CHOCH_2CHO (**Figure 3.7b**), which occupies a pair of adjacent surface oxygen vacancies (VV$_o$) and a surface H, with a small E_a of 0.25 eV. The methylene group (-CH_2-) undergoes H abstraction (**Figure 3.7f**) with a nearby lattice oxygen as the H acceptor, with E_a = 0.65 eV. The product, $CH_3CHOCHCHO$/VV$_o$ (**Figure 3.7c**), undergoes C-O scission (E_a = 0.88 eV) that cleaves off the internal oxygen, which yields a vacancy-stabilized CrA (CrA/V$_o$, **Figure 3.7d**) and annihilates one oxygen vacancy. The final step is desorption of CrA from V$_o$, which is common to all three expanded TPD mechanisms. The desorption barrier is taken to be the reverse of the adsorption energy, which is calculated to be -1.35 eV (GGA-PW91) and -2.12 eV (optB86-vdW). The negative of the latter is used in the microkinetic modeling as the desorption barrier for CrA because it yields far better agreement with the experimental peak temperature for CrA than the GGA value. However, optB86b-vdW is known

Table 3. Extended steps in mechanisms A, B, and C for AcH TPD on $\mathrm{CeO_{2\text{-}\mathit{x}}}$(111) with DFT-calculated activation energy (E_a, in eV), reaction Energy (ΔE_{rxn}, in eV), and representative pre-factor (ν, in s^{-1}, at 298.15 K)[#] for each proposed elementary step

Mech	No.	Step	E_a	ΔE_{rxn}	ν
A	12	$\mathrm{Enl/V_o{+}AcH/V_o \leftrightarrow CH_3CHOCH_2CHO/VV_o}$	0.25	-0.53	1.47×10^{11}
	13	$\mathrm{CH_3CHOCH_2CHO/VV_o{+}{*}{\leftrightarrow}CH_3CHOCHCHO/VV_o + H{*}}$	0.65	-0.75	3.58×10^{12}
	14	$\mathrm{CH_3CHOCHCHO/VV_o \leftrightarrow CrA/V_o{+}{*}}$	0.88	+0.38	2.69×10^{13}
B	12	$\mathrm{Enl/V_o{+}Enl/V_o \leftrightarrow CH_2CHOCH_2CHO/VV_o}$	1.87	+1.80	2.92×10^{11}
	13	$\mathrm{CH_2CHOCH_2CHO/VV_o{+}H{*}{\leftrightarrow}CH_3CHOCH_2CHO/VV_o{+}{*}}$	0.00	-1.41	6.21×10^{12}
	14-15	same as A13-A14			
C	12	$\mathrm{Enl/V_o{+}AcH{*} \leftrightarrow CH_3CHOCH_2CHO/V_o}$	0.22	+0.13	8.07×10^{9}
	13	$\mathrm{CH_3CHOCH_2CHO/V_o \leftrightarrow CH_3CHOHCHCHO/V_o}$	1.03	-0.56	7.08×10^{11}
	14	$\mathrm{CH_3CHOHCHCHO/V_o \leftrightarrow CrA/V_o{+}OH{*}}$	1.20	+1.10	1.33×10^{14}
	15	$\mathrm{CrA/V_o{+}OH{*}{+}H{*} \leftrightarrow CrA/V_o{+}H_2O{*}}$	0.10	-0.07	1.05×10^{12}
	16	$\mathrm{H_2O{*} \rightarrow H_2O\uparrow}$	0.52	+0.52	10^{13}
Des.		$\mathrm{CrA/V_o \rightarrow CrA\uparrow{+}V_o}$	2.12	+2.12	10^{13}

E_a and ΔE_{rxn} reported are based on DFT total energies without ZPE corrections. CrA desorption is common to all three mechanisms as the final step.

[#] Calculated in the harmonic approximation, except for desorption steps where a value of 10^{13} is used.

to over-bind molecules somewhat in many cases and there is so far no database of experimentally measured heats of chemisorption on oxides to gauge how accurate this functional is for adsorption on ceria. The strong interaction of the carbonyl intermediates with V_o on CeO_2(111) is a reason why alcohol species such as crotyl alcohol and ethanol do not appear as major products in the current and prior experiments [78], since the hydrogenation of the vacancy-stabilized C=O group is likely a difficult step.

In Mechanism B (**Figure 3.8**), a pair of adjacent vacancy-stabilized enolate molecules (Enl/V_o) undergo self-coupling by overcoming a substantial E_a of 1.87 eV, forming CH_2CHOCH_2CHO/VV_o (**Figure 3.8b**). Afterwards a surface H atom is transferred with practically zero barrier from a lattice O site to the terminal methylene group of CH_2CHOCH_2CHO/VV_o, forming CH_3CHOCH_2CHO/VV_o (**Figure 3.8c**). The subsequent steps are identical to Mechanism A following the formation of CH_3CHOCH_2CHO/VV_o, although the prior steps in Mechanism A, i.e. C-C coupling between Enl/V_o and AcH/V_o, are not included here.

In Mechanism C (**Figure 3.9**), the C-C coupling step occurs between surface-adsorbed AcH* and vacancy-stabilized Enl/V_o. Thus this mechanism requires only one surface oxygen vacancy rather than a vacancy dimer as in Mechanisms A and B. As shown in **Table 3**, the C-C coupling step only needs to overcome an activation energy of 0.22 eV, with a corresponding ΔE_{rxn} of +0.13 eV. The product of the C-C coupling step, CH_3CHOCH_2CHO/V_o (**Figure 3.9b**), is less stable than the C-O coupled dimer and prone to decomposition. The most facile pathway to CrA formation involves intra-molecular H transfer (from the methylene group to the internal carbonyl O) with E_a = 1.03 eV to yield a vinyl alcohol species, $CH_3CHOHCHCHO/V_o$ (**Figure 3.9c**), and the OH group then dissociating with E_a = 1.20 eV. OH can scavenge a nearby surface H to form water, which readily desorbs from the surface (ΔE_{ads} = -0.52 eV).

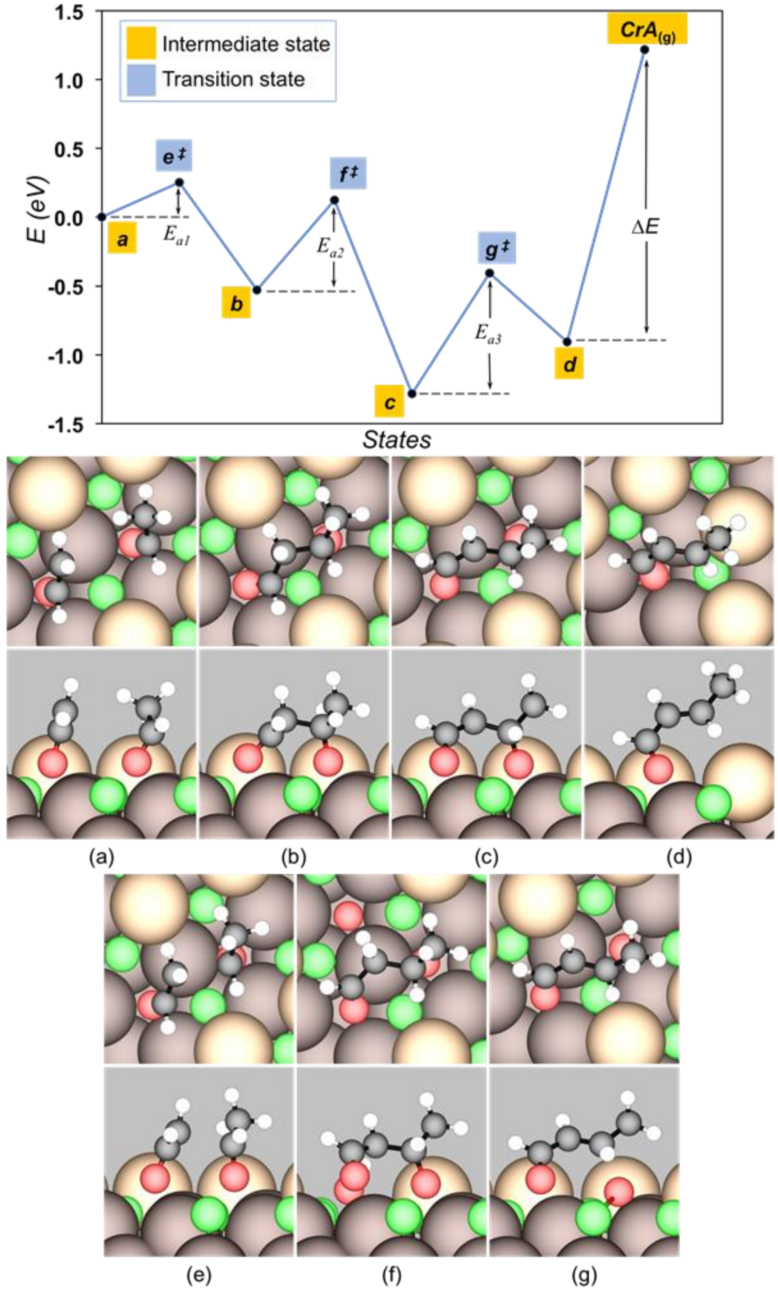

Figure 3.7. Extended steps of TPD Mechanism A. (Upper) DFT-calculated reaction total energy profile. The labeled states are: (a) Enl/V$_o$+AcH/V$_o$; (b) CH_3CHOCH_2CHO/VV$_o$; (c) $CH_3CHOCHCHO$/VV$_o$; (d) CrA/V$_o$; (e‡) TS for C-C coupling; (f‡) TS for H abstraction; (g‡) TS for C-O scission. The forward E_a's are E_{a1} = 0.25 eV, E_{a2} = 0.65 eV, E_{a3} = 0.88 eV, and ΔE = 2.12 eV. (Lower) Snapshots of reaction intermediates and transition states, with top view on top and side view on bottom. Labels correspond to those in the upper panel. Green, light brown, dark brown, red, black, and white spheres represent lattice Ce, surface lattice O, subsurface lattice O, O in molecules, C, and H atoms, respectively. Surface lattice O atoms bonded to C or H atoms in the molecules are considered part of the molecules. Periodic images of the adsorbates have been removed for clarity.

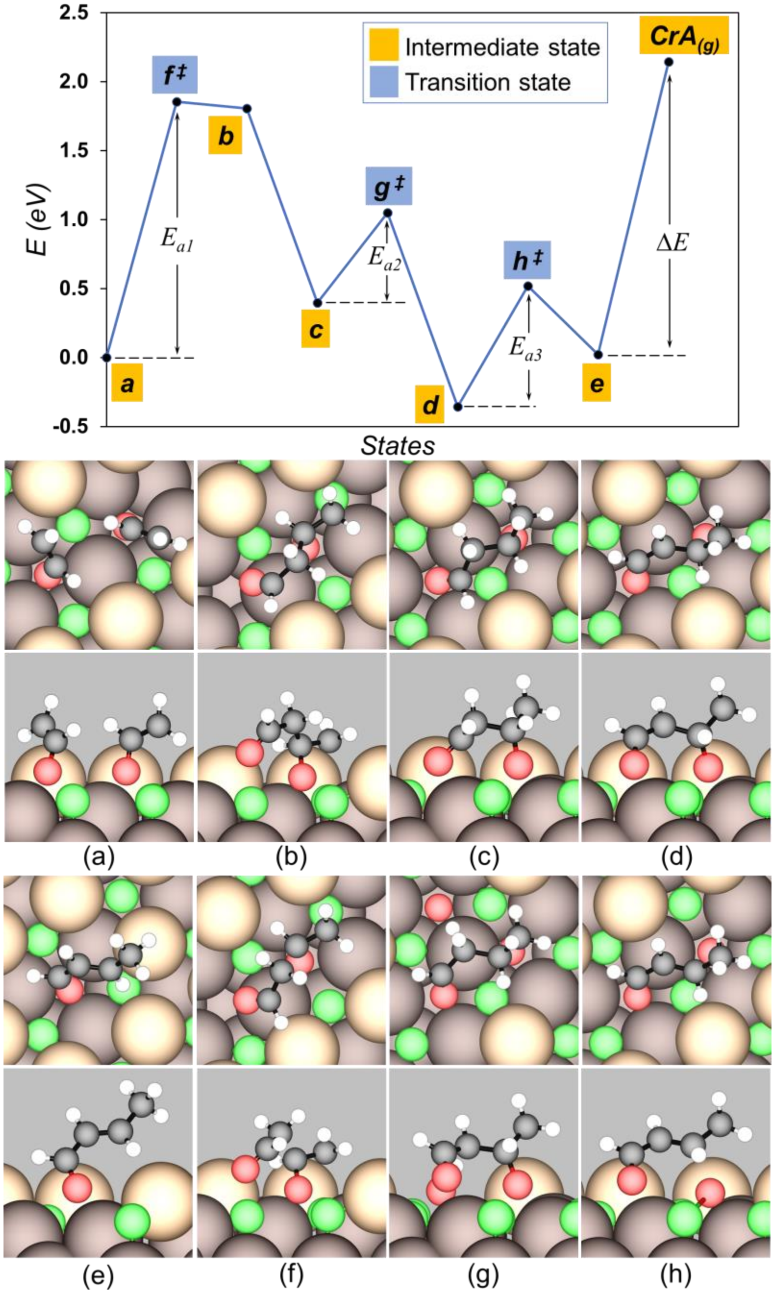

Figure 3.8. Extended steps of TPD Mechanism B. (Upper) DFT-calculated reaction total energy profile. The labeled states are: (a) Enl/V_o+Enl/V_o; (b) CH_2CHOCH_2CHO/VV_o; (c) CH_3CHOCH_2CHO/VV_o; (d) $CH_3CHOCHCHO$/VV_o; (e) CrA/V_o; ($f^‡$) TS for C-C coupling; ($g^‡$) TS for H abstraction; ($h^‡$) TS for C-O scission. The forward E_a's are E_{a1} = 1.87 eV, E_{a2} = 0.65 eV, E_{a3} = 0.88 eV, and ΔE = 2.12 eV. (Lower) Snapshots of reaction intermediates and transition states, with top view on top and side view on bottom. Labels correspond to those in the upper panel. Green, light brown, dark brown, red, black, and white spheres represent lattice Ce, surface lattice O, subsurface lattice O, O in molecules, C, and H atoms, respectively. Surface lattice O atoms bonded to C or H atoms in the molecules are considered part of the molecules. Periodic images of the adsorbates have been removed for clarity.

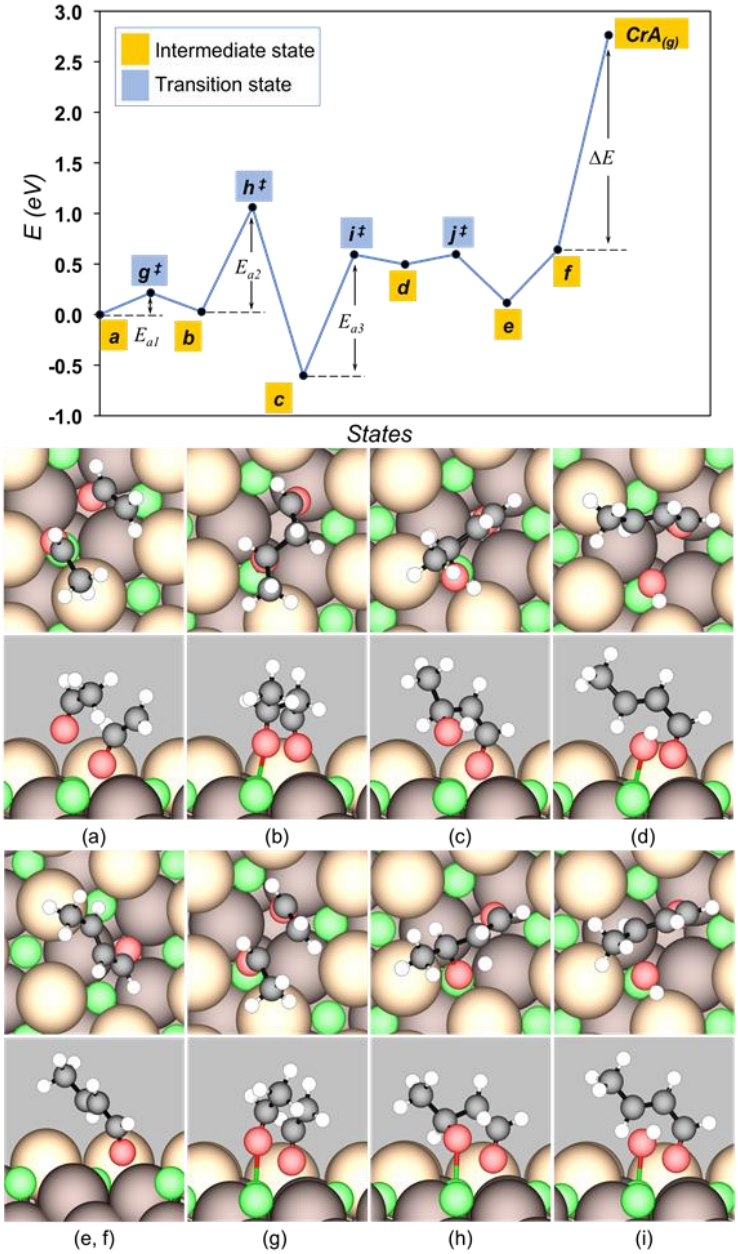

Figure 3.9. Extended steps of TPD Mechanism C. (Upper) DFT-calculated reaction total energy profile. The labeled states are: (a) Enl/V_o+AcH*; (b) CH_3CHOCH_2CHO/V_o; (c) $CH_3CHOHCHCHO/V_o$; (d) CrA/V_o+OH*; (e) CrA/V_o, H_2O*; (f) CrA/V_o, H_2O^{gas}; ($g^‡$) TS for C-C coupling; ($h^‡$) TS for intra-molecular H transfer; ($i^‡$) TS for OH detaching; ($j^‡$) TS for water formation. The forward E_a's are E_{a1} = 0.22 eV, E_{a2} = 1.03 eV, E_{a3} = 1.20 eV, and ΔE = 2.12 eV. (Lower) Snapshots of reaction intermediates and transition states, with top view on top and side view on bottom. Labels correspond to those in the upper panel. Green, light brown, dark brown, red, black, and white spheres represent lattice Ce, surface lattice O, subsurface lattice O, O in molecules, C, and H atoms, respectively. Surface lattice O atoms bonded to C or H atoms in the molecules are considered part of the molecules. Periodic images of the adsorbates have been removed for clarity.

Our microkinetic modeling effort based on the three TPR mechanisms is aimed at reproducing and explaining the results observed in the second ramp of the double-ramp experiments. The coverages at the start of the second ramp are specified in the caption of **Figure 3.10**. They are the final results of the microkinetic model of our original TPD mechanism by terminating the temperature ramp at 602 K, i.e., prior to the peak of the 3rd AcH desorption wave in the original microkinetic model, so that a certain portion of the occupied V_o becomes unoccupied and available to be occupied by AcH in the second dosing. Therefore, a mixture of the enolate and AcH occupy all of the V_o sites at the beginning of the simulated second ramp. The total coverage of V_o (0.226 ML) is less than the initial coverage of V_o used in the original microkinetic model (0.3 ML) because a portion of V_o has been annihilated in the reductive desorption of the C_2 products. Residual atomic H and newly dosed molecular AcH take up most of the oxidized sites. The starting temperature and ramping rate are identical to those used in the original model [77].

The simulated TPD spectra based on Mechanism A are shown in **Figure 3.10a**. Three AcH desorption peaks are predicted, with peak temperatures (T_p) of 132, 391, and 656 K. As mentioned before, the origin for the 1st AcH wave is the molecular desorption of AcH. The 2nd AcH wave is due to the decomposition of a C-O coupled dimer (D/VV_o), which releases an AcH molecule to the gas phase under UHV conditions. The 3rd AcH wave is due to the recombinative desorption of Enl/V_o and H. Compared to the our original TPD mechanism [77], the 3rd AcH peak temperature here is higher by ~50 K, which also applies to molecular hydrogen with T_p = 660 K (previously 620 K). The desorption wave for CrA is predicted to span from ca. 590 K to 720 K, with T_p = 686 K.

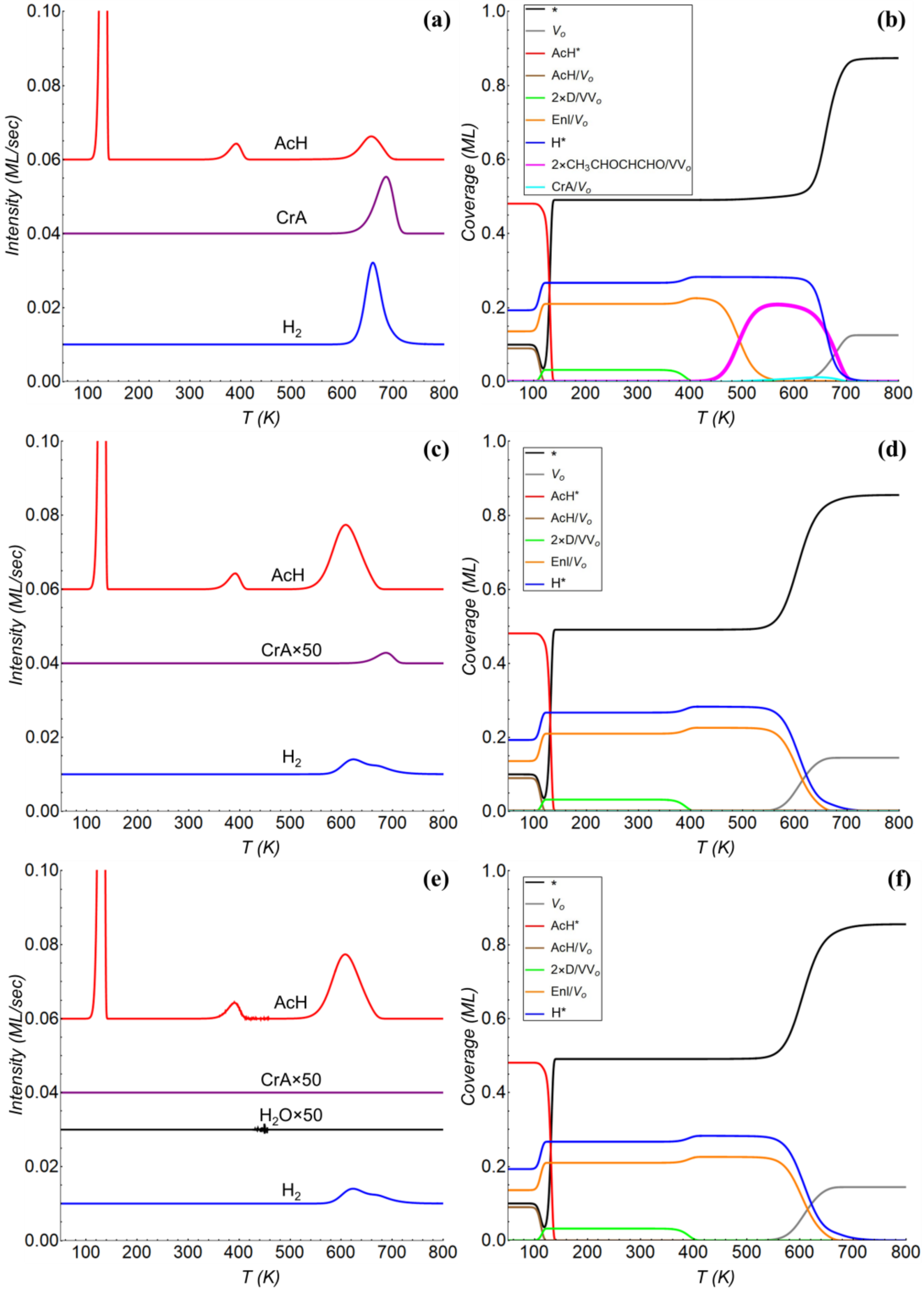

Figure 3.10. (a), (c), (e) Simulated TPD spectra and corresponding (b), (d), (f) coverages of surface intermediates as a function of temperature for AcH adsorbed on partially reduced CeO$_{2-x}$(111) based on microkinetic modeling of TPD Mechanism A, B, and C, respectively. Initial coverages (in ML): Enl/V$_o$ = 0.136; AcH/V$_o$ = 0.090; H* = 0.193; AcH* = 0.481; all other intermediates = 0; free V$_o$ = 0 ML; free site * = 0.1; T_0 = 50 K; ramp rate = 2 K/s. Surface intermediates with essentially 0 ML coverages are not shown in (b), (d) and (f) [156].

Microkinetic modeling also predicts how the coverages of surface species evolve as a function of temperature. For Mechanism A (**Figure 3.10b**), it can be seen that all the additional AcH added for the second temperature ramp has disappeared by ca. 130 K, due to either molecular desorption or enolization (with a concomitant increase in the coverage of $\mathrm{Enl/V_o}$). Between ca. 130 K and 500 K the enolate is the dominant C-containing surface species. Above ca. 450 K, the C-C coupling pathway is actuated to generate $\mathrm{CH_3CHOCHCHO/VV_o}$, which becomes a dominant surface species between ca. 500 K and 700 K. This happens because the enolate begins to recombine with H to form $\mathrm{AcH/V_o}$, which then rapidly undergoes C-C coupling with other $\mathrm{Enl/V_o}$ but does not build up any appreciable coverage. A small coverage of $\mathrm{CrA/V_o}$ also builds up between ca. 550 K and 700 K. All other organic intermediates are predicted to have negligible coverages. At the end of the temperature ramp ca. 0.1 ML of oxygen vacancy (out of the initial 0.226 ML) is annihilated on account mainly of CrA formation.

The results of microkinetic modeling for Mechanism B are markedly different from those of Mechanism A. As shown in **Figure 3.10c**, the 3rd AcH wave has a T_p = 608 K and a greater peak area than the 2nd AcH peak. CrA desorption occurs with a nearly identical T_p to Mechanism A, but it is significantly diminished in intensity. These results are similar to the microkinetic modeling results of our original AcH TPD mechanism [77] because the C-C coupling pathway is essentially not operative in Mechanism B due to the high activation energy for the enolate self-coupling step. This is confirmed by the evolution of the coverages of surface species, which indicates that none of the C_4 intermediates have any appreciable coverage over the entire temperature range in Mechanism B (and therefore not shown in **Figure 3.10d**). Combining Mechanisms A and B yields results essentially identical to Mechanism A alone.

No CrA desorption is predicted in the simulated TPD based on Mechanism C (**Figure 3.10e**). The reason why Mechanism C fails to produce CrA is that the C-C coupling product, CH_3CHOCH_2CHO/V_o, readily breaks down and back into Enl/V_o and AcH. The other desorption features are mostly identical to those based on Mechanism B.

Overall, therefore, Mechanism A yields the best agreement with the double-ramp experiments on $CeO_{2-x}(111)$ with $T_B = 530$ K. The essential features of this mechanism are: 1) The C-C coupling step occurs in a pair of surface oxygen vacancies. The site requirement is further discussed below. 2) CrA desorption, and not C-C coupling, is rate-limiting. We have estimated that, if CrA desorption were not rate-limiting, the T_p of CrA desorption would be 493 K.

Note that ethylene and acetylene channels remain part of the expanded mechanisms, although their production, together with high-temperature AcH formation, is reduced compared to the original TPD model [77]. This is consistent with the outcome of the double-ramp experiments, which found ethylene and acetylene to be minor products (especially the latter). We attribute the difference to the existence of the CrA channel, which removes a portion of the enolates from the uni-molecular pathways that produce AcH, ethylene, and acetylene. Of these, only the desorption of the organics as C_2H_2 permits H to desorb as H_2, so the diminishment of acetylene formation means less contribution to H_2 evolution from the uni-molecular pathways. On the other hand, the formation of each CrA molecule from two AcH molecules discharges a net total of two H atoms, so an H_2 peak similar in size to the CrA peak should be expected and is indeed predicted by our microkinetic model for Mechanism A. Since no H_2O channel is provided for in Mechanism A whereas on the actual ceria surface some of the atomic H is almost certainly diverted from desorption as H_2 to reduction of the surface (e.g. at loosely bound lattice

O sites), the predicted H_2 desorption wave would be more intense in relation to CrA desorption than observed in the experiment.

We attribute the face that no CrA was detected in the single-ramp experiments [75] to the fact that, as alluded to before, the positioning of oxygen vacancies is crucial to the bimolecular coupling step. A key requirement implicit in Mechanisms A and B (but not C) is that Enl/V_o and AcH/V_o or another Enl/V_o must be adjacent to each other in order for aldol addition and CrA formation to occur effectively. If Enl/V_o is instead surrounded by oxygen sites, C-C coupling can still occur (e.g. via Mechanism C), but it would not lead to CrA formation under UHV conditions due to the decomposition of intermediates.

The nature of oxygen vacancies on CeO_2(111) has long been debated in the literature. Early work based on scanning tunneling microscopy (STM) and atomic force microscopy (AFM) for high-temperature annealed CeO_2(111) single crystal surfaces reported a predominance of surface and subsurface oxygen vacancy clusters, while point surface vacancies appeared to be a minority species [129, 157]. More recently it was demonstrated theoretically that previous STM studies were not capable of distinguishing oxygen vacancies from fluorine impurities, which are typically present at appreciable concentrations in naturally occurring CeO_2, and that the vacancy clusters seen in STM may be clusters of fluorine atoms [130]. DFT studies based on GGA [158, 159], GGA+U (U=4.5~5 eV) [160-162], and HSE06 hybrid functional [160] all reported that an isolated oxygen vacancy to be a few tenths of an eV more stable in subsurface than in surface. GGA+U also predicted point vacancies to be more stable than vacancy clusters, whether on surface or in subsurface [161, 163]. Forming a surface vacancy dimer from two surface point vacancies is calculated to be endothermic by ~0.3 eV [161, 163].

Based on the latest findings, we surmise that the as-synthesized $CeO_{2-x}(111)$ films used in our experiments initially (**Figure 3.5b**) contained primarily isolated vacancies and few vacancy clusters since they are disfavored by thermodynamics. When AcH was dosed onto such a surface, all point vacancies should be occupied by AcH and later the enolate molecules, which immobilized the vacancies. Mechanisms A and B would be largely inoperative on such a $CeO_{2-x}(111)$ surface. For clusters of oxygen vacancies to appear, the following conditions must be met: 1) some AcH molecules desorb to vacate some vacancies; 2) vacancies are able to diffuse at an appreciable rate; 3) the energetics is altered to favor the aggregation of vacancies.

What the double-ramping experiments with T_B = 530 K (602 K in our microkinetic modeling) accomplish (**Figure 3.5d**), thus, is to free some vacancies while retaining some enolate molecules in vacancies since the 3rd AcH desorption wave is well under way by 530 K. When unoccupied vacancies appear at 530 K, their mobility is expected to be high because the diffusion barrier for oxygen vacancies via a surface-subsurface exchange mechanism has been calculated theoretically to be modest (E_a = 0.5 or 0.6 eV with GGA+U with U=3 [164] or 5 [165] respectively). Further, our calculations show that the occupation of a surface V_o by an enolate can make the formation of a vacancy dimer exothermic, in contrast to the dimerization of two unoccupied surface point vacancies [161, 163]. As summarized in **Table 4**, when an enolate occupies a surface V_o, the energetics of a second, unoccupied V_o varies depending on its location, with the site in the surface that is nearest neighbor to Enl/V_o being the most favorable. In other words, neighbor-neighbor interaction between Enl/V_o and an unoccupied V_o (similar to adsorbate-adsorbate effects if V_o were considered an adsorbate) alters which state is thermodynamically favored relative to the energetics in the absence of the enolate. Conversely, if most of the enolates desorb, the thermodynamics would revert and cause most such vacancy dimers to re-disperse. We note this stabilization does not extend to the formation of a vacancy trimer: The energy of adding a third, unoccupied surface V_o to an existing Enl/VV_o (enolate-stabilized vacancy dimer) is calculated to be +0.55 and +0.37 eV (U=2 and 5, respectively).

Table 4. Location, Energy (E_v, in eV), and Boltzmann Probability (P, in %, calculated at 603 K) for an Unoccupied Oxygen Vacancy in the Presence of an Enl/V_o species on $CeO_2(111)$ at U = 2 and 5 eV

	U = 2		U = 5	
location of 2nd V_o [a]	E_v [b]	P	E_v [b]	P
N.N., surface	-0.03	60	-0.13	91
N.N., subsurface	+0.27	0	+0.27	0
Inf. Sep., surface	+0.05	9	+0.01	4
Inf. Sep., subsurface	0	31	0	5

[a] Relative to the location of the V_o occupied by the enolate, with a coadsorbed H at a nearby atop O_{surf} site. N.N. = nearest neighbor, Inf. Sep. = infinite separation.

[b] Based on DFT total energy without ZPE correction, relative to the Inf. Sep., subsurface state.

In short, all three conditions above can be met if the initial temperature ramp is terminated at an appropriate temperature, resulting in the formation of partially occupied surface vacancy dimers that allow the enolate molecules to be stabilized side-by-side in vacancies, in a position to undergo effective adol addition in the second temperature ramp. Using a lower T_B (e.g. 410 K) in the initial temperature ramp could not lead to CrA formation (**Figure 3.5c**) because all vacancies are still occupied by the enolates and cannot aggregate to form vacancy dimers.

Adsorbate-adsorbate interaction is an aspect of surface chemical kinetics that microkinetic modeling is not capable of fully handling. As the theoretical results above show, there are comparable coverages of some organic intermediate and atomic H (ca. 0.2~0.3 ML) between ca. 100 K and 600~700 K (**Figure 3.10**, depending on the mechanism). The interaction between the organic intermediates and atomic H turns out to be moderately repulsive in all cases (**Table 5**). On the basis of that, and for consistency with our previous microkinetic model [77], we have treated the organic intermediates and H to have no interaction, or "at infinite

Table 5. Interaction Energies (ΔE_{int}, in eV) between Intermediates that Appear in the Proposed TPD Mechanisms A, B, and C, and H* or OH*.

Relevant step	Combination	ΔE_{int}
A12	$\mathrm{AcH/V_o{+}Enl/V_o}$, H*	+0.38
A12	$[\mathrm{AcH/V_o, Enl/V_o}]^{\text{C-C}\ddagger}$, H*	+0.48
A12, A13	$\mathrm{CH_3CHOCH_2CHO/VV_o}$, H*	+0.34
A13	$[\mathrm{CH_3CHOCH_2CHO/VV_o}]^{\text{C-H}\ddagger}$, H*	+0.59
A13, A14	$\mathrm{CH_3CHOCHCHO/VV_o}$, H*	+0.25
A14	$[\mathrm{CH_3CHOCHCHO/VV_o}]^{\text{C-O}\ddagger}$, H*	+0.69
A14, Des.	$\mathrm{CrA/V_o}$, H*	+0.20
B12	$\mathrm{Enl/V_o{+}Enl/V_o}$, H*	+0.24
B13	$\mathrm{CH_2CHOCH_2CHO/VV_o}$, H*	+0.24
C12	$\mathrm{AcH^*{+}Enl/V_o}$, H*	0.00
C12	$[\mathrm{AcH^*, Enl/V_o}]^{\text{C-C}\ddagger}$, H*	+0.02
C12, C13	$\mathrm{CH_3CHOCH_2CHO/V_o}$, H*	+0.10
C13	$[\mathrm{CH_3CHOCH_2CHO/V_o}]^{\text{C-H}\ddagger}$, H*	+0.08
C13, C14	$\mathrm{CH_3CHOHCHCHO/V_o}$, H*	+0.17
C14	$[\mathrm{CH_3CHOHCHCHO/V_o}]^{\text{C-O}\ddagger}$, H*	+0.01
C14	$\mathrm{CrA/V_o}$, OH*	-1.49

ΔE_{int} is the difference in DFT total energy between a pair of indicated species co-adsorbed in one surface unit cell state and at infinite separation. "‡" refers to transition state.

separation", in the present models. OH that has a very strong stabilizing interaction with both CrA/V_o and H, so they are treated as coadsorbates in the models.

It should be noted, however, that the diffusion barrier for atomic H on CeO_2(111) has been determined theoretically to be 1.8 eV (GGA+U; U=4.5) [153], which means that the mobility of H is highly limited below 600 K according to DFT, in stark contrast to H on metal surfaces. The coverage of H is therefore likely to be locally non-equilibrated on the surface due to reactions, which complicates the estimation of coverage dependence for reaction energetics, if such an approach were to be used in microkinetic modeling. The fact that the H_2 and H_2O desorption waves appear to be linked (**Figure 3.5**) may also be due to underlying processes, e.g. H atoms searching for H_2 formation sites or loosely bound O anions. If true, our TPD results would suggest the GGA+U diffusion barrier of 1.8 eV reported in the literature to be overestimated by ca. 0.2~0.3 eV, but we are unable to confirm it by locating a lower diffusion barrier on CeO_2(111) theoretically. The reduction of surface by atomic H via water formation on CeO_2(111) might seem like a high-barrier process.

To fully account for all of these effects would require a comprehensive kinetic Monte Carlo model with reaction energetic parameters implemented as explicit functions of local coverages of atomic H, organic intermediates, and surface oxygen vacancies, and with the mobility of H and oxygen vacancies taken into account. It is outside the scope of the present study. While our simple microkinetic approach undoubtedly contains inconsistencies, the purpose of adopting it is to show that the aldol addition mechanism that we propose is fundamentally compatible with the experimental TPD, which sheds light on the microscopic level intricacies of this reaction.

For the ketonization of acetic acid on the fully oxidized $CeO_2(111)$, we propose a TPD mechanism that involves a β-keto-acid species. According to **Table 6**, the proposed TPD mechanism consists of 13 elementary steps. Structures for the proposed reaction intermediates and corresponding transition states are shown in **Figure 3.11** and **Figure 3.12**, respectively.

Table 6. Steps in proposed mechanism for AA TPD on $CeO_2(111)$ with DFT-calculated activation barrier (E_a, in eV), reaction energy (ΔE_{rxn}, in eV), and representative pre-factor (ν, in s^{-1}, at 298.15 K)# for each elementary step

No.	Step	E_a	ΔE_{rxn}	ν
1	$AA^* + ^* \leftrightarrow Ata/V_o + OH^*$	0.77	+0.62	3.64×10^{12}
2	$AA^* + OH^* \leftrightarrow Ata^* + H_2O^*$	0.20	-0.14	3.80×10^{12}
3	$H_2O^* \rightarrow H_2O(g)$	0.52	+0.52	10^{13}
4	$Ata/V_o + ^* \leftrightarrow Ket^* + H^*$	0.95	+0.65	7.99×10^{10}
5	$Ket^* \rightarrow CH_2CO(g) + ^*$	1.19	+1.09	10^{13}
6	$Ata^* + Ket^* \leftrightarrow CH_3CO(O)CH_2COO/V_o$	1.13	+0.82	1.12×10^{11}
7	$CH_3CO(O)CH_2COO/V_o /V_o + H^* \leftrightarrow$ $CH_3CO(OH)CH_2COO/V_o + ^*$	0.66	-0.01	4.71×10^{12}
8	$CH_3CO(OH)CH_2COO/V_o \leftrightarrow CH_3COCH_2COO/V_o +$ OH^*	0.12	-0.42	7.86×10^{12}
9	$CH_3COCH_2COO/V_o + OH^* \leftrightarrow \beta\text{-}KA^*$	0.36	+0.17	1.56×10^{12}
10	$\beta\text{-}KA^* \leftrightarrow Atl^* + CO_3H/V_o$	0.67	+0.09	6.30×10^{12}
11	$Atl^* + CO_3H/V_o \leftrightarrow Ace^* + CO_3/V_o$	0.11	-0.91	2.67×10^{11}
12	$CO_3/V_o \rightarrow CO_2(g) + ^*$	0.58	+0.58	10^{13}
13	$Ace^* \rightarrow Ace(g) + ^*$	0.44	+0.44	10^{13}

E_a and ΔE_{rxn} are based on DFT total energy without ZPE corrections.
#Calculated in the harmonic approximation, except for desorption steps where a value of 10^{13} is used.

Different from AcH, AA can readily reduce the oxidized surface around room temperature by forming a vacancy stabilized acetate (denoted as Ata/V_o, **Figure 3.11a**) and surface adsorbed water, which can readily desorb into the vacuum under UHV condition. This accounts for the 1st water desorption peak in the experimental TPD spectra [76]. Then a surface adsorbed bent

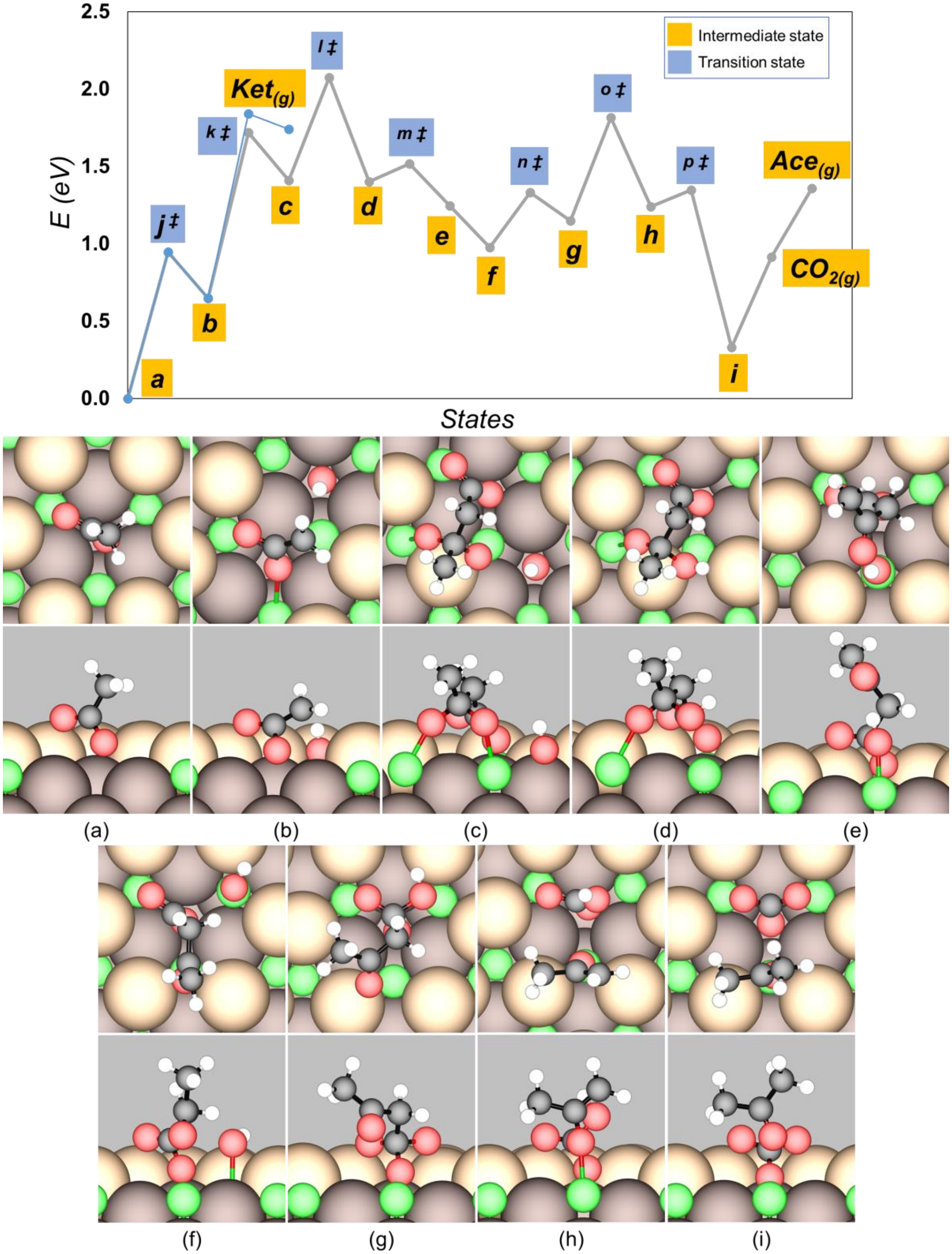

Figure 3.11. TPD mechanism for ketoniztion of acetic acid on the fully oxidized $CeO_2(111)$. (Upper) DFT-caluclated reaction total energy profile for ketene pathway (blue) and acetone pathway (grey). The labeled states are: (a) Ata* + Ata/V_o, (b) Ata* + Ket*, (c) $CH_3CO(O)CH_2COO/V_o$, (d) $CH_3CO(OH)CH_2COO/V_o$, (e) CH_3COCH_2COO/V_o + OH*, (f) CH_3COCH_2COO/V_o + OH*, (g) β-KA* , (h) Atl* + CO_3H/V_o, (i) Ace* + CO_3/V_o.

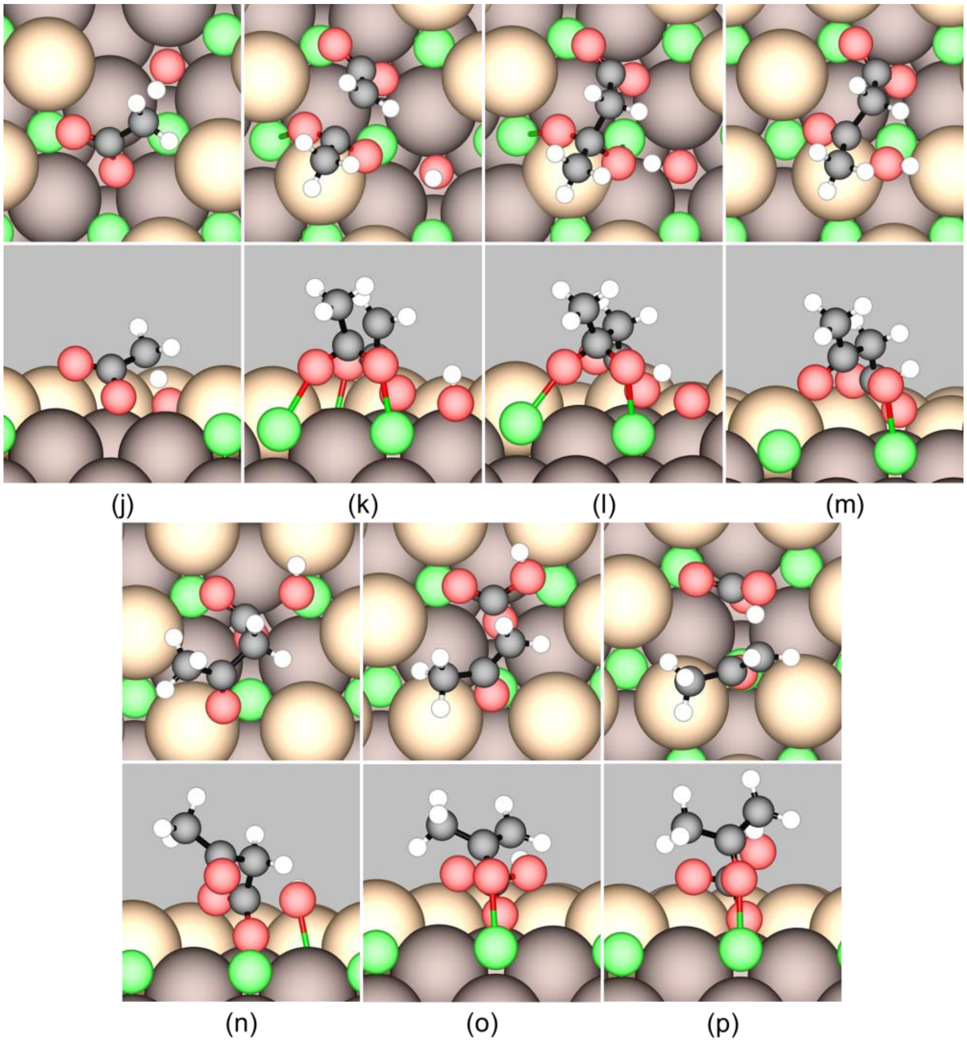

Figure 3.12. Corresponding transition states appeared in the proposed TPD mechanism for ketoniztion of acetic acid on the fully oxidized CeO_2(111). The labeled states are: (j) TS for enolization, (k) TS for C-C coupling, (l) TS for H addition, (m) TS for OH detaching, (n) TS for OH attacking, or β-KA* formation, (o) TS for C-C breaking and (p) TS for H transfer.

ketene (denoted as Ket*, i.e. CH_2COO/V_o, **Figure 3.11b**) is formed via α-H abstraction of Ata/V_o with an activation energy barrier of 0.95 eV, which in contrast is much higher than the α-H abstraction of AcH/V_o. After this H abstraction step, C-C coupling step between the surface adsorbed ketene and nearby surface adsorbed Ata (denoted as Ata*) turns out to be a kinetically significant step with an activation energy barrier of 1.13 eV (TS is shown in **Figure 3.12k**). This finding is in accordance with earlier conclusions that the rate-limiting step is C-C bond formation on monoclinic zirconia surface [166, 167].

The product of C-C coupling, $CH_3CO(O)CH_2COO/V_o$ (**Figure 3.11c**), accepts a H from the surface lattice O and forms $CH_3CO(OH)CH_2COO/V_o$ (**Figure 3.11d**). This H addition facilitates the subsequent facile OH detaching step that cleaves off the internal O. This surface adsorbed OH can rearrange itself firstly, then it attacks the carboxylate group that has been stabilized by the surface oxygen vacancy and forms the surface adsorbed β-keto-acid (denoted as β-KA*, **Figure 3.11g**). The β-keto-acid then decomposes relatively easily via a C-C breaking step with an activation energy barrier of 0.67 eV, and forms surface adsorbed acetonyl species (denoted as Atl*) and a vacancy stabilized bicarbonate species (denoted as HCO_3/V_o). Next step is H transfer from bicarbonate to acetonyl, which forms the final surface adsorbed acetone (denoted as Ace*). This step gives a relatively big energy gain about 0.91 eV.

Our DFT calculated energy profile basically accords with the observed desorption activities in surface science study that acetone is only a minor product, whereas ketene is the major desorption product. Our findings show that the product of C-C coupling binds weakly on the surface. As a result, instead of favoring the bimolecular acetone formation pathway, the C-C coupling product undergoes facile decomposition and contributes to ketene desorption pathway. A similar microkinetic modeling methodology will also be deployed here to validate our mechanistic hypothesis. We expect that it is possible to improve the catalytic performance of ceria towards acetone if the surface can impose a larger stabilization effect on the C-C coupling product than on the other reaction intermediate states. On the other hand, if the stabilization effect is too strong, the catalyst surface would get poisoned by $CH_3CO(O)CH_2COO/V_o$.

3.2 Dephosphorylation Mechanism of Phosphate Monoesters on $CeO_2(111)$

Now gear will be switched to phosphorus chemistry from carbon chemistry, but the main topic is coherent since the catalyst being studied here is still ceria. Firstly, we present and discuss the surface-assisted hydrolysis mechanism for the dephosphorylation of model phosphate monoester, *p*-NPP. The main surface intermediates involved in this mechanism will be presented first, and then the mechanism and its energy profile, which starts with the adsorption of *p*-NPP, followed by the P-O ester bond scission, the formation and desorption of *p*-NP, the hydration of the remaining phosphate group, and finally the desorption of phosphoric acid (H_3PO_4). Then a similar pathway is proposed and investigated for MP. Finally, a linear transition state scaling plot is presented for the activation of the P-O ester bond on $CeO_2(111)$ for several additional organic monophosphates together with *p*-NPP and MP.

3.2.1 Molecular adsorption of p-NPP

Several geometries for molecular adsorption of neutral *p*-NPP are considered, and the minimum-energy configuration (**Figure 3.13a**) involves the formation of a P-O bond between the P atom and a lattice O atom (O_{latt}) in the surface with a bond length of 1.687 Å (**Table 7**), while the P-O ester bond is lengthened from 1.619 Å in the gas phase to 1.706 Å (**Table 8**). The two acidic H atoms are attached to the axial O atom and one of the equatorial O atoms of the phosphate group, respectively. The three equatorial O atoms of the phosphate group are each located on a threefold hollow site above a Ce atom in the 2nd layer (designated as a $3f_c$ site, cf. **Figure 3.13b**). The minimum-energy configuration therefore involves a pentavalent P center with a weakened P-O ester bond and its formation is determined to be barrier-less. The adsorption energy of this adsorption state is -1.04 eV. It is 0.77 eV less stable for both of the acidic H atoms to be attached to equatorial O atoms instead (i.e., with the phosphoryl O atom (P=O) pointing away from surface). Another configuration that we have investigated involves *p*-NPP coordinated to a $3f_c$ site via the phosphoryl O at an O-Ce distance of 2.678 Å, similar to the adsorption modes that previous theoretical studies of phosphate adsorption on oxides have considered [88, 106]. This configuration is calculated to be 0.74 eV less stable than the minimum-energy configuration.

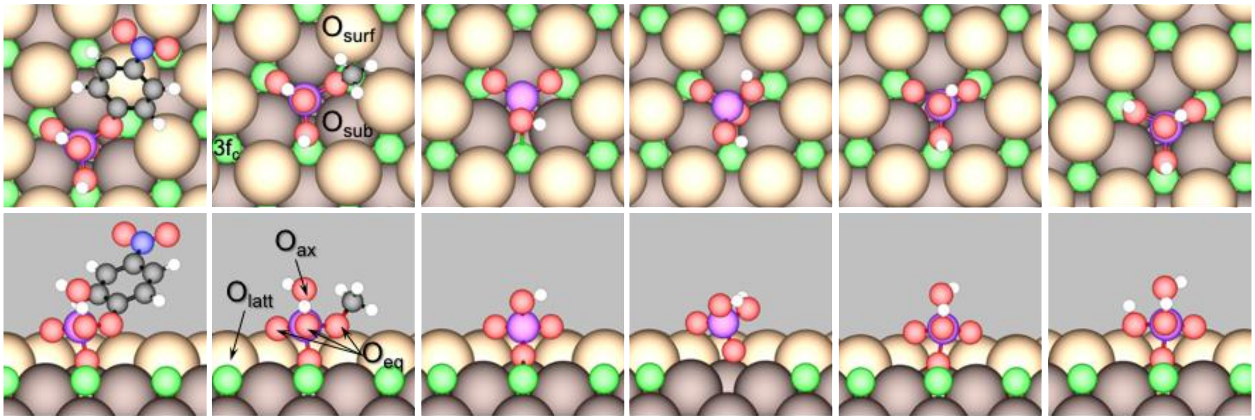

(a) (b) (c) (d) (e) (f)

Figure 3.13. Top (top panels) and side (bottom panels) views of DFT-calculated minimum-energy geometries of (a) *p*-NPP, (b) MP, (c) HPO_3, (d) H_2PO_3, (e) H_2PO_4, and (f) H_3PO_4 adsorbed on $CeO_2(111)$. In each panel, top view is on top and side view is on bottom. Color code: green=Ce, light brown=surface O_{latt},, dark brown=subsurface O_{latt}, red=O, violet=P, black=C, blue=N, and white=H. O_{ax}, O_{eq}, and O_{latt} refer to O atom at the axial, equatorial, and lattice position, respectively.

Table 7. DFT-calculated minimum adsorption energies (ΔE_{ads}, in eV) and corresponding P-O bond lengths (d(P-O_{latt}), in Å), Bader[a] charges (in *e*) of the P atom and the O_{latt} atom beneath it, and magnetic moments of the systems (m.m., in μ_B).

Adsorbate	ΔE_{ads}	d(P-O_{latt})	*e*(P)	*e*(O_{latt})	m.m.
p-NPP	-1.04	1.687	+3.51	-1.34	0
MP	-1.04	1.701	+3.44	-1.31	0
p-NP_x[b]	-0.22	–	–	–	1
p-NP[b]	-0.42	–	–	–	0
CH_3O	-0.63	–	–	–	1
CH_3OH	-0.52	–	–	–	0
HPO_3	-3.02	1.594	+3.54	-1.43	0
H_2PO_3	-3.34	1.546	+3.58	-1.47	1
H_2PO_4	-1.18	1.785	+3.51	-1.13	1
H_3PO_4	-1.15	1.692	+3.50	-1.33	0

Adsorption energies are not zero-point energy-corrected. Adsorbate coverage is 1/9 ML. O_{latt} refers to the surface O atom that forms a bond with P.

[a] Bader charge partition analysis was performed using the approach of Henkelman [168], and the difference between the normal valence charge (6 for O and 5 for P) and Bader charge is reported herein. For comparison, the charge of O_{latt} in bulk CeO_2 is -1.22; the charge of P in gas phase *p*-NPP and MP is +3.55 and +3.56, respectively.

[b] *p*-NP_x: *para*-nitrophenoxide; *p*-NP: *para*-nitrophenol.

3.2.2 Dephosphorylation of p-NPP

The calculated reaction energy profile for the proposed surface-assisted dephosphorylation mechanism for *p*-NPP is shown in **Figure 3.14**. The mechanism begins with the P-O ester bond scission, which begins with the H atom on the axial O atom of the phosphate group rotates to a position where it can form a hydrogen bond with the O atom of the *p*-NP_x group (*para*-

nitrophenoxide or 4-nitrophenoxide) and stabilize the *p*-NP$_x$ group once it is dissociated from the molecule. The P-O bond is further lengthened to 1.858 Å in the transition state (TS, shown in **Figure 3.14iii**). The activation barrier relative to the adsorbed *p*-NPP is a mere 0.13 eV (0.12 eV ZPE-corrected). Once the P-O ester bond is cleaved, the axial H atom on the dissociated H_2PO_3 group is transferred to *p*-NP$_x$ to form *p*-NP (**Figure 3.14iv**). The *p*-NP presumably desorbs first due to weaker adsorption (ΔE_{ads} = -0.42 eV by itself, or -0.40 eV while co-adsorbed with the HPO_3 group). The remaining HPO_3 group then re-arranges itself to adopt the minimum-energy configuration that occupies two 3f$_c$ sites (**Figure 3.14v)**. Both the hydrogen transfer step and the HPO_3 re-arrangement step are found to be barrier-less.

To close the catalytic cycle, the HPO_3 group needs to be hydrated and desorb as H_3PO_4. We explored the direct addition of a water molecule to HPO_3 and found it to be very endothermic with a reaction energy in excess of 2 eV. Instead, hydration preferentially takes place in a step-wise mechanism (**Figure 3.14**). The minimum-energy pathway begins with a water molecule transferring a H atom to the axial O of phosphate, which has lost a H atom in the previous alcohol formation step. This hydrogen transfer step has an activation barrier of 1.05 eV (1.04 eV ZPE-corrected). The remaining hydroxyl group is now located at a distance of 1.831 Å between the P and O atoms in the intermediate state (**Figure 3.14viii**). The next step, OH attack forming H_3PO_4, is very facile with an activation energy of only 0.09 eV (0.06 eV ZPE-corrected). The desorption of H_3PO_4 is endothermic by 1.15 eV (1.07 eV ZPE-corrected). Thus, our calculations show that the hydration of HPO_3 and the desorption of H_3PO_4 are both rate-limiting steps in the overall dephosphorylation process *in vacuo*, with activation energies of ca. 1.1 eV.

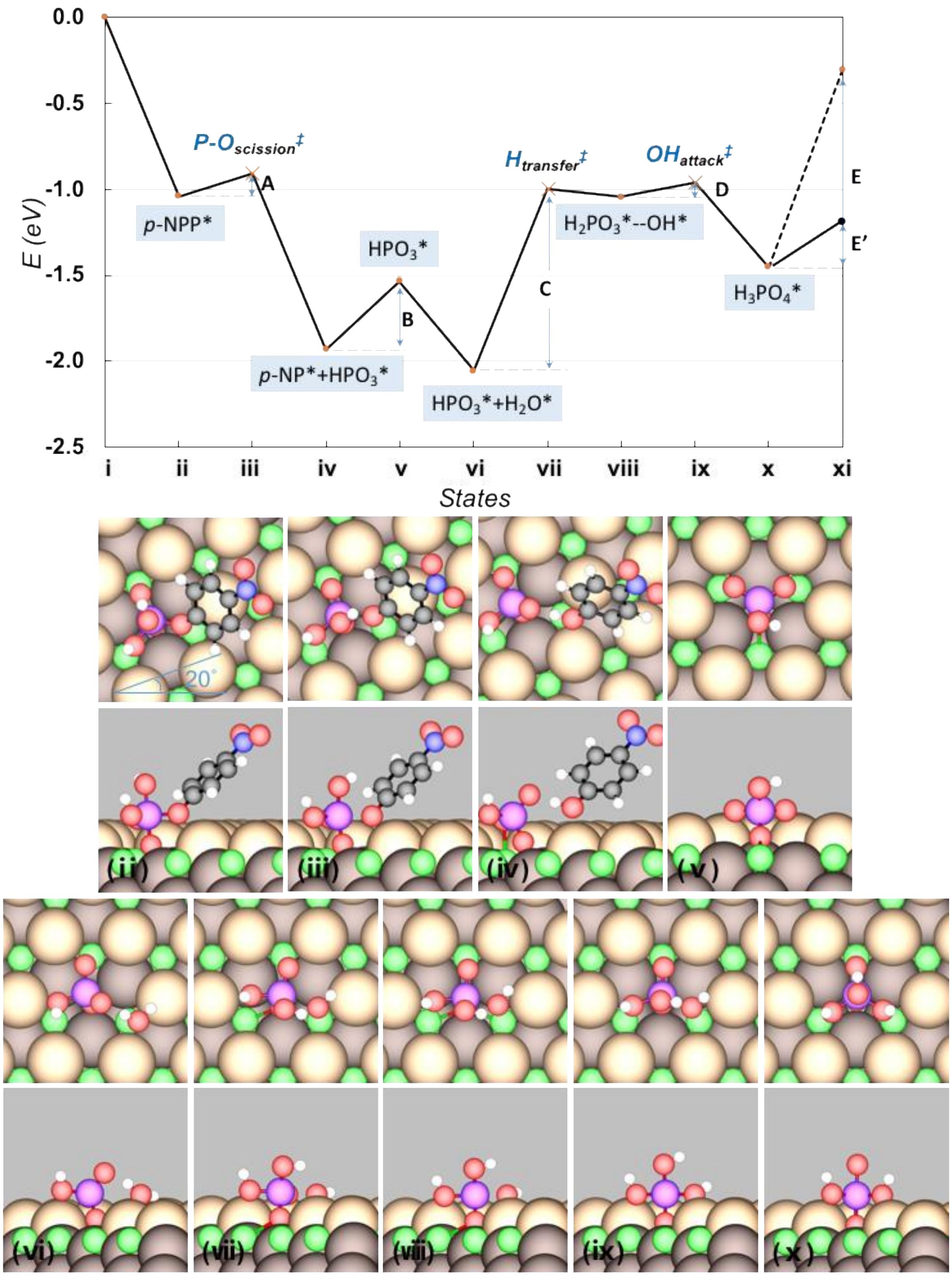

Figure 3.14. DFT-calculated minimum-energy reaction energy profile (not ZPE-corrected; entire path at zero magnetic moment) for the proposed dephosphorylation mechanism for *p*-NPP (including hydration of HPO_3) on $CeO_2(111)$. Transition states are labeled by “‡”.
(Fig. 3.14 caption cont.)

Surface adsorbed species are labeled by “*”. *p*-NPP, H_2O, *p*-NP, and H_3PO_4 are treated as gas-phase molecules in States (i), (i)-(v), (v)-(xi) and (xi), respectively. Labeled activation or desorption processes are: A: P-O ester bond scission, E_a = 0.13 eV; B: *p*-NP desorption to gas phase, ΔE_{des} = 0.41 eV; C: H transfer, E_a = 1.05 eV; D: OH attack, E_a = 0.09 eV; E: H_3PO_4 desorption to gas phase, ΔE_{des} = 1.15 eV; E’: H_3PO_4 desorption to aqueous phase, ΔE_{des} = 0.28 eV. Structures for states in the energy profile are shown in top and side views below the profile. View is rotated by 40° counterclockwise from panel (iv) to (v), and by 60° clockwise from (v) to (vi). Color code: green=Ce, light brown=surface O_{latt}, dark brown=subsurface O_{latt}, red=O, violet=P, black=C, blue=N, and white=H.

Alternatively, we have investigated a stepwise hydration mechanism that begins with water dissociation on the surface, followed by OH attack before H transfer. The corresponding reaction energy profile is shown in **Figure 3.15**. The small barrier to water dissociation (0.32 eV, or 0.21 eV ZPE-corrected) is consistent with prior experimental [74] and theoretical [45, 169, 170] work that reported water dissociation to be very facile and reversible on $CeO_2(111)$. The diffusion of a surface OH group, which positions it following water splitting for attack of the P center, is very facile with a diffusion barrier of ca. 0.1 eV, and so it is kinetically insignificant and therefore neglected from **Figure 3.15**. The OH attack step itself has an activation energy of 0.90 eV (0.92 eV ZPE-corrected), which results in a H_2PO_4 group. The remaining H atom is transferred from the surface to the H_2PO_4 group with an activation energy of 0.61 eV (0.50 eV ZPE-corrected). Thus the total energetic barrier that HPO_3 hydration needs to overcome (i.e. between States vi and ix in **Figures 3.14** and **3.15**) is practically identical for both mechanisms (1.08 vs. 1.15 eV, or 1.08 vs. 1.14 eV ZPE-corrected). We conclude that within the accuracy of DFT it is kinetically equivalent whether OH attack occurs before or after H transfer, at least *in vacuo*.

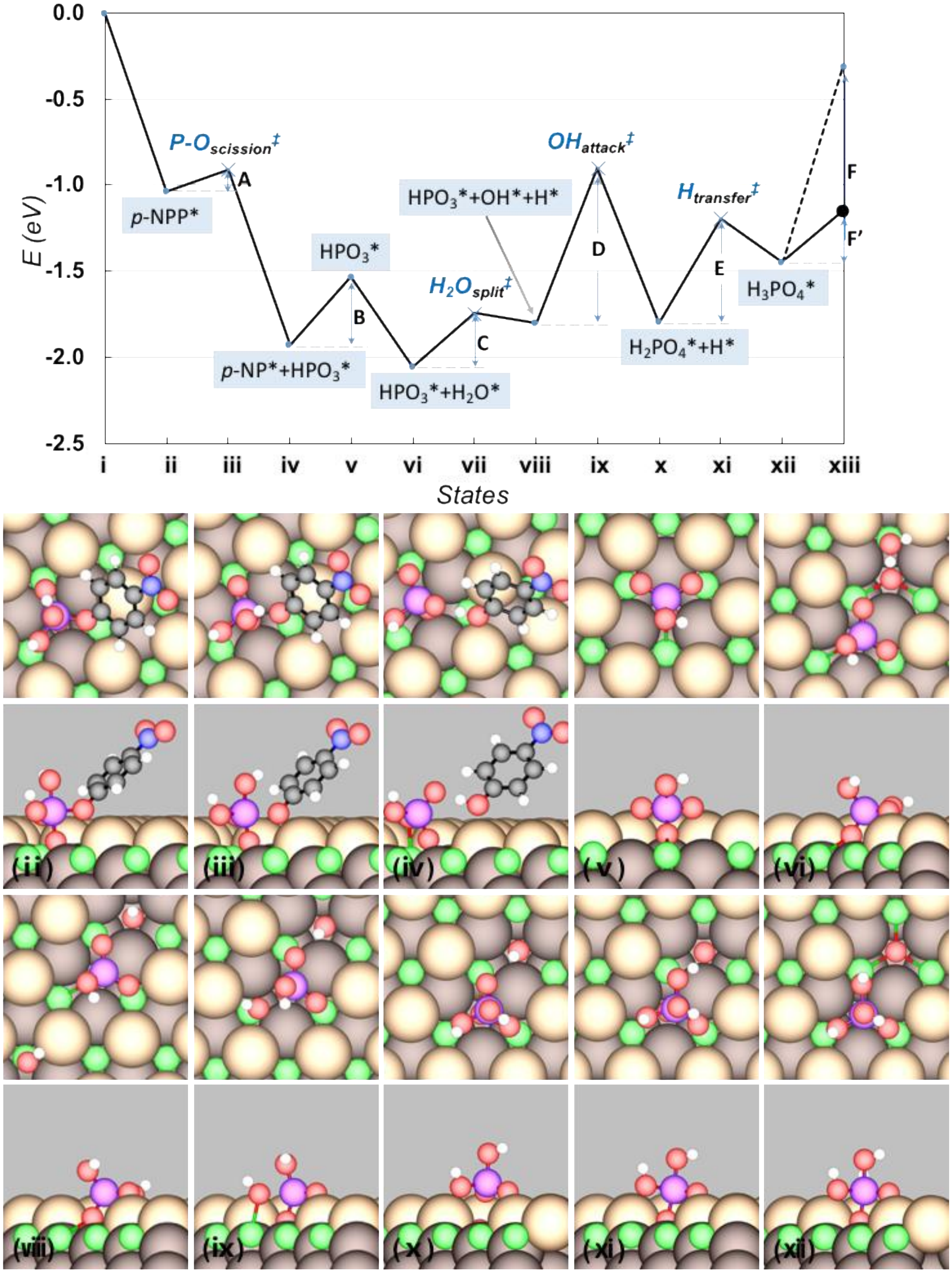

Figure 3.15. DFT-calculated minimum-energy reaction energy profile (not ZPE-corrected; entire path at zero magnetic moment) for the proposed dephosphorylation mechanism for *p*-NPP (including the alternate HPO_3 hydration mechanism) on $CeO_2(111)$. Transition states are labeled (Fig. 3.15 caption cont.)

by “‡”. Surface adsorbed species are labeled by “*”. *p*-NPP, H_2O, *p*-NP and H_3PO_4 are treated as gas phase molecules in States (i), (i)-(v), (v)-(xiii), and (xiii), respectively. Labeled activation or desorption processes are: A: P-O ester bond scission, $E_a = 0.13$ eV; B: *p*-NP desorption to gas phase, $\Delta E_{des} = 0.41$ eV; C: water splitting, $E_a = 0.32$ eV; D: OH attack, $E_a = 0.90$ eV; E: H transfer, $E_a = 0.61$ eV; F: H_3PO_4 desorption to gas phase, $\Delta E_{des} = 1.15$ eV; F’: H_3PO_4 desorption to aqueous phase, $\Delta E_{des} = 0.28$ eV. Structures for states in the energy profile are shown in top and side views below the profile. View is rotated by 40° counterclockwise from panel (iv) to (v), by 60° clockwise from (v) to (vi). Color code: green=Ce, light brown=surface O_{latt}, dark brown=subsurface O_{latt}, red=O, violet=P, black=C, blue=N, and white=H.

Experimentally, Manto et al. have reported the apparent activation energies to be 36.6±1.2, 76.5±1.9, 82.0±3.6, and 105.4±2.9 kJ/mol (100 kJ/mol ≈ 1 eV) for the nanospheres, nano-octahedra (which primarily expose (111) facets), nanorods, and nanocubes, respectively, in comparison to 57.4±2.7 kJ/mol for commercial CeO_2 powder [91]. While our DFT-calculated activation energies based on the rate-limiting steps are ca. 0.3 eV higher than the apparent activation energy corresponding to $CeO_2(111)$, such a direct comparison is not meaningful due to potential concentration effects (e.g. reactant/product concentrations in solution were changing during experiment), coverage effects (surface site competition and lateral interaction are not considered here), as well as solvation effects. Solvation is expected to make the desorption of both the alcohol and phosphoric acid (or their deprotonated forms) much easier because they are well solvated by water [171, 172], so phosphate desorption may no longer be rate-limiting in aqueous phase. This can be seen in **Figures 3.14** and **3.15**, where we have indicated the solvation energy for molecular *p*-NPP in water calculated using an implicit solvent model [173]. We expect the species adsorbed on the ceria surface to also be partially solvated so that the promotional effect of solvation on desorption would be somewhat smaller than depicted. Presently the solvent model cannot be applied to the surface species on ceria due to problems in its implementation. Nonetheless, it is clear that the binding strengths, and thus the corresponding desorption barriers, of these species would be reduced at a water-ceria interface. In addition, there is theoretical evidence in the literature that solvation by water can stabilize the transition states of the formation of polarized bonds by a few tenths of an eV [174, 175], which suggests that the hydration of the phosphate group should occur at more appreciable rates at ambient conditions than the as-calculated activation barrier of ca. 1.1 eV would suggest. Furthermore, Manto et al. have shown that the apparent activation energy of *p*-NPP dephosphorylation can be correlated to the surface density of oxygen vacancies [91], which suggests that the reaction mechanism may be different when *p*-NPP interacts with an oxygen vacancy, a surface element that is not considered in this study. Detailed microkinetic modeling accounting for adsorption/desorption, coverage and solvation effects, and varying extent of reduction in ceria will be attempted in the future to better validate our mechanistic model.

3.2.3 Adsorption and dephosphorylation of MP

The minimum-energy molecular adsorption state of neutral methyl phosphate (MP) has a similar configuration (**Figure 3.16b**) to that of *p*-NPP. Its formation is likewise found to be non-activated, just like for *p*-NPP. As can be seen in **Table 7**, the strength of the P-O_{latt} bond is nearly identical for *p*-NPP, MP, and H_3PO_4, suggesting that the P-O_{latt} bond is little affected by substitution of the acidic hydrogen by an organic group.

The P-O ester bond scission in MP occurs in a similar manner (see **Figure 3.16**) and produces HPO_3 and methanol in one step, and it has a noticeably higher activation energy of 0.50 eV (0.43 eV ZPE-corrected) than in *p*-NPP. After the formation and desorption of methanol, the hydration of the remaining HPO_3 group is identical to that described above. Overall, even

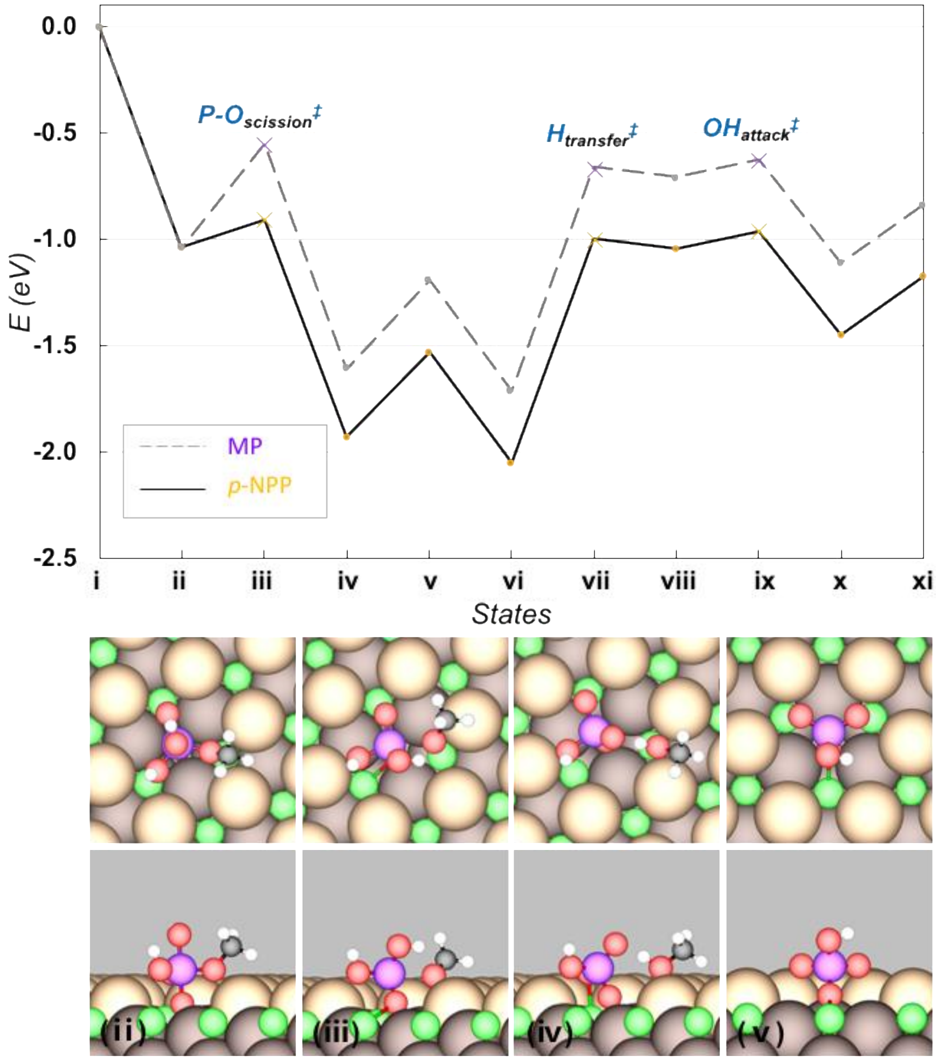

Figure 3.16. DFT-calculated minimum-energy reaction energy profiles (not ZPE-corrected; entire path at zero magnetic moment) for the proposed dephosphorylation mechanism for MP (dash line) and *p*-NPP (solid line) on $CeO_2(111)$. Structures unique to the dephosphorylation of MP are shown in top and side views below the profile. View is rotated by 40° counterclockwise from panel (iv) to (v). Color code: green=Ce, light brown=surface O_{latt}, dark brown=subsurface O_{latt}, red=O, violet=P, black=C, and white=H. Solvation energy of H_3PO_4 in water has been applied to the desorption energy in the final state (xi).

though the methoxy group affects the activation energy of the P-O ester bond, the hydration of the phosphate group remains rate-limiting. We note that P-OCH_3 bond scission in a similar compound, dimethyl methylphosphonate (DMMP), has been reported to occur between 200 and 400 K on $CeO_2(111)$, with which the small activation energy for P-OCH_3 bond scission in MP is in line [101]. It is worth mentioning that DMMP has been frequently studied as a proxy for certain chemical warfare agents, and what its reactivity has in common on a variety of solids under gas phase [100, 102-104] is P-OCH_3 bond scission under mild conditions but hindered removal of the remaining methylphosphonic acid group due to strong adsorption. This pattern is similar to the dephosphorylation of *p*-NPP and MP that we are reporting herein, i.e. facile P-O ester bond scission but hindered removal of the phosphate group, in the absence of solvation effects.

3.2.4 Role of ceria surface in catalyzing hydrolysis of phosphate monoesters

A CeO_2(111) surface presents a large number of exposed O_{latt} atoms that can act as nucleophiles to coordinate to the P atoms in the phosphates, as well as Lewis bases to accept protons from the phosphates or from water. As mentioned above, an optimal pentavalent structure for model phosphate monoesters is formed on CeO_2(111) without any activation energy. Here the P center is activated prior to P-O bond scission by a nucleophilic attack, although it is done by ceria and not water. Then the P-O bond preferentially dissociates, followed by the hydration of the remaining phosphate group and its desorption as H_3PO_4, each of which has an activation energy of ca. 1.1 eV. Thus the surface-assisted dephosphorylation process on CeO_2(111) possesses features of both associative and dissociative mechanisms in aqueous solution but does not strictly conform to either.

Although P-O ester bond scission is not rate-limiting in the dephosphorylation of *p*-NPP and MP on CeO_2(111), it could be significant in other phosphate monoesters. Thus we explored ester bond scission in four additional neutral organic phosphate monoesters on CeO_2(111), including *para*-chlorophenyl phosphate (*p*-ClPP), phenyl phosphate (PP), 2-pyridyl phosphate

(2-py-P), and chloro-methyl phosphate (Cl-MP). The minimum-energy geometries for the molecular adsorption of the four additional phosphates and the corresponding P-O ester bond scission transition states on $CeO_2(111)$ are shown in **Figure 3.17** with additional molecular properties

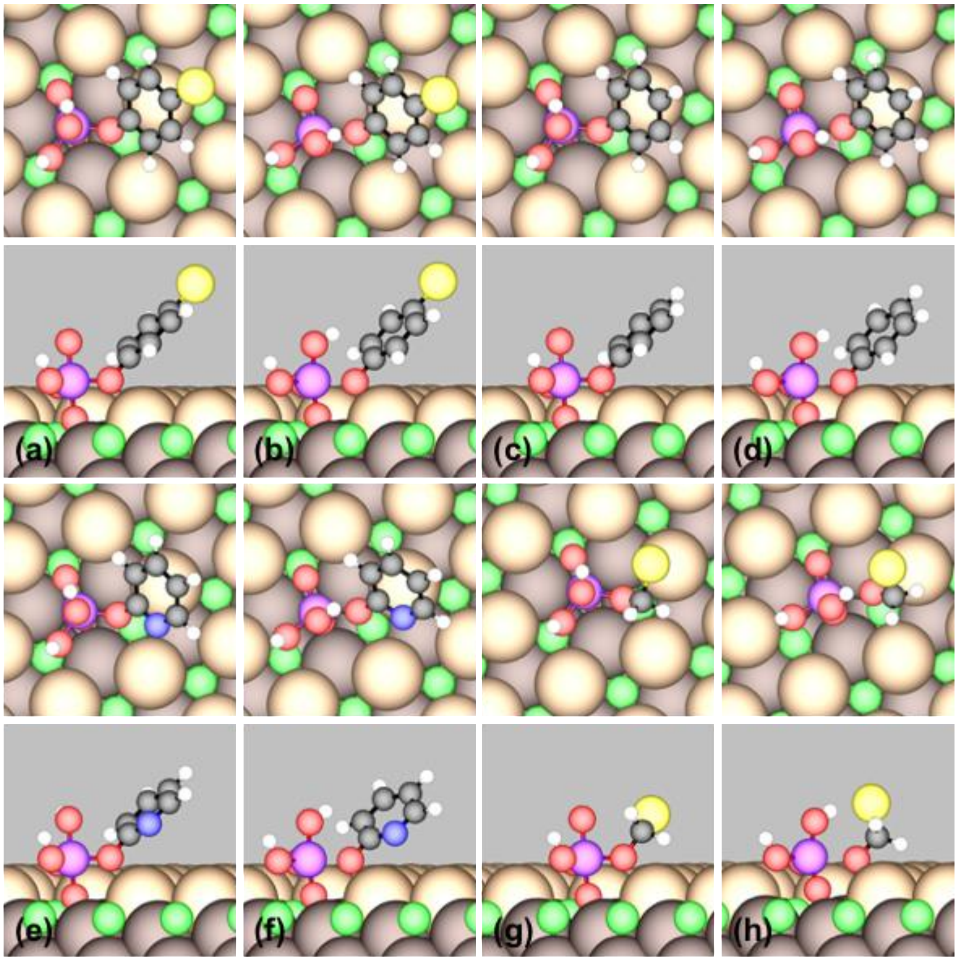

Figure 3.17. Top (top panels) and side (bottom panels) views of DFT-calculated minimum-energy geometries for: (a) molecular adsorption state and (b) corresponding transition state for P-O ester bond scission on $CeO_2(111)$ (same below) for *p*-ClPP; (c) molecular adsorption and (d) transition state for PP; (e) molecular adsorption and (f) transition state for 2-py-P; (g) molecular adsorption and (h) transition state for Cl-MP. Color code: green=Ce, light brown=surface O_{latt},, dark brown= subsurface O_{latt}, red=O, violet=P, black=C, blue=N, white=H, and yellow=Cl.

listed in **Table 8**. As shown in **Figure 3.18**, a linear relation with a slope of 0.66 results, which relates the energy of the transition state of P-O ester bond scission to the energies of the dissociated moieties (alkoxide and H_2PO_3) on $CeO_2(111)$. The correlation is not particularly strong possibly because the P-O bonds in most of these phosphate monoesters are significantly weakened on $CeO_2(111)$, causing the activation energies of the P-O ester bond scission fall

Table 8. DFT-calculated minimum adsorption energies (ΔE_{ads}, in eV) and corresponding P-O bond lengths (d(P-O_{latt}), in Å; ester bond d(P-O), in Å; gas-phase ester bond (d(P-O)^{gas}, in Å) included for comparison), and magnetic moments (m.m., in μ_B).

Adsorbate	ΔE_{ads}	pK_a[†]	d(P-O_{latt})	d(P-O)	d(P-O)^{gas}	*e*(P)	*e*(O_{latt})	m.m.
p-NPP	-1.04	–	1.687	1.706	1.619	+3.51	-1.34	0
MP	-1.04	–	1.701	1.670	1.599	+3.44	-1.31	0
p-ClPP	-0.99	–	1.692	1.703	1.606	+3.47	-1.32	0
PP	-0.98	–	1.694	1.697	1.602	+3.47	-1.32	0
2-py-P	-0.65	–	1.690	1.694	1.666	+3.46	-1.33	0
Cl-MP	-1.03	–	1.691	1.707	1.640	+3.45	-1.32	0
p-NP_x	-0.22	7.1	–	–	–	–	–	1
CH_3O	-0.63	15.5	–	–	–	–	–	1
p-ClP_x	-0.09	9.4	–	–	–	–	–	1
phenoxy	-0.23	10.0	–	–	–	–	–	1
2-oxopyridine	-0.30	n/a	–	–	–	–	–	1
$ClCH_2O$	-0.58	n/a	–	–	–	–	–	1

Adsorption energies are not ZPE-corrected. Adsorbate coverage is 1/9 ML. O_{latt} refers to the surface O atom that forms a bond with P.

[†] pK_a values of *p*-NP_x, CH_3O, *p*-ClP_x, and phenoxy are obtained from Ref. [95].

within DFT margins of error and thus making the accurate capture of the transition states challenging. Nonetheless, the energies of the dissociated moieties may still be used to provide quick estimates for the energies of the transition states of P-O ester bond scission and therefore

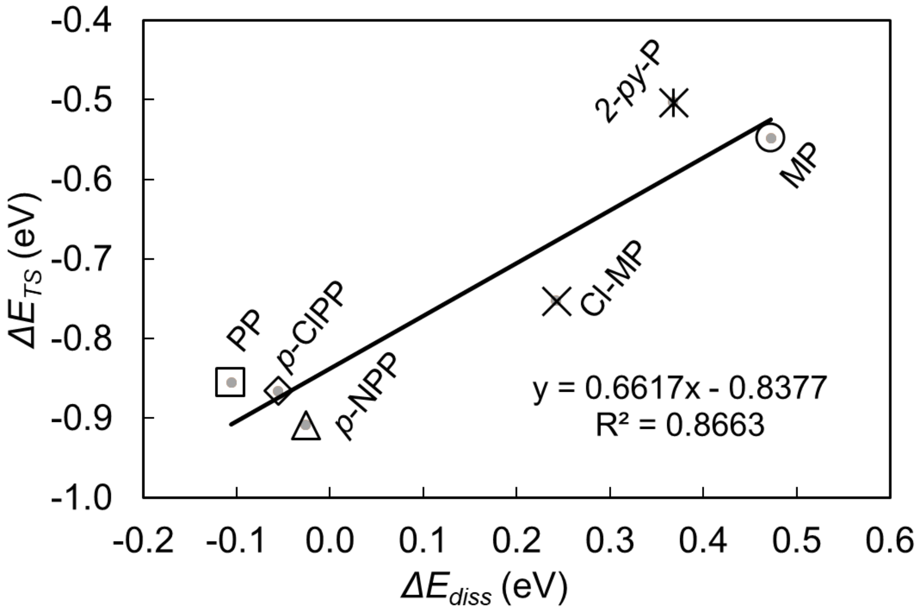

Figure 3.18. Transition state scaling relation between the adsorption energies of the transition states for P-O ester bond scission of model phosphate monoesters and the adsorption energies of the dissociated fragments (alkoxide and H_2PO_3, at infinite separation) on $CeO_2(111)$. The energies are referenced to the corresponding neutral gas-phase phosphate monoesters [176].

the corresponding P-O ester bond scission barriers for other phosphate monoesters. As summarized in **Table 9**, the activation energies for activating the P-O ester bonds in these phosphate monoesters on $CeO_2(111)$ are also closely related to the corresponding P-O ester bond energies in gas phase, and they are all significantly lower than the activation energies for phosphate hydration and desorption *in vacuo*.

The potential significance of ceria as a catalyst for dephosphorylation is suggested by **Figure 3.18** and **Table 9**. Ceria can readily weaken the P-O ester bond to the extent that P-O ester bond scission is kinetically insignificant for a range of phosphate monoesters compared to phosphate hydration and desorption, and the proposed surface-assisted dephosphorylation mechanism should apply to all of the phosphate monoesters. In other words, our calculations predict that the intrinsic catalytic activity of $CeO_2(111)$ toward dephosphorylation should be independent of the alkoxide group. This is true even for MP, in which methoxy is a poor leaving group that causes the hydrolysis of MP to have a significant activation energy in aqueous

Table 9. Gas-phase P-O ester bond energies ($E_b^{\text{P-O}}$, in eV), corresponding activation energies for P-O ester bond scission on $CeO_2(111)$ (E_a and zero-point energy corrected value E_a^{ZPE}, in eV), energies of transition state relative to gas phase molecule (ΔE_{TS}, in eV), and energies of dissociated moieties at infinite separation relative to gas phase molecule (ΔE_{diss}, in eV) for model phosphate monoesters on $CeO_2(111)$

Species	$E_b^{\text{P-O}}$	E_a	E_a^{ZPE}	ΔE_{TS}	ΔE_{diss}
p-NPP	3.54	0.13	0.12	-0.91	-0.03
MP	4.45	0.50	0.43	-0.55	0.47
p-ClPP	3.37	0.13	0.11	-0.87	-0.06
PP	3.47	0.13	0.11	-0.86	-0.11
2-py-P	4.01	0.14	0.13	-0.50	0.37
Cl-MP	4.17	0.28	0.23	-0.75	0.24

solution. Thus ceria and ceria related materials may have the potential to be developed into environmental phosphorus recovery and phosphate detoxification technologies for a variety of organic phosphates. Whether ceria does have significant catalytic dephosphorylation activity toward other types of organophosphates, such as phosphate diesters and triesters [177] and phosphonates and phosphorothioates (notable examples of which include chlorpyrifos and glyphosate), will be the subject of our future studies.

3.3 Resonant Photoelectron Study of the Electronic Nature of Ceria

Oxygen storage capacity is one of the characteristic properties of ceria-based materials, and it can be measured conventionally by either CO/H_2 consumption or O_2 intake experiments. In fact, the interplay sees quite a few phase transitions within the two limit phases: Ce_2O_3 and CeO_2. From the electronic perspective, the oxidation state of Ce changes between 3+ and 4+, which is fundamentally due to the localization and delocalization of the electron at the Ce *4f* level, respectively. The commonly used technique to determine the relative ratio of Ce^{3+}/Ce^{4+} is measuring the Ce *3d* or *4d* core level by X-ray photo-emission spectroscopy (XPS) [178]: quantitative analysis of the oxidation state can be achieved by linear fitting the sample's spectra with the spectra of the two reference limits. Recently, a method called resonant photoelectron spectroscopy (RPES) focusing on valence level has been developed and showed several advantages over the conventional core level XPS method [13]: higher count rates, larger contrast for small oxidation state fluctuation, and higher surface sensitivity.

A closer examination of the $CeO_2(111)$ and *c*-$Ce_2O_3(111)$ surfaces by combining angle-resolved RPES experiments and electronic structure calculations reveals the covalent nature of CeO_2 that lies in the hybridization of Ce *4f* state and O *2p* states, while a non-dispersive (i.e.

highly localized) *4f* state only exists in *c*-Ce_2O_3 [179]. As shown in **Figure 3.19**, for CeO_2(111), the hybridization of Ce *4f* and O *2p* states can be seen both in the on/off resonant modes in the angle-resolved RPES experiments, which is in qualitive agreement with the *p*DOS spectra

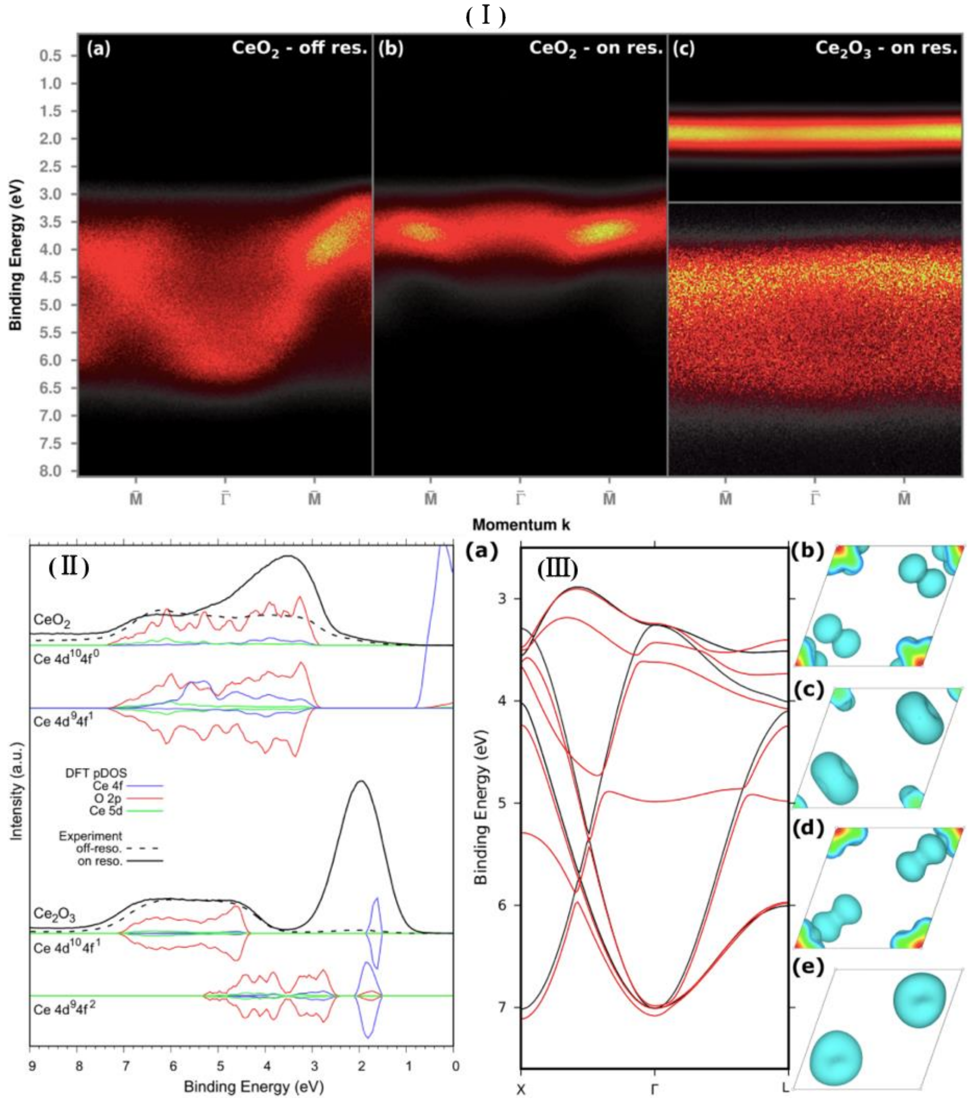

Figure 3.19. (I) Dispersion of the valence band in CeO_2 and *c*-Ce_2O_3 in the M - Γ- M direction of the surface Brillouin zone followed by resonant angle-resolved photoelectron spectroscopy. (II) Partial density of states (pDOS) of CeO_2 and *c*-Ce_2O_3 as calculated using the HSE06 exchange-correlation functional and measured by photoelectron spectroscopy (PES). (III) Band structure of CeO_2 calculated along X - Γ- L for the ground state (black) and the intermediate $4d^9 4f^1$ state (red), with calculated Kohn-Sham wave functions at the point of CeO_2 in the intermediate state.

calculated by DFT. On the other hand, for *c*-Ce_2O_3(111), no admixture of Ce *4f* and O *2p* exists due to the highly localized nature of the *4f* electrons. Therefore, our study confirmed the covalent nature of CeO_2 that is caused by cation-anion hybridization with electrons tied up in the ligand states.

SUMMARY

The potential applications of ceria as catalyst in upgrading biomass-derived oxygenates and recovering phosphorus from organic pollutants have been studied throughout the research project, using self-consistent, periodic density functional theory calculations primarily at the GGA+U-PW91 level. Mean-field microkinetic modeling using DFT-calculated energetics as inputs can simulate spectroscopic outcomes that can be directly compared with the spectroscopic evidence from surface science experiments, thus it (DFT+MkM) turns out to be a useful tool to validate mechanistic hypothesis.

The temperature programmed desorption of model oxygenates, i.e. AcH and AA, on $CeO_2(111)$ surfaces under UHV condition have been studied in detail. For the AcH-TPD system, a general TPD mechanism has been proposed to account for the formation of various C_2 species. The outcomes of MkM are in close agreement with the observed desorption activities and infrared evidence. Therefore, our results suggested that oxygen vacancies play the critical role of activating the carbonyl bond by stabilizing the carbonyl O with exposed Lewis acid site, which transforms the carbonyl bond to a C-O single bond, and allows this C atom to engage in bonding with another AcH. Afterwards, decomposition of the dimer state forms the enolate (CH_2CHO) and its derivatives, which in turn account for the formation of ethylene and acetylene via intermolecular hydrogen transfer and deoxygenation.

Further attempts have been made to explain the discrepancy between the AcH-TPD experiment (UHV condition) and AcH-TPSR experiment (flow reactor condition). Taking advantages of the surface dominant enolate species that spans a wide temperature window of ca. 200 K, our most recent AcH-TPD experiment using a tailored double-ramping procedure

managed to capture appreciable amount of CrA formation under UHV condition. Three expanded TPD mechanisms were then proposed to account for CrA formation, one of which was validated using the DFT+MkM methodology. Therefore, our results suggested the catalytic active site is a vacancy dimer that is created *in-situ* via facile vacancy migration.

For the AA-TPD system, our calculations showed AA could readily reduce the fully oxidized $CeO_2(111)$ around room temperature under UHV condition, which agrees with the observed early water desorption activity in the TPD experiments. However, the kinetic difficulties of the acetone pathway lie in two aspects: one is the α-H abstraction of the vacancy stabilized acetate, another is the C-C coupling step. The weak binding of the C-C coupling product on the surface makes its decomposition facile, which would eventually contribute to ketene desorption. This finding agrees with the experimental evidence that ketene is a major product other than acetone under UHV condition.

The dephosphorylation of two model phosphate monoesters, neutral *p*-NPP and MP, on $CeO_2(111)$ has been investigated theoretically *in vacuo*. A surface-assisted hydrolysis mechanism is proposed, which involves the barrier-less activation of the phosphates by adsorption on $CeO_2(111)$ and formation of a $P\text{-}O_{latt}$ bond, facile dissociation of the P-O ester bond, hydration of the remaining HPO_3 group, and desorption of H_3PO_4. The last two steps are found to be rate-limiting *in vacuo* with activation energies of ca. 1.1 eV, both of which are expected to be reduced by solvation effects. P-O ester bond scission in several other phosphate monoesters has been investigated and is found consistently to have low activation energies, in contrast to the large bond energy of the P-O ester bond in the isolated molecules. The overall catalytic performance of $CeO_2(111)$ in dephosphorylation process is therefore predicted to be independent of the nature of the alkoxide group.

Other than its successful application in the automotive emission control industry, our findings provide insights for the potential engineering of ceria into viable catalysts for upgrading small organic oxygenates derived from biomass feedstock. Besides, our findings suggest that ceria can be catalytically active toward the dephosphorylation of organic phosphates in general under ambient conditions and may potentially serve as the core of technologies for the recycling of phosphorus from, and detoxification of, organic phosphates in the environment.

REFERENCES

[1] A. Trovarelli, P. Fornasiero, Catalysis by Ceria and Related Materials, Imperial College Press, London, 2002.

[2] T. Montini, M. Melchionna, M. Monai, P. Fornasiero, Fundamentals and Catalytic Applications of CeO_2-Based Materials, Chem. Rev., 116 (2016) 5987-6041.

[3] J. Kašpar, P. Fornasiero, M. Graziani, Use of CeO_2-Based Oxides in the Three-Way Catalysis, Catal. Today, 50 (1999) 285-298.

[4] R.M. Heck, R.J. Farrauto, S.T. Gulati, Catalytic Air Pollution Control: Commercial Technology, 3rd ed., John Wiley & Sons, Hoboken, 2009.

[5] J.A. Rodriguez, S. Ma, P. Liu, J. Hrbek, J. Evans, M. Pérez, Activity of CeO_x and TiO_x Nanoparticles Grown on Au(111) in the Water-Gas Shift Reaction, Science, 318 (2007) 1757-1760.

[6] G.A. Deluga, J.R. Salge, L.D. Schmidt, X.E. Verykios, Renewable Hydrogen from Ethanol by Autothermal Reforming, Science, 303 (2004) 993-997.

[7] J. Graciani, K. Mudiyanselage, F. Xu, A.E. Baber, J. Evans, S.D. Senanayake, D.J. Stacchiola, P. Liu, J. Hrbek, J.F. Sanz, J.A. Rodriguez, Highly Active Copper-Ceria and Copper-Ceria-Titania Catalysts for Methanol Synthesis from CO_2, Science, 345 (2014) 546-550.

[8] E. Aneggi, C. de Leitenburg, G. Dolcetti, A. Trovarelli, Promotional Effect of Rare Earths and Transition Metals in the Combustion of Diesel Soot over CeO_2 and CeO_2-ZrO_2, Catal. Today, 114 (2006) 40-47.

[9] B.C.H. Steele, Materials for IT-SOFC Stacks: 35 years R&D: The Inevitability of Gradualness?, Solid State Ionics, 134 (2000) 3-20.

[10] G.P. Smestad, A. Steinfeld, Review: Photochemical and Thermochemical Production of Solar Fuels from H_2O and CO_2 Using Metal Oxide Catalysts, Ind. Eng. Chem. Res., 51 (2012) 11828-11840.

[11] M. Nolan, S.C. Parker, G.W. Watson, The Electronic Structure of Oxygen Vacancy Defects at the Low Index Surfaces of Ceria, Surf. Sci., 595 (2005) 223-232.

[12] D.R. Mullins, P.V. Radulovic, S.H. Overbury, Ordered Cerium Oxide Thin Films Grown on Ru(0001) and Ni(111), Surf. Sci., 429 (1999) 186-198.

[13] V. Matolín, J. Libra, M. Škoda, N. Tsud, K.C. Prince, T. Skála, Methanol Adsorption on a CeO_2(111)/Cu(111) Thin Film Model Catalyst, Surf. Sci., 603 (2009) 1087-1092.

[14] P. Luches, F. Pagliuca, S. Valeri, Morphology, Stoichiometry, and Interface Structure of CeO_2 Ultrathin Films on Pt(111), J. Phys. Chem. C, 115 (2011) 10718-10726.

[15] S. Eck, C. Castellarin-Cudia, S. Surnev, M.G. Ramsey, F.P. Netzer, Growth and Thermal Properties of Ultrathin Cerium Oxide Layers on Rh(111), Surf. Sci., 520 (2002) 173-185.

[16] M. Alexandrou, R.M. Nix, The Growth, Structure and Stability of Ceria Overlayers on Pd(111), Surf. Sci., 321 (1994) 47-57.

[17] S. Ma, J.A. Rodriguez, J. Hrbek, STM Study of the Growth of Cerium Oxide Nanoparticles on Au(111), Surf. Sci., 602 (2008) 3272-3278.

[18] D.R. Mullins, The Surface Chemistry of Cerium Oxide, Surf. Sci. Rep., 70 (2015) 42-85.

[19] J.L. Lu, H.J. Gao, S. Shaikhutdinov, H.J. Freund, Morphology and Defect Structure of the CeO_2(111) Films Grown on Ru(0001) as Studied by Scanning Tunneling Microscopy, Surf. Sci., 600 (2006) 5004-5010.

[20] J. Zhou, A.P. Baddorf, D.R. Mullins, S.H. Overbury, Growth and Characterization of Rh and Pd Nanoparticles on Oxidized and Reduced CeO_x(111) Thin Films by Scanning Tunneling Microscopy, J. Phys. Chem. C, 112 (2008) 9336-9345.

[21] S. Gritschneder, M. Reichling, Structural Elements of CeO_2(111) Surfaces, Nanotechnology, 18 (2007) 044024.

[22] M.A. Barteau, Organic Reactions at Well-Defined Oxide Surfaces, Chem. Rev., 96 (1996) 1413-1430.

[23] M.I. Zaki, M.A. Hasan, L. Pasupulety, Surface Reactions of Acetone on Al_2O_3, TiO_2, ZrO_2, and CeO_2: IR Spectroscopic Assessment of Impacts of the Surface Acid−Base Properties, Langmuir, 17 (2001) 768-774.

[24] M.J. Climent, A. Corma, S. Iborra, A. Velty, Designing the Adequate Base Solid Catalyst with Lewis or Brønsted Basic Sites or with Acid–Base Pairs, J. Mol. Catal. A: Chem., 182-183 (2002) 327-342.

[25] R.W. Snell, E. Combs, B.H. Shanks, Aldol Condensations Using Bio-Oil Model Compounds: The Role of Acid–Base Bi-Functionality, Top. Catal., 53 (2010) 1248-1253.

[26] S. Wang, K. Goulas, E. Iglesia, Condensation and Esterification Reactions of Alkanals, Alkanones, and Alkanols on TiO_2: Elementary Steps, Site Requirements, and Synergistic Effects of Bifunctional Strategies, J. Catal., 340 (2016) 302-320.

[27] J.L.F. Da Silva, Stability of the Ce_2O_3 Phases: A DFT + U Investigation, Phys. Rev. B, 76 (2007) 193108.

[28] M. Zinkevich, D. Djurovic, F. Aldinger, Thermodynamic Modelling of the Cerium–Oxygen System, Solid State Ionics, 177 (2006) 989-1001.

[29] R.J. Ackermann, E.G. Rauh, A High-Temperature Study of the Stoichiometry, Phase Behavior, Vaporization Characteristics, and Thermodynamic Properties of the Cerium + Oxygen System, J. Chem. Thermodyn., 3 (1971) 609-624.

[30] M.D. Watson, Phase Equilibrium for Solid and Molten CeO_{2-x} Above 1500 °C, Ph.D. Thesis, Georgia Institute of Technology (1977).

[31] N.V. Skorodumova, S.I. Simak, B.I. Lundqvist, I.A. Abrikosov, B. Johansson, Quantum Origin of the Oxygen Storage Capability of Ceria, Phys. Rev. Lett., 89 (2002) 166601.

[32] T. Duchoň, F. Dvořák, M. Aulická, V. Stetsovych, M. Vorokhta, D. Mazur, K. Veltruská, T. Skála, J. Mysliveček, I. Matolínová, V. Matolín, Ordered Phases of Reduced Ceria As Epitaxial Films on Cu(111), J. Phys. Chem. C, 118 (2014) 357-365.

[33] R. Olbrich, G.E. Murgida, V. Ferrari, C. Barth, A.M. Llois, M. Reichling, M.V. Ganduglia-Pirovano, Surface Stabilizes Ceria in Unexpected Stoichiometry, J. Phys. Chem. C, 121 (2017) 6844-6851.

[34] F. Dvořák, L. Szabová, V. Johánek, M. Farnesi Camellone, V. Stetsovych, M. Vorokhta, A. Tovt, T. Skála, I. Matolínová, Y. Tateyama, J. Mysliveček, S. Fabris, V. Matolín, Bulk Hydroxylation and Effective Water Splitting by Highly Reduced Cerium Oxide: The Role of O Vacancy Coordination, ACS Catal., 8 (2018) 4354-4363.

[35] I. Chorkendorff, J.W. Niemantsverdriet, Concepts of Modern Catalysis and Kinetics, Wiley-VCH, Weinheim, 2003.

[36] R.A. van Santen, M. Neurock, Molecular Heterogeneous Catalysis, Wiley-VCH, Weinheim, 2006.

[37] G. Ertl, Reactions at Solid Surfaces, John Wiley & Sons, Hoboken, 2009.

[38] J.K. Nørskov, F. Studt, F. Abild-Pedersen, T. Bligaard, Fundamental Concepts in Heterogeneous Catalysis, John Wiley & Sons, Hoboken, 2014.

[39] T.X.T. Sayle, S.C. Parker, D.C. Sayle, Shape of CeO_2 Nanoparticles Using Simulated Amorphisation and Recrystallisation, Chem. Commun., 0 (2004) 2438-2439.

[40] A. Trovarelli, P. Fornasiero, Catalysis by Ceria and Related Materials, 2nd ed., Imperial College Press, London, 2013.

[41] A. Trovarelli, C. de Leitenburg, M. Boaro, G. Dolcetti, The Utilization of Ceria in Industrial Catalysis, Catal. Today, 50 (1999) 353-367.

[42] J.A. Rodriguez, D.C. Grinter, Z. Liu, R.M. Palomino, S.D. Senanayake, Ceria-Based Model Catalysts: Fundamental Studies on the Importance of the Metal-Ceria Interface in CO Oxidation, the Water-Gas Shift, CO_2 Hydrogenation, and Methane and Alcohol Reforming, Chem. Soc. Rev., 46 (2017) 1824-1841.

[43] J. Paier, C. Penschke, J. Sauer, Oxygen Defects and Surface Chemistry of Ceria: Quantum Chemical Studies Compared to Experiment, Chem. Rev., 113 (2013) 3949-3985.

[44] Y.-G. Wang, D. Mei, V.-A. Glezakou, J. Li, R. Rousseau, Dynamic Formation of Single-Atom Catalytic Active Sites on Ceria-Supported Gold Nanoparticles, Nat. Commun., 6 (2015) 6511.

[45] M.F. Camellone, F.R. Negreiros, L. Szabová, Y. Tateyama, S. Fabris, Catalytic Proton Dynamics at the Water/Solid Interface of Ceria-Supported Pt Clusters, J. Am. Chem. Soc., 138 (2016) 11560-11567.

[46] D.C. Sayle, X. Feng, Y. Ding, Z.L. Wang, T.X.T. Sayle, “Simulating Synthesis”: Ceria Nanosphere Self-Assembly into Nanorods and Framework Architectures, J. Am. Chem. Soc., 129 (2007) 7924-7935.

[47] A. Trovarelli, Catalytic Properties of Ceria and CeO2-Containing Materials, Catal. Rev., 38 (1996) 439-520.

[48] P. Granger, L. Delannoy, J.J. Lecomte, C. Dathy, H. Praliaud, L. Leclercq, G. Leclercq, Kinetics of the CO+NO Reaction over Bimetallic Platinum–Rhodium on Alumina: Effect of Ceria Incorporation into Noble Metals, J. Catal., 207 (2002) 202-212.

[49] P. Bera, K.C. Patil, V. Jayaram, G.N. Subbanna, M.S. Hegde, Ionic Dispersion of Pt and Pd on CeO2 by Combustion Method: Effect of Metal–Ceria Interaction on Catalytic Activities for NO Reduction and CO and Hydrocarbon Oxidation, J. Catal., 196 (2000) 293-301.

[50] K. Momma, F. Izumi, VESTA: A Three-Dimensional Visualization System for Electronic and Structural Analysis, J. Appl. Crystallogr., 41 (2008) 653-658.

[51] D. Mohan, C.U. Pittman, P.H. Steele, Pyrolysis of Wood/Biomass for Bio-Oil: A Critical Review, Energ. Fuel, 20 (2006) 848-889.

[52] G.W. Huber, S. Iborra, A. Corma, Synthesis of Transportation Fuels from Biomass: Chemistry, Catalysts, and Engineering, Chem. Rev., 106 (2006) 4044-4098.

[53] D.M. Alonso, J.Q. Bond, J.A. Dumesic, Catalytic Conversion of Biomass to Biofuels, Green Chem., 12 (2010) 1493-1513.

[54] M. Pruski, A.D. Sadow, I.I. Slowing, C.L. Marshall, P. Stair, J.A. Rodriguez, A. Harris, G.A. Somorjai, J. Biener, C. Matranga, C. Wang, J.A. Schaidle, G.T. Beckham, D.A. Ruddy, T. Deutsch, S.M. Alia, C. Narula, S.H. Overbury, T. Toops, R.M. Bullock, C.H.F. Peden, Y. Wang, M.D. Allendorf, J. Nørskov, T. Bligaard, Virtual Special Issue on Catalysis at the U.S. Department of Energy’s National Laboratories, ACS Catal., 6 (2016) 3227-3235.

[55] M. Langholtz, B. Stokes, L. Eaton, 2016 Billion-Ton Report: Advancing Domestic Resources for a Thriving Bioeconomy, 1 (2016) 1-411.

[56] G.W. Huber, J.A. Dumesic, An Overview of Aqueous-Phase Catalytic Processes for Production of Hydrogen and Alkanes in a Biorefinery, Catal. Today, 111 (2006) 119-132.

[57] H. Idriss, C. Diagne, J.P. Hindermann, A. Kiennemann, M.A. Barteau, Reactions of Acetaldehyde on CeO_2 and CeO_2-Supported Catalysts, J. Catal., 155 (1995) 219-237.

[58] T.S. Hendren, K.M. Dooley, Kinetics of Catalyzed Acid/Acid and Acid/Aldehyde Condensation Reactions to Non-Symmetric Ketones, Catal. Today, 85 (2003) 333-351.

[59] E.I. Gürbüz, E.L. Kunkes, J.A. Dumesic, Integration of C-C Coupling Reactions of Biomass-Derived Oxygenates to Fuel-Grade Compounds, Appl. Catal., B, 94 (2010) 134-141.

[60] A. Gangadharan, M. Shen, T. Sooknoi, D.E. Resasco, R.G. Mallinson, Condensation Reactions of Propanal over $Ce_xZr_{1-x}O_2$ Mixed Oxide Catalysts, Appl. Catal., A, 385 (2010) 80-91.

[61] J.I. Di Cosimo, G. Torres, C.R. Apesteguía, One-Step MIBK Synthesis: A New Process from 2-Propanol, J. Catal., 208 (2002) 114-123.

[62] L. Vivier, D. Duprez, Ceria-Based Solid Catalysts for Organic Chemistry, ChemSusChem, 3 (2010) 654-678.

[63] C.A. Gaertner, J.C. Serrano-Ruiz, D.J. Braden, J.A. Dumesic, Catalytic Coupling of Carboxylic Acids by Ketonization as a Processing Step in Biomass Conversion, J. Catal., 266 (2009) 71-78.

[64] S.D. Randery, J.S. Warren, K.M. Dooley, Cerium Oxide-Based Catalysts for Production of Ketones by Acid Condensation, Appl. Catal., A, 226 (2002) 265-280.

[65] K.M. Dooley, A.K. Bhat, C.P. Plaisance, A.D. Roy, Ketones from Acid Condensation Using Supported CeO_2 Catalysts: Effect of Additives, Appl. Catal., A, 320 (2007) 122-133.

[66] O. Neunhoeffer, P. Paschke, About the mechanism of ketone formation from carboxylic acids, Chem. Ber., 72 (1939) 919-929.

[67] T.N. Pham, D. Shi, T. Sooknoi, D.E. Resasco, Aqueous-Phase Ketonization of Acetic Acid Over Ru/TiO_2/Carbon Catalysts, J. Catal., 295 (2012) 169-178.

[68] T.N. Pham, T. Sooknoi, S.P. Crossley, D.E. Resasco, Ketonization of Carboxylic Acids: Mechanisms, Catalysts, and Implications for Biomass Conversion, ACS Catal., 3 (2013) 2456-2473.

[69] M. Boudart, Turnover Rates in Heterogeneous Catalysis, Chem. Rev., 95 (1995) 661-666.

[70] S.D. Senanayake, D.R. Mullins, Redox Pathways for HCOOH Decomposition over CeO_2 Surfaces, J. Phys. Chem. C, 112 (2008) 9744-9752.

[71] W.O. Gordon, Y. Xu, D.R. Mullins, S.H. Overbury, Temperature Evolution of Structure and Bonding of Formic Acid and Formate on Fully Oxidized and Highly Reduced CeO_2(111), Phys. Chem. Chem. Phys., 11 (2009) 11171-11183.

[72] D.R. Mullins, S.D. Senanayake, T.L. Chen, Adsorption and Reaction of C_1-C_3 Alcohols Over CeO_x(111) Thin Films, J. Phys. Chem. C, 114 (2010) 17112-17119.

[73] T.L. Chen, D.R. Mullins, Adsorption and Reaction of Acetaldehyde Over CeO_x(111) Thin Films, J. Phys. Chem. C, 115 (2011) 3385-3392.

[74] D.R. Mullins, P.M. Albrecht, T.L. Chen, F.C. Calaza, M.D. Biegalski, H.M. Christen, S.H. Overbury, Water Dissociation on CeO_2(100) and CeO_2(111) Thin Films, J. Phys. Chem. C, 116 (2012) 19419-19428.

[75] F.C. Calaza, Y. Xu, D.R. Mullins, S.H. Overbury, Oxygen Vacancy-Assisted Coupling and Enolization of Acetaldehyde on CeO_2(111), J. Am. Chem. Soc., 134 (2012) 18034-18045.

[76] F.C. Calaza, T.L. Chen, D.R. Mullins, Y. Xu, S.H. Overbury, Reactivity and Reaction Intermediates for Acetic Acid Adsorbed on CeO_2(111), Catal. Today, 253 (2015) 65-76.

[77] C. Zhao, Y. Xu, Simulated Temperature Programmed Desorption of Acetaldehyde on CeO_2(111): Evidence for the Role of Oxygen Vacancy and Hydrogen Transfer, Top. Catal., 60 (2017) 446-458.

[78] A.K.P. Mann, Z. Wu, F.C. Calaza, S.H. Overbury, Adsorption and Reaction of Acetaldehyde on Shape-Controlled CeO_2 Nanocrystals: Elucidation of Structure–Function Relationships, ACS Catal., 4 (2014) 2437-2448.

[79] D. Cordell, J.O. Drangert, S. White, The Story of Phosphorus: Global Food Security and Food for Thought, Global Environ. Chang., 19 (2009) 292-305.

[80] L. Reijnders, Phosphorus Resources, Their Depletion and Conservation, a Review, Resour. Conserv. Recy., 93 (2014) 32-49.

[81] S.R. Carpenter, Phosphorus Control Is Critical to Mitigating Eutrophication, Proc. Natl. Acad. Sci. U. S. A., 105 (2008) 11039-11040.

[82] S.A. Parsons, J.A. Smith, Phosphorus Removal and Recovery from Municipal Wastewaters, Elements, 4 (2008) 109-112.

[83] B.K. Mayer, L.A. Baker, T.H. Boyer, P. Drechsel, M. Gifford, M.A. Hanjra, P. Parameswaran, J. Stoltzfus, P. Westerhoff, B.E. Rittmann, Total Value of Phosphorus Recovery, Environ. Sci. Technol., 50 (2016) 6606-6620.

[84] V.H. Freed, C.T. Chiou, D.W. Schmedding, Degradation of Selected Organophosphate Pesticides in Water and Soil, J. Agr. Food Chem., 27 (1979) 706-708.

[85] C. Lad, N.H. Williams, R. Wolfenden, The Rate of Hydrolysis of Phosphomonoester Dianions and the Exceptional Catalytic Proficiencies of Protein and Inositol Phosphatases, Proc. Natl. Acad. Sci. U. S. A., 100 (2003) 5607-5610.

[86] B.K. Singh, A. Walker, Microbial Degradation of Organophosphorus Compounds, Fems. Microbiol. Rev., 30 (2006) 428-471.

[87] F. Tan, Y. Zhang, J. Wang, J. Wei, Y. Cai, X. Qian, An Efficient Method for Dephosphorylation of Phosphopeptides by Cerium Oxide, J. Mass Spectrom., 43 (2008) 628-632.

[88] M.H. Kuchma, C.B. Komanski, J. Colon, A. Teblum, A.E. Masunov, B. Alvarado, S. Babu, S. Seal, J. Summy, C.H. Baker, Phosphate Ester Hydrolysis of Biologically Relevant Molecules by Cerium Oxide Nanoparticles, Nanomed-Nanotechnol., 6 (2010) 738-744.

[89] P. Janos, P. Kuran, M. Kormunda, V. Stengl, T.M. Grygar, M. Dosek, M. Stastny, J. Ederer, V. Pilarova, L. Vrtoch, Cerium Dioxide as a New Reactive Sorbent for Fast Degradation of Parathion Methyl and Some Other Organophosphates, J. Rare Earth, 32 (2014) 360-370.

[90] P. Janos, P. Kuran, V. Pilarova, J. Trogl, M. Stastny, O. Pelant, J. Henych, S. Bakardjieva, O. Zivotsky, M. Kormunda, K. Mazanec, M. Skoumal, Magnetically Separable Reactive Sorbent Based on the $CeO_2/\gamma\text{-}Fe_2O_3$ Composite and Its Utilization for Rapid Degradation of the Organophosphate Pesticide parathion Methyl and Certain Nerve Agents, Chem. Eng. J., 262 (2015) 747-755.

[91] M.J. Manto, P.F. Xie, C. Wang, Catalytic Dephosphorylation Using Ceria Nanocrystals, ACS Catal., 7 (2017) 1931-1938.

[92] J.K. Lassila, J.G. Zalatan, D. Herschlag, Biological Phosphoryl-Transfer Reactions: Understanding Mechanism and Catalysis, Annul. Rev. Biochem., 80 (2011) 669-702.

[93] J. Florian, A. Warshel, A Fundamental Assumption About OH^- Attack in Phosphate Ester Hydrolysis Is Not Fully Justified, J. Am. Chem. Soc., 119 (1997) 5473-5474.

[94] J. Florian, A. Warshel, Phosphate Ester Hydrolysis in Aqueous Solution: Associative versus Dissociative Mechanisms, J. Phys. Chem. B, 102 (1998) 719-734.

[95] M. Klähn, E. Rosta, A. Warshel, On the Mechanism of Hydrolysis of Phosphate Monoesters Dianions in Solutions and Proteins, J. Am. Chem. Soc., 128 (2006) 15310-15323.

[96] S.C.L. Kamerlin, N.H. Williams, A. Warshel, Dineopentyl Phosphate Hydrolysis: Evidence for Stepwise Water Attack, J. Org. Chem., 73 (2008) 6960-6969.

[97] B.R. Prasad, N.V. Plotnikov, A. Warshel, Addressing Open Questions About Phosphate Hydrolysis Pathways by Careful Free Energy Mapping, J. Phys. Chem. B, 117 (2013) 153-163.

[98] S.C.L. Kamerlin, P.K. Sharma, R.B. Prasad, A. Warshel, Why Nature Really Chose Phosphate, Q. Rev. Biophys., 46 (2013) 1-132.

[99] F. Duarte, A. Barrozo, J. Aqvist, N.H. Williams, S.C.L. Kamerlin, The Competing Mechanisms of Phosphate Monoester Dianion Hydrolysis, J. Am. Chem. Soc., 138 (2016) 10664-10673.

[100] C.N. Rusu, J.T. Yates, Adsorption and Decomposition of Dimethyl Methylphosphonate on TiO_2, J. Phys. Chem. B, 104 (2000) 12292-12298.

[101] D.A. Chen, J.S. Ratliff, X. Hu, W.O. Gordon, S.D. Senanayake, D.R. Mullins, Dimethyl Methylphosphonate Decomposition on Fully Oxidized and Partially Reduced Ceria Thin Films, Surf. Sci., 604 (2010) 574-587.

[102] G. Wang, C. Sharp, A.M. Plonka, Q. Wang, A.I. Frenkel, W. Guo, C. Hill, C. Smith, J. Kollar, D. Troya, J.R. Morris, Mechanism and Kinetics for Reaction of the Chemical Warfare

Agent Simulant, DMMP(g), with Zirconium(IV) MOFs: An Ultrahigh-Vacuum and DFT Study, J. Phys. Chem. C, 121 (2017) 11261-11272.

[103] Q. Wang, R.C. Chapleski, A.M. Plonka, W.O. Gordon, W. Guo, T.-D. Nguyen-Phan, C.H. Sharp, N.S. Marinkovic, S.D. Senanayake, J.R. Morris, C.L. Hill, D. Troya, A.I. Frenkel, Atomic-Level Structural Dynamics of Polyoxoniobates During DMMP Decomposition, Sci. Rep. -U. K., 7 (2017) 773.

[104] L. Trotochaud, R. Tsyshevsky, S. Holdren, K. Fears, A.R. Head, Y. Yu, O. Karslıoğlu, S. Pletincx, B. Eichhorn, J. Owrutsky, J. Long, M. Zachariah, M.M. Kuklja, H. Bluhm, Spectroscopic and Computational Investigation of Room-Temperature Decomposition of a Chemical Warfare Agent Simulant on Polycrystalline Cupric Oxide, Chem. Mater., 29 (2017) 7483-7496.

[105] C.A. Bunton, D.R. Llewellyn, K.G. Oldham, C.A. Vernon, The Reactions of Organic Phosphates: 1. The Hydrolysis of Methyl Dihydrogen Phosphate, J. Chem. Soc., 0 (1958) 3574-3587.

[106] K.D. Kwon, J.D. Kubicki, Molecular Orbital Theory Study on Surface Complex Structures of Phosphates to Iron Hydroxides: Calculation of Vibrational Frequencies and Adsorption Energies, Langmuir, 20 (2004) 9249-9254.

[107] G. Kresse, J. Furthmuller, Efficient Iterative Schemes for Ab Initio Total-Energy Calculations Using a Plane-Wave Basis Set, Phys. Rev. B, 54 (1996) 11169-11186.

[108] J.P. Perdew, J. Chevary, S. Vosko, K.A. Jackson, M.R. Pederson, D. Singh, C. Fiolhais, Atoms, Molecules, Solids, and Surfaces: Applications of the Generalized Gradient Approximation for Exchange and Correlation, Phys. Rev. B, 46 (1992) 6671.

[109] J. Klimeš, D.R. Bowler, A. Michaelides, Chemical Accuracy for the van der Waals Density Functional, J. Phys. -Condens. Mat., 22 (2010) 022201.

[110] J. Klimeš, D.R. Bowler, A. Michaelides, Van der Waals Density Functionals Applied to Solids, Phys. Rev. B, 83 (2011) 195131.

[111] G. Kresse, D. Joubert, From Ultrasoft Pseudopotentials to the Projector Augmented-Wave Method, Phys. Rev. B, 59 (1999) 1758-1775.

[112] G. Henkelman, B.P. Uberuaga, H. Jónsson, A Climbing Image Nudged Elastic Band Method for Finding Saddle Points and Minimum Energy Paths, J. Chem. Phys., 113 (2000) 9901-9904.

[113] S. Smidstrup, A. Pedersen, K. Stokbro, H. Jonsson, Improved Initial Guess for Minimum Energy Path Calculations, J. Chem. Phys., 140 (2014).

[114] G. Henkelman, H. Jónsson, A Dimer Method for Finding Saddle Points on High Dimensional Potential Surfaces Using Only First Derivatives, J. Chem. Phys., 111 (1999) 7010-7022.

[115] A. Heyden, A.T. Bell, F.J. Keil, Efficient Methods for Finding Transition States in Chemical Reactions: Comparison of Improved Dimer Method and Partitioned Rational Function Optimization Method, J. Chem. Phys., 123 (2005) 224101.

[116] S.L. Dudarev, G.A. Botton, S.Y. Savrasov, C.J. Humphreys, A.P. Sutton, Electron-Energy-Loss Spectra and the Structural Stability of Nickel Oxide: An LSDA+U Study, Phys. Rev. B, 57 (1998) 1505-1509.

[117] G. Kresse, P. Blaha, J.L.F. Da Silva, M.V. Ganduglia-Pirovano, Comment on “Taming Multiple Valency with Density Functionals: A Case Study of Defective Ceria”, Phys. Rev. B, 72 (2005) 237101.

[118] P. Redhead, Thermal Desorption of Gases, Vacuum, 12 (1962) 203-211.

[119] C. Loschen, J. Carrasco, K.M. Neyman, F. Illas, First-Principles LDA+U and GGA+U Study of Cerium Oxides: Dependence on the Effective U Parameter, Phys. Rev. B, 75 (2007) 035115.

[120] S. Lutfalla, V. Shapovalov, A.T. Bell, Calibration of the DFT/GGA+U Method for Determination of Reduction Energies for Transition and Rare Earth Metal Oxides of Ti, V, Mo, and Ce, J. Chem. Theory Comput., 7 (2011) 2218-2223.

[121] S. Fabris, G. Vicario, G. Balducci, S. de Gironcoli, S. Baroni, Electronic and Atomistic Structures of Clean and Reduced Ceria Surfaces, J. Phys. Chem. B, 109 (2005) 22860-22867.

[122] D.Y. Lu, P. Liu, Rationalization of the Hubbard U Parameter in CeO_x from First Principles: Unveiling the Role of Local Structure in Screening, J. Chem. Phys., 140 (2014) 084101.

[123] J. Neugebauer, M. Scheffler, Adsorbate-Substrate and Adsorbate-Adsorbate Interactions of Na and K Adlayers on Al (111), Phys. Rev. B, 46 (1992) 16067.

[124] J. Conesa, Computer Modeling of Surfaces and Defects on Cerium Dioxide, Surf. Sci., 339 (1995) 337-352.

[125] N.V. Skorodumova, M. Baudin, K. Hermansson, Surface Properties of CeO_2 from First Principles, Phys. Rev. B, 69 (2004) 075401.

[126] M. Nolan, S. Grigoleit, D.C. Sayle, S.C. Parker, G.W. Watson, Density Functional Theory Studies of the Structure and Electronic Structure of Pure and Defective Low Index Surfaces of Ceria, Surf. Sci., 576 (2005) 217-229.

[127] A.D. Mayernick, M.J. Janik, Methane Activation and Oxygen Vacancy Formation over CeO_2 and Zr, Pd Substituted CeO_2 Surfaces, J. Phys. Chem. C, 112 (2008) 14955-14964.

[128] T. Kropp, J. Paier, J. Sauer, Interactions of Water with the (111) and (100) Surfaces of Ceria, J. Phys. Chem. C, 121 (2017) 21571-21578.

[129] F. Esch, S. Fabris, L. Zhou, T. Montini, C. Africh, P. Fornasiero, G. Comelli, R. Rosei, Electron Localization Determines Defect Formation on Ceria Substrates, Science, 309 (2005) 752-755.

[130] J. Kullgren, M.J. Wolf, C.W.M. Castleton, P. Mitev, W.J. Briels, K. Hermansson, Oxygen Vacancies versus Fluorine at CeO_2(111): A Case of Mistaken Identity?, Phys. Rev. Lett., 112 (2014) 156102.

[131] H.J. Monkhorst, J.D. Pack, Special Points for Brillouin-Zone Integrations, Phys. Rev. B, 13 (1976) 5188-5192.

[132] J. Heyd, G.E. Scuseria, M. Ernzerhof, Erratum: "Hybrid Functionals Based on a Screened Coulomb Potential" [J. Chem. Phys. 118, 8207 (2003)], J. Chem. Phys., 124 (2006) 219906.

[133] L. Gerward, J. Staun Olsen, L. Petit, G. Vaitheeswaran, V. Kanchana, A. Svane, Bulk Modulus of CeO_2 and PrO_2—An Experimental and Theoretical Study, J. Alloys Compd., 400 (2005) 56-61.

[134] P.J. Hay, R.L. Martin, J. Uddin, G.E. Scuseria, Theoretical Study of CeO_2 and Ce_2O_3 Using a Screened Hybrid Density Functional, J. Chem. Phys., 125 (2006) 034712.

[135] E. Wuilloud, B. Delley, W.D. Schneider, Y. Baer, Spectroscopic Evidence for Localized and Extended f-Symmetry States in CeO_2, Phys. Rev. Lett., 53 (1984) 202-205.

[136] G.-y. Adachi, N. Imanaka, The Binary Rare Earth Oxides, Chem. Rev., 98 (1998) 1479-1514.

[137] A.V. Prokofiev, A.I. Shelykh, B.T. Melekh, Periodicity in the Band Gap Variation of Ln_2X_3 (X = O, S, Se) in the Lanthanide Series, J. Alloys Compd., 242 (1996) 41-44.

[138] L. Köhler, G. Kresse, Density Functional Study of CO on Rh(111), Phys. Rev. B, 70 (2004) 165405.

[139] J.I. Steinfeld, J.S. Francisco, W.L. Hase, Chemical Kinetics and Dynamics, Prentice Hall1999.

[140] M.P. Andersson, E. Abild-Pedersen, I.N. Remediakis, T. Bligaard, G. Jones, J. Engbæk, O. Lytken, S. Horch, J.H. Nielsen, J. Sehested, J.R. Rostrup-Nielsen, J.K. Nørskov, I. Chorkendorff, Structure Sensitivity of the Methanation Reaction: H_2-Induced CO Dissociation on Nickel Surfaces, J. Catal., 255 (2008) 6-19.

[141] H. Olcay, Y. Xu, G.W. Huber, Effects of Hydrogen and Water on the Activity and Selectivity of Acetic Acid Hydrogenation on Ruthenium, Green Chem., 16 (2014) 911-924.

[142] Z. Wu, M. Li, J. Howe, H.M. Meyer, S.H. Overbury, Probing Defect Sites on CeO_2 Nanocrystals with Well-Defined Surface Planes by Raman Spectroscopy and O_2 Adsorption, Langmuir, 26 (2010) 16595-16606.

[143] T. Mizukami, Physico-Chemical Studies on Acetaldehyde Polymerization at High Pressure and Low Temperature: 2. Kinetics of Polymerization of Acetaldehyde, Rev. Phys. Chem. Jpn., 35 (1965) 60.

[144] J.L. Davis, M.A. Barteau, Polymerization and Decarbonylation Reactions of Aldehydes on the Pd(111) Surface, J. Am. Chem. Soc., 111 (1989) 1782-1792.

[145] J. Carrasco, G. Vilé, D. Fernandez-Torre, R. Pérez, J. Pérez-Ramírez, M.V. Ganduglia-Pirovano, Molecular-Level Understanding of CeO_2 as a Catalyst for Partial Alkyne Hydrogenation, J. Phys. Chem. C, 118 (2014) 5352-5360.

[146] G. Vicario, G. Balducci, S. Fabris, S. de Gironcoli, S. Baroni, Interaction of Hydrogen with Cerium Oxide Surfaces: A Quantum Mechanical Computational Study, J. Phys. Chem. B, 110 (2006) 19380-19385.

[147] C. Popa, M.V. Ganduglia-Pirovano, J. Sauer, Periodic Density Functional Theory Study of VO_n Species Supported on the CeO_2(111) Surface, J. Phys. Chem. C, 115 (2011) 7399-7410.

[148] X.P. Wu, X.Q. Gong, G.Z. Lu, Role of Oxygen Vacancies in the Surface Evolution of H at CeO_2(111): A Charge Modification Effect, Phys. Chem. Chem. Phys., 17 (2015) 3544-3549.

[149] D.R. Mullins, P.M. Albrecht, F.C. Calaza, Variations in Reactivity on Different Crystallographic Orientations of Cerium Oxide, Top. Catal., 56 (2013) 1345-1362.

[150] M.A. Christiansen, G. Mpourmpakis, D.G. Vlachos, DFT-Driven Multi-Site Microkinetic Modeling of Ethanol Conversion to Ethylene and Diethyl Ether on γ-Al_2O_3(111), J. Catal., 323 (2015) 121-131.

[151] A. Beste, S.H. Overbury, Pathways for Ethanol Dehydrogenation and Dehydration Catalyzed by Ceria (111) and (100) Surfaces, J. Phys. Chem. C, 119 (2015) 2447-2455.

[152] B.H. Chen, Y.S. Ma, L.B. Ding, L.S. Xu, Z.F. Wu, Q. Yuan, W.X. Huang, Reactivity of Hydroxyls and Water on a CeO_2(111) Thin Film Surface: the Role of Oxygen Vacancy, J. Phys. Chem. C, 117 (2013) 5800-5810.

[153] D. Fernández-Torre, J. Carrasco, M.V. Ganduglia-Pirovano, R. Pérez, Hydrogen Activation, Diffusion, and Clustering on CeO_2(111): A DFT+U Study, J. Chem. Phys., 141 (2014) 014703.

[154] M. García-Melchor, N. López, Homolytic Products from Heterolytic Paths in H_2 Dissociation on Metal Oxides: the Example of CeO_2, J. Phys. Chem. C, 118 (2014) 10921-10926.

[155] M.J. Gilkey, B.J. Xu, Heterogeneous Catalytic Transfer Hydrogenation as an Effective Pathway in Biomass Upgrading, ACS Catal., 6 (2016) 1420-1436.

[156] C. Zhao, C. Watt, P.R. Kent, S.H. Overbury, D.R. Mullins, F.C. Calaza, A. Savara, Y. Xu, Coupling of Acetaldehyde to Crotonaldehyde on CeO_{2-x}(111): Bifunctional Mechanism and Role of Oxygen Vacancies, J. Phys. Chem. C, XXX (2018) XXX-XXX.

[157] S. Torbrügge, M. Reichling, A. Ishiyama, S. Morita, Ó. Custance, Evidence of Subsurface Oxygen Vacancy Ordering on Reduced CeO_2(111), Phys. Rev. Lett., 99 (2007) 056101.

[158] Z. Yang, T.K. Woo, M. Baudin, K. Hermansson, Atomic and Electronic Structure of Unreduced and Reduced CeO_2 Surfaces: A First-Principles Study, J. Chem. Phys., 120 (2004) 7741-7749.

[159] M. Fronzi, A. Soon, B. Delley, E. Traversa, C. Stampfl, Stability and Morphology of Cerium Oxide Surfaces in an Oxidizing Environment: A First-Principles Investigation, J. Chem. Phys., 131 (2009) 104701.

[160] M.V. Ganduglia-Pirovano, J.L.F. Da Silva, J. Sauer, Density-Functional Calculations of the Structure of Near-Surface Oxygen Vacancies and Electron Localization on CeO_2(111), Phys. Rev. Lett., 102 (2009) 026101.

[161] G.E. Murgida, M.V. Ganduglia-Pirovano, Evidence for Subsurface Ordering of Oxygen Vacancies on the Reduced CeO_2(111) Surface Using Density-Functional and Statistical Calculations, Phys. Rev. Lett., 110 (2013) 246101.

[162] J.E. Sutton, A. Beste, S.H. Overbury, Origins and Implications of the Ordering of Oxygen Vacancies and Localized Electrons on Partially Reduced CeO_2(111), Phys. Rev. B, 92 (2015) 144105.

[163] J.C. Conesa, Surface Anion Vacancies on Ceria: Quantum Modelling of Mutual Interactions and Oxygen Adsorption, Catal. Today, 143 (2009) 315-325.

[164] H.A. Hansen, C. Wolverton, Kinetics and Thermodynamics of H_2O Dissociation on Reduced CeO_2(111), J. Phys. Chem. C, 118 (2014) 27402-27414.

[165] H.Y. Li, H.F. Wang, Y.L. Guo, G.Z. Lu, P. Hu, Exchange between Sub-Surface and Surface Oxygen Vacancies on CeO_2(111): A New Surface Diffusion Mechanism, Chem. Commun., 47 (2011) 6105-6107.

[166] S. Wang, E. Iglesia, Experimental and Theoretical Evidence for the Reactivity of Bound Intermediates in Ketonization of Carboxylic Acids and Consequences of Acid–Base Properties of Oxide Catalysts, J. Phys. Chem. C, 121 (2017) 18030-18046.

[167] A.V. Ignatchenko, J.P. McSally, M.D. Bishop, J. Zweigle, Ab Initio Study of the Mechanism of Carboxylic Acids Cross-Ketonization on Monoclinic Zirconia via Condensation to beta-Keto Acids Followed by Decarboxylation, Mol. Catal., 441 (2017) 35-62.

[168] W. Tang, E. Sanville, G. Henkelman, A Grid-Based Bader Analysis Algorithm without Lattice Bias, J. Phys. -Condens. Mat., 21 (2009).

[169] D. Marrocchelli, B. Yildiz, First-Principles Assessment of H_2S and H_2O Reaction Mechanisms and the Subsequent Hydrogen Absorption on the CeO_2(111) Surface, J. Phys. Chem. C, 116 (2012) 2411-2424.

[170] D. Fernández-Torre, K. Kośmider, J. Carrasco, M.V. Ganduglia-Pirovano, R. Pérez, Insight into the Adsorption of Water on the Clean CeO_2(111) Surface with van der Waals and Hybrid Density Functionals, J. Phys. Chem. C, 116 (2012) 13584-13593.

[171] Y. Marcus, Ion Properties, Marcel Dekker, New York, 1997.

[172] M. Śmiechowski, Theoretical Calculation of pK_as of Phosphoric(V) Acid in the Polarisable Continuum and Cluster-Continuum Models, J. Mol. Struct., 924 (2009) 170-174.

[173] K. Mathew, R. Sundararaman, K. Letchworth-Weaver, T.A. Arias, R.G. Hennig, Implicit Solvation Model for Density-Functional Study of Nanocrystal Surfaces and Reaction Pathways, J. Chem. Phys., 140 (2014) 8.

[174] B.N. Zope, D.D. Hibbitts, M. Neurock, R.J. Davis, Reactivity of the Gold/Water Interface during Selective Oxidation Catalysis, Science, 330 (2010) 74-78.

[175] X. Nie, M.R. Esopi, M.J. Janik, A. Asthagiri, Selectivity of CO_2 Reduction on Copper Electrodes: The Role of the Kinetics of Elementary Steps, Angew. Chem. Int. Edit., 52 (2013) 2459-2462.

[176] C. Zhao, Y. Xu, Theoretical Investigation of Dephosphorylation of Phosphate Monoesters on CeO_2(111), Catal. Today, 312 (2018) 141-148.

[177] A.J. Kirby, F. Nome, Fundamentals of Phosphate Transfer, Accounts Chem. Res., 48 (2015) 1806-1814.

[178] D.R. Mullins, S.H. Overbury, D.R. Huntley, Electron Spectroscopy of Single Crystal and Polycrystalline Cerium Oxide Surfaces, Surf. Sci., 409 (1998) 307-319.

[179] T. Duchoň, M. Aulická, E.F. Schwier, H. Iwasawa, C. Zhao, Y. Xu, K. Veltruská, K. Shimada, V. Matolín, Covalent versus Localized Nature of 4f Electrons in Ceria: Resonant Angle-Resolved Photoemission Spectroscopy and Density Functional Theory, Phys. Rev. B, 95 (2017) 165124.

APPENDIX. COPYRIGHT INFORMATION

Springer Nature:

Springer Nature Customer Service Centre GmbH (the Licensor) hereby grants you a non-exclusive, world-wide licence to reproduce the material and for the purpose and requirements specified in the attached copy of your order form, and for no other use, subject to the conditions below:

1. The Licensor warrants that it has, to the best of its knowledge, the rights to license reuse of this material. However, you should ensure that the material you are requesting is original to the Licensor and does not carry the copyright of another entity (as credited in the published version). If the credit line on any part of the material you have requested indicates that it was reprinted or adapted with permission from another source, then you should also seek permission from that source to reuse the material.

2. Where print only permission has been granted for a fee, separate permission must be obtained for any additional electronic re-use.

3. Permission granted free of charge for material in print is also usually granted for any electronic version of that work, provided that the material is incidental to your work as a whole and that the electronic version is essentially equivalent to, or substitutes for, the print version.

4. A licence for 'post on a website' is valid for 12 months from the licence date. This licence does not cover use of full text articles on websites.

5. Where 'reuse in a dissertation/thesis' has been selected the following terms apply: Print rights of the final author's accepted manuscript (for clarity, NOT the published version) for up to 100 copies, electronic rights for use only on a personal website or institutional repository as defined by the Sherpa guideline (www.sherpa.ac.uk/romeo/).

6. Permission granted for books and journals is granted for the lifetime of the first edition and does not apply to second and subsequent editions (except where the first edition permission was granted free of charge or for signatories to the STM Permissions Guidelines http://www.stm-assoc.org/copyright-legal-affairs/permissions/permissions-guidelines/), and does not apply for editions in other languages unless additional translation rights have been granted separately in the licence.

7. Rights for additional components such as custom editions and derivatives require additional permission and may be subject to an additional fee. Please apply to Journalpermissions@springernature.com/bookpermissions@springernature.com for these rights.

8. The Licensor's permission must be acknowledged next to the licensed material in print. In electronic form, this acknowledgement must be visible at the same time as the figures/tables/illustrations or abstract, and must be hyperlinked to the journal/book's homepage. Our required acknowledgement format is in the Appendix below.

9. Use of the material for incidental promotional use, minor editing privileges (this does not include cropping, adapting, omitting material or any other changes that affect the meaning, intention or moral rights of the author) and copies for the disabled are permitted under this licence.

10. Minor adaptations of single figures (changes of format, colour and style) do not require the Licensor's approval. However, the adaptation should be credited as shown in Appendix below.

American Chemical Society:

PERMISSION/LICENSE IS GRANTED FOR YOUR ORDER AT NO CHARGE

This type of permission/license, instead of the standard Terms & Conditions, is sent to you because no fee is being charged for your order. Please note the following:

- Permission is granted for your request in both print and electronic formats, and translations.
- If figures and/or tables were requested, they may be adapted or used in part.
- Please print this page for your records and send a copy of it to your publisher/graduate school.
- Appropriate credit for the requested material should be given as follows: "Reprinted (adapted) with permission from (COMPLETE REFERENCE CITATION). Copyright (YEAR) American Chemical Society." Insert appropriate information in place of the capitalized words.
- One-time permission is granted only for the use specified in your request. No additional uses are granted (such as derivative works or other editions). For any other uses, please submit a new request.

Elsevier:

Please note that, as the author of this Elsevier article, you retain the right to include it in a thesis or dissertation, provided it is not published commercially. Permission is not required, but please ensure that you reference the journal as the original source. For more information on this and on your other retained rights, please visit: https://www.elsevier.com/about/our-business/policies/copyright#Author-rights.

American Physical Society:

The American Physical Society (APS) is pleased to grant the Requestor of this license a non-exclusive, non-transferable permission, limited to Electronic format, provided all criteria outlined below are followed.

1. You must also obtain permission from at least one of the lead authors for each separate work, if you haven't done so already. The author's name and affiliation can be found on the first page of the published Article.
2. For electronic format permissions, Requestor agrees to provide a hyperlink from the reprinted APS material using the source material's DOI on the web page where the work appears. The hyperlink should use the standard DOI resolution URL, http://dx.doi.org/{DOI}. The hyperlink may be embedded in the copyright credit line.
3. For print format permissions, Requestor agrees to print the required copyright credit line on the first page where the material appears: "Reprinted (abstract/excerpt/figure) with permission from [(FULL REFERENCE CITAT ION) as follows:

Author's Names, APS Journal Title, Volume Number, Page Number and Year of Publication.]

Copyright (YEAR) by the American Physical Society."

4. Permission granted in this license is for a one-time use and does not include permission for any future editions, updates, databases, formats or other matters. Permission must be sought for any additional use.

5. Use of the material does not and must not imply any endorsement by APS.

6. APS does not imply, purport or intend to grant permission to reuse materials to which it does not hold copyright. It is the requestor 's sole responsibility to ensure the licensed material is original to APS and does not contain the copyright of another entity, and that the copyright notice of the figure, photograph, cover or table does not indicate it was reprinted by APS with permission from another source.

7. The permission granted herein is personal to the Requestor for the use specified and is not transferable or assignable without express written permission of APS. This license may not be amended except in writing by APS.

8. You may not alter, edit or modify the material in any manner.

9. You may translate the materials only when translation rights have been granted.

10. APS is not responsible for any errors or omissions due to translation.

11. You may not use the material for promotional, sales, advertising or marketing purposes.

12. The foregoing license shall not take effect unless and until APS or its agent, Aptara, receives payment in full in accordance with Aptara Billing and Payment Terms and Conditions, which are incorporated herein by reference.

13. Should the terms of this license be violated at any time, APS or Aptara may revoke the license with no refund to you and seek relief to the fullest extent of the laws of the USA. Official written notice will be made using the contact information provided with the permission request. Failure to receive such notice will not nullify revocation of the permission.

14. APS reserves all rights not specifically granted herein.

15. This document, including the Aptara Billing and Payment Terms and Conditions, shall be the entire agreement between the parties relating to the subject matter hereof.

VITA

Chuanlin Zhao, was born and raised in the City of Jiamusi, Province of Heilongjiang, at the northeastern region of China, though his family was originally from the City of Chengdu, Province of Sichuan, at the southwestern region of China. He received a Bachelor of Engineering from the Department of Chemical Engineering with a direction in Polymer Engineering at Tianjin University, China. Then he directly went to the United States of America for advanced intellectual training by means of participating in the Doctor of Philosophy program in the Cain Department of Chemical Engineering at Louisiana State University. Upon completion of his Ph.D. degree, he plans to continue to work in the field of catalysis research at the fundamental level.